

THESIS ON INFORMATICS AND SYSTEM ENGINEERING C107

Statistical Methods for Ultrasound Image Segmentation

LIN LI

TUT
PRESS

TALLINN UNIVERSITY OF TECHNOLOGY
Faculty of Information Technology
Centre for Biorobotics

This dissertation was accepted for the defence of the degree of Philosophy in Engineering on October 19, 2015.

Supervisor: Prof. Maarja Kruusmaa
Centre for biorobotics
Tallinn University of Technology
Tallinn, Estonia

Opponents: Prof. Joni-Kristjan Kämäräinen
Department of Signal Processing
Tampere University of Technology
Tampere, Finland

Prof. Ville Kyrki
Department of Electrical Engineering
Aalto University
Helsinki, Finland

Defence of the thesis: December 3, 2015, Tallinn

Declaration:

Hereby I declare that this doctoral thesis, my original investigation and achievement, submitted for the doctoral degree at Tallinn University of Technology has not been submitted for any academic degree.



Copyright: Lin Li, 2015
ISSN 1406-4731
ISBN 978-9949-23-867-5 (publication)
ISBN 978-9949-23-868-2 (PDF)

INFORMAATIKA JA SÜSTEEMITEHNIKA C107

Ultrahelipiltide segmenteerimine statistiliste meetoditega

LIN LI

Contents

List of Publications.....	7
Related work	7
Author's Contribution to the Publications.....	8
Introduction	9
1 Background	13
1.1 Ultrasound imaging system	13
1.2 Speckle phenomenon.....	14
1.3 Statistical models for ultrasound image	15
1.3.1 Generalized Gaussian distribution.....	16
1.3.2 Rayleigh distribution	16
1.3.3 Fisher-Tippett distribution.....	18
1.4 Segmentation algorithms overview	18
1.4.1 Level set	19
1.4.2 Edge based active contour models	21
1.4.3 Region based active contour models	23
1.5 Summary	25
2 Region based statistical segmentation.....	26
2.1 Inhomogeneous image segmentation problem	26
2.2 Bhattacharyya distance	27
2.3 Novel contribution: combining CV and Bhattacharyya distance	28
2.4 Implementation.....	30
2.4.1 Narrow band and reinitialization approach	30
2.4.2 Numerical implementation details.....	31
2.5 Results	33
2.6 Conclusions	37
3 Localized active contour segmentation	38
3.1 Localized region based active contour algorithm.....	38
3.2 Novel contribution: Localized active contour with Rayleigh distribution	39

3.2.1	Maximum a posteriori estimation.....	40
3.2.2	Localized Rayleigh active contour	42
3.2.3	Localized shifted Rayleigh active contour	42
3.3	Implementation.....	44
3.4	Results	45
3.5	Conclusions	49
4	Localized region scalable fitting and the Bhattacharyya distance.....	50
4.1	Region scalable fitting algorithm	50
4.2	Novel contribution: Localized RSF algorithm	52
4.3	Implementation.....	55
4.4	Results	56
4.5	Conclusions	60
5	Conclusions	61
	References	63
	Abstract	80
	Kokkuvõte	81
	Appendix A	83
	Appendix B	105
	Appendix C	113
	Appendix D	119
	CURRICULUM VITAE	127
	ELULOOKIRJELDUS.....	128

List of Publications

This thesis is based on work reported in the following publications:

- A Muradore, R., Fiorini, P., Akgun, G., Barkana, D. E., Bonfe, M., Bonfe, F., Caprara, A., De Rossi, G., Dodi, R., Elle, O. J., Ferraguti, F., Gasperotti, L., Gassert, R., Mathiassen, K.; Handini, D., Lambercy, O., Li, L., Kruusmaa, M., Oberman Manurung, A., Meruzzi, G., Nguyen, H. Q. P., Preda, N., Riolfo, G., Ristolainen, A., Sanna, A., Secchi, C., Torsello, M., Yantac, A. E., "Development of a Cognitive Robotic System for Simple Surgical Tasks", *International Journal of Advanced Robotic Systems*, 2015, 12(37), pp.1-20.
- B Lin Li, Peeter Ross, Maarja Kruusmaa, "Ultrasound Image Segmentation by Bhattacharyya Distance with Rayleigh Distribution", in *Proc. IEEE Int. Conf. on Signal Processing: Algorithms, Architectures, Arrangements, and Applications (SPA)*, 2013, pp.149-153.
- C Lin Li, Maarja Kruusmaa, "Ultrasound Image Segmentation with Localized Level Set Based Curve Evolution and Rayleigh Distribution", in *Proc. IEEE Int. Conf. on Systems, Signals and Image Processing (IWSSIP)*, 2013, pp. 139-142.
- D Lin Li, Peeter Ross, Maarja Kruusmaa, Xiaosong Zheng, "A Comparative Study of Ultrasound Image Segmentation Algorithms for Segmenting Kidney Tumors", In *Proceedings of the 4th International Symposium on Applied Sciences in Biomedical and Communication Technologies*, ACM, 2011.

Related work

A paper related to the thesis that is not included in the appendices:

1. Maris, B., Dall'Alba, D., Fiorini, P., Ristolainen, A., Lin Li., Gavsins, Y., Barsi, A., Adhikarla, V.K (2013), "A phantom study for the validation of a surgical navigation system based on real-time segmentation and registration methods", *International Journal of Computer Assisted Radiology and Surgery (IJCARs)*, 8:1/S1, pp.381-382.

Author's Contribution to the Publications

Publication A: Developed the methodology, implemented the algorithm, and analyzed the segmentation results. Contributed to the writing of the "Ultrasound image segmentation" section.

Publication B: Proposed the initial idea, implemented the algorithm, evaluated the algorithm on ultrasound images and analyzed the results. Wrote the article.

Publication C: Proposed the initial idea, implemented the algorithm, evaluated the algorithm on ultrasound images and analyzed the results. Wrote the article.

Publication D: Proposed the initial idea, implemented the algorithm, evaluated the algorithm on ultrasound images and analyzed the results. Wrote the article.

Introduction

Ultrasound imaging technique was introduced to medical analyses in 1950s [1]. Since then it has been widely used in clinical application and is one of the most popular diagnostic method in medical diagnosis [2],[3]. The principle of ultrasound imaging is as follows [4]: an ultrasound transducer produces an acoustic wave and this acoustic wave propagates through the tissue and is partially reflected back because of the inhomogeneity of the tissue. The backscattered wave is received by the same transducer and further converted into a grayscale image which is then shown on a screen. Compared to other medical imaging techniques such as X-ray, computed tomography (CT) and magnetic resonance imaging (MRI), ultrasound imaging has several advantages. Firstly, an ultrasound machine has a short acquisition time [5]. The ultrasound machine is portable with relatively low cost [6]. And the ultrasound technique is non-invasive with no hazardous radiation emission [7].

Limitations of ultrasound imaging

However, ultrasound imaging has some limitations:

- Ultrasound image quality is poor compared to MRI and CT images. The tissue boundary in an ultrasound image is ambiguous and it is difficult to precisely detect the position of the organ on an ultrasound image due to the low contrast of the ultrasound image [8].
- The quality of an ultrasound image depends highly on the ultrasound machine, the acquisition conditions and the operator. The interpretation of the ultrasound image is subjective and it needs considerable training to obtain the expertise by the clinicians [9].

The low quality of ultrasound images limits the applications of the ultrasound imaging. To improve the quality of ultrasound images, many scientists are working on this challenging task [10],[11]. Mainly there are two research directions: one research direction is to improve the acquisition modality of ultrasound by investigating new probes [5], more sophisticated components [12] or more advanced apodization schemes [13],[14]; the other direction is ultrasound signal and image processing i.e. improving the ultrasound image by signal or image processing methods [15].

Image segmentation for ultrasound image

Image segmentation plays an important role in medical image analysis [16]. It is an important process for higher level image comprehension and is helpful for radiologists. It has wide applications such as in surgical path planning [17], in early disease detection [18] and in 3D reconstruction [19]. Unfortunately, the

noisy properties of ultrasound images decrease the performance of traditional algorithms which are developed for natural scenes [20].

Many scientists are working on the improvement of segmentation algorithms for ultrasound images [21],[22]. One way is to treat the speckle noise in ultrasound images as a source of information which provides useful information about the internal structure of the organ tissue. This concept is exploited widely in many applications such as classification [23], segmentation [24], registration [25].

Challenges in ultrasound image segmentation

Kidneys are essential organs and are located at the back of the abdomen [26]. Kidneys are bean shaped organs and are about 4-5 inches in length. Every year, many people suffer from chronic renal diseases due to diabetes mellitus, glomerulonephritis [27], etc. In Europe, kidney cancer accounts for nearly 3% of all cancer cases [28]. Because the kidney function failure can be life threatening, the detection of kidney disorders and diseases in the early stage is very crucial [29]. Ultrasound technique is widely used to diagnose kidney diseases in hospitals [30],[31]. Ultrasound imaging is the standard technique to examine renal abnormal structures such as stones, tumors, cysts [32],[33], etc.

In clinical practise, the detection of kidney border is usually done manually by the radiologist which is time consuming and subjective [34], [35]. A great deal of expertise is needed to correctly recognize the organ tissue or the part that the radiologist is interested in. Image segmentation methods on the other hand offer potential advantages, and can help the radiologist speed up the process and save their time from the tedious work. The benefits of using image processing methods are [36]:

- The kidney segmentation can be used in the surgical operations like puncturing. It plays an important role in the computer-aided diagnosis systems for kidney intervention.
- The segmentation results of kidney from other tissue by image processing methods can further be used for other process steps such as reconstruction, registration.

But due to the low ultrasound image quality and the presence of noise and artifacts, the detection of abnormal renal structure is difficult [21],[37]. The in vivo segmentation of kidney ultrasound images is a challenging task because of the following reasons [38]:

- The kidney is a deformable organ. The patient posture during the scan, as well as the physical conditions of the patient such as stomach and intestine can affect the shape of the kidney.
- The inner area of the kidney is not homogeneous. Its internal structure contains vein, arteries, pelivs, etc.

- The border between the kidney and the nearby tissue is not very clear. In some cases, it is difficult even for a specialist to tell exactly where the border of the kidney is, because there might be an area with no boundary at all.

Figure 0.1 shows an abdomen CT image with kidneys and a kidney ultrasound image. Both images are obtained from East Tallinn Central Hospital, Estonia.

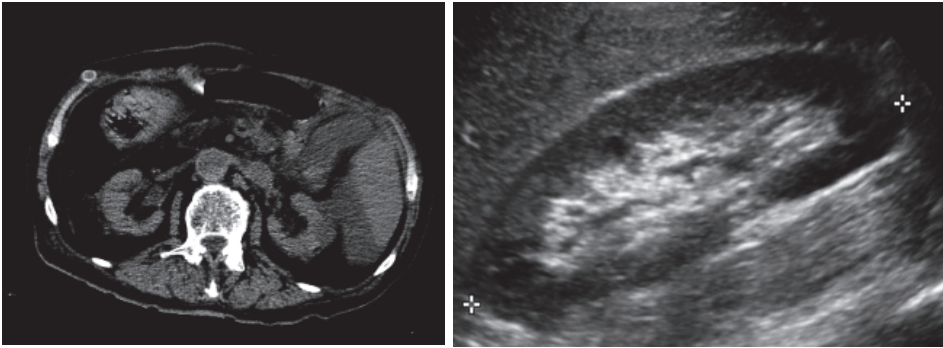


Figure 0.1 CT abdomen image and kidney ultrasound image

Contributions

This manuscript addresses the segmentation problem of kidney ultrasound image by using statistical methods. It focuses on the following methodological aspects:

- Statistical modeling of the ultrasound image signal to improve the detection of the kidney border.
- Segmentation methods are based on level sets. By using the level sets, the algorithms are able to deal with topological change.

The scientific contributions of this thesis are the following:

- Developing a region based active contour algorithm which combines the Chan & Vese algorithm and the Bhattacharyya distance for ultrasound image segmentation.
- Using the Rayleigh distribution for ultrasound image segmentation. A localized active contour framework is used for the kidney ultrasound image segmentation.
- Developing an algorithm which combines the localized active contour and the region scalable fitting algorithm together for ultrasound image segmentation.
- Showing that the proposed algorithms can improve the segmentation results for ultrasound image.

Organization of the thesis

The manuscript is divided into four main sections. The first section provides the background of ultrasound imaging system. The first section mainly focuses on the noisy property of ultrasound image and discusses the speckle phenomenon and various existing statistical models for ultrasound image. An overview of the segmentation algorithms for ultrasound image is also included in the first section.

In the second section, the speckle in the ultrasound image is exploited as a source of information and an algorithm which combines the Chan & Vese and the Bhattacharyya distance is proposed. The Rayleigh distribution is chosen as the ultrasound image intensity distribution. In the third section, a localized active contour framework is used and Rayleigh distribution and shifted Rayleigh distribution are chosen as the ultrasound image intensity distribution and a comparison between the performances of these two distributions is included. In the fourth section, an algorithm is proposed which can improve the segmentation result of region scalable fitting algorithm by introducing a localized factor into the region scalable fitting algorithm. Both synthetic and ultrasound images are used to test the performance of the proposed algorithms.

1 Background

Ultrasound imaging is commonly used in clinical application. Compared to other medical image modalities, ultrasound is safe, low cost and relatively cheap. Ultrasound imaging is the only non-invasive imaging modality which can acquire images in real time [39]–[41]. All of these features make the ultrasound imaging one of the most popular medical imaging techniques.

In this chapter, firstly the ultrasound imaging system is introduced. Then, the speckle noise in the ultrasound image is discussed. After that, various statistical distributions of an ultrasound image are presented and an overview about the segmentation algorithms for ultrasound images is given.

1.1 Ultrasound imaging system

Figure 1.1 shows a typical ultrasound system. An ultrasound system usually consists of a transducer, an ultrasound machine and an image display screen. The display image shown on the screen is obtained through a series of transformations from the original signal. The transducer generates an acoustic wave which then penetrates into the tissue and reflects back when tissue inhomogeneity occurs [42]. The backscattered signal is received by the transducer and then passes through different processes to get the final display image. Usually an ultrasound imaging system contains the following signals to analyze:

a) Radio-frequency (RF) signal

The reflected acoustical echo wave is received by the transducer and converted to a radio-frequency signal [43]. The RF signal provides the micro information about the internal structures.



Figure 1.1 Ultrasound system [44]

b) Analytic signal

Since the RF signal is a real signal, its Fourier transform is symmetric and therefore contains redundant information. The negative frequency component in the Fourier transform of the RF signal is removable and the resulting signal is the analytic signal without a loss of information. The analytic signal is a complex signal. The Fourier transform of the RF signal is usually achieved by using the Hilbert transform operator [45].

c) Complex In-phase/quadrature (IQ) signal

The in-phase/quadrature (IQ) signal is obtained by applying demodulation to the analytic signal [46]. The maximum frequency of the complex IQ signal is lower than the RF and analytic signal. The complex IQ signal preserves the same useful information as the RF signal but has a lower frequency than the RF signal.

d) Envelope detected signal

An envelope detection is performed on the IQ signal to obtain an envelope detected signal [47]. This envelope detected signal is further used for the display of the ultrasound image.

e) Display image

The envelope detected data is then log compressed to produce a grayscale display image for most commercial ultrasound systems. Often post-processing is employed to produce a grayscale image. Interpolation and rasterization is then carried out to produce the final display image. Several modes of display images are used clinically: B-mode M-mode, and Doppler mode [48].

1.2 Speckle phenomenon

The ultrasound transducer generates a high frequency acoustic wave. When the acoustic wave propagates in the tissue, the wave speed is changed by the tissue properties. The acoustic impedance of a biological tissue is not constant. Therefore, reflection occurs at the places where the acoustic property of the tissue is discontinuous. The reflected signal provides useful information about the tissue's internal structure. The echo reflection is received by the transducer and is further transformed to make a tissue image. There are two types of reflections: specular reflection and diffusive reflection [49].

- Specular reflection: when a sound wave reaches the region where the number of scatterers is large compared to the wavelength, specular reflection occurs. The specular reflection enables the visualization of the object's boundary.
- Diffuse reflection: Diffuse reflection appears when the acoustic wave transits in a region where the number of scatterers is smaller than the

wavelength of acoustical signal. Diffuse reflection causes the granular texture of the ultrasound image.

The diffuse reflection yields the speckle phenomenon. Speckle is the granular pattern in an ultrasound image. The speckle is the undesirable feature of the ultrasound image and is responsible for the noisy property of the ultrasound image [50]. The speckle depends on the resolution of the ultrasound machine. Since speckle is the backscattered wave from the scatterers inside the resolution cell, the nature of the scatterers, such as their density affects the speckle. If the number of scatterers inside the resolution cell is large and its density is uniform, then the speckle is called fully developed [51]. Otherwise, if the number of scatterers inside the resolution cell is small, the speckle is partially developed [52].

Though speckle pattern has random appearance, it is not a random process but a deterministic process [53]. If an object is scanned two times under the same situation, the speckle pattern will be exactly the same. For example, if we move the transducer back to the same position, it will create exactly the same image.

The speckle in the ultrasound image is correlated with the micro structure of the organ tissue. The speckle phenomenon causes difficulties in ultrasound image processing like ultrasound image segmentation, recognition and reconstruction. Speckle leads to intensity inhomogeneities inside the homogeneous tissue regions. In literature, the speckle can be viewed as noise or source of information [54],[55].

If the speckle is considered as noise, several despeckle methods [56] have been designed, for example Wiener filtering [57], anisotropic algorithm [58], wavelet algorithm [59], median filtering [60]. It is more common to view the speckle as a source of information which provides useful information about the tissue and can be exploited for certain applications. Statistical signal theory has been applied to analyze the ultrasound signal by modeling the ultrasound image formation as a statistical process [53]. The methods of modeling the speckle statistical probability distribution of ultrasound image are non-parametric [61], [62] and parametric [63],[64].

1.3 Statistical models for ultrasound image

In literature, statistical models for ultrasound image have been extensively studied [65]–[67]. Several distributions such as Rayleigh distribution [68],[69], Rician distribution [70],[71], K distribution [52],[72], generalized Gaussian distribution[73],[74] and Nakagami distribution [75],[76] are proposed to model the ultrasound image signal. In this section, some ultrasound image signal distributions are discussed: the generalized Gaussian distribution for RF signal, the Rayleigh distribution for envelope detected signal and Fisher-Tippett distribution for the display image.

1.3.1 Generalized Gaussian distribution

The RF signal is not commonly accessible for a commercial ultrasound machine. The generalized Gaussian distribution (GGD) is used for the RF signal [77]. The GGD is defined as:

$$P_{GGD} = \frac{\beta}{(2\alpha\Gamma(1/\beta))} \exp\left(-\left|\frac{y}{\alpha}\right|^\beta\right) \quad (1.1)$$

where α is the parameter for the scale control and β is for the shape control, σ is the standard deviation and $\Gamma(\cdot)$ is the Gamma function. Figure 1.2 shows the GGD with different β values. The estimation methods for the GGD parameters α and β are usually based on maximum likelihood methods [78] and moments matching methods [79].

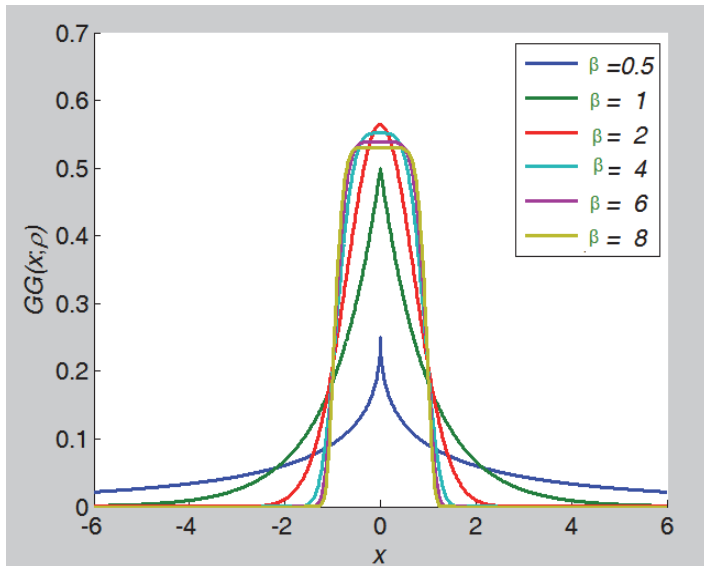


Figure 1.2 Generalized Gaussian distribution

1.3.2 Rayleigh distribution

The Rayleigh distribution is the most commonly used distribution for the ultrasound envelope-detected image. For fully developed speckle situation, i.e. in the resolution cell the number of scatterers are very large, the ultrasound envelope image follows the Rayleigh distribution [53]. When the number of scatterers per resolution cell is very high, the scatterers phase is uniformly

distributed, and using the central limit theorem, the joint probability density function is:

$$P = \frac{1}{2\pi\sigma^2} e^{-\frac{r^2+i^2}{2\sigma^2}} \quad (1.2)$$

Where r is the real and i is the imaginary parts of the corresponding signal. Transforming from Cartesian coordinate to Polar coordinate, the Rayleigh distribution is obtained by:

$$P_{Rayleigh} = \frac{\rho}{\sigma^2} e^{-\frac{\rho^2}{2\sigma^2}} \quad (1.3)$$

where $\rho = \sqrt{r^2 + i^2}$ is the magnitude of the signal. The phase of the signal is uniformly distributed $[-\pi, \pi]$. Figure 1.3 represents the Rayleigh distribution with different σ values.

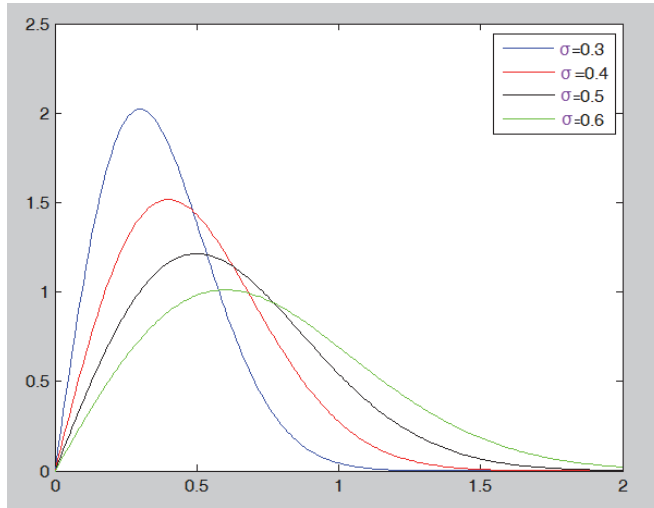


Figure 1.3 Rayleigh distribution

The analytic expression of Rayleigh distribution is simple which makes it attractive. The maximum likelihood method (MLE) is usually employed in the estimation of the parameter σ^2 . For n number of elements $(y_1, y_2 \dots y_n)$, the MLE estimation of the σ^2 is:

$$\hat{\sigma}^2 = \frac{1}{2n} \sum_{i=1}^n y_i^2 \quad (1.4)$$

1.3.3 Fisher-Tippett distribution

The ultrasound envelope-detected image has a large dynamic range. Therefore log compression approach is usually employed to produce an image with a suitable dynamic range to display on a monitor for most commercial ultrasound machines. In [80] the distribution of display image was investigated and it was pointed out that the display image distribution was a Fisher-Tippett distribution. The Fisher-Tippett distribution is defined as follows:

$$P = 2\exp\left(\frac{1}{2\sigma^2}\right)\exp\{2\rho - \ln(2\sigma^2) - e^{[2\rho - \ln(2\sigma^2)]}\} \quad (1.5)$$

where σ^2 is the parameter of Fisher-Tippett distribution.

1.4 Segmentation algorithms overview

Ultrasound imaging is commonly used in clinical diagnostics such as the detection of breast abnormality [81]–[83], prostate cancer [84]–[86], liver diseases [87]–[89], the 2D/3D visualization of fetus [90],[91], etc. The ultrasound imaging also plays an important role in the early detection of the kidney diseases [92]–[94]. The real time visualization of ultrasound images makes it possible to use it in surgical robotics, for example for the identification of the organs of interest [95],[96], or pathology of those organs [97],[98]. Compared to other medical imaging techniques, ultrasound imaging is cheaper, relatively safer and more adaptable. Therefore, ultrasound imaging has important applications in the clinical field.

Image segmentation is a fundamental step for image analysis and is the basis for higher level applications such as registration, visualization, clinical diagnosis [99]. However, compared to other medical images, such as computed tomography and magnetic resonance imaging, ultrasound images are difficult to segment because their quality is relatively poor. The speckle phenomenon in the ultrasound images leads to the granular texture in the images. Moreover, because of the attenuation of the ultrasonic wave in the tissue, the intensity of the tissue always changes and the boundaries of the tissue are often not prominent or sometime are completely missing.

Since the image segmentation plays an important role for ultrasound image analysis, different algorithms for segmenting the object boundaries in ultrasound images will be presented in this section. In literature, several methods have been proposed to semi-automatically [100] or automatically[101] detect the objects' borders in ultrasound images. Methods such as region growing[102]–[104], statistical methods[105]–[107], Markov random fields [108]–[110], and active contour models [111]–[113] are among the most frequently used. The active contour models will be mainly discussed here.

Active contour (AC) models are commonly used in ultrasound image segmentation for example for intravascular ultrasound images [114],[115], breast ultrasound images [116],[117], echocardiography [118],[119] and kidney ultrasound images [37],[120]. Active contour models can be classified as parametric active contour models [121] or geometric active contour models [122]. The parametric active contour models explicitly represent the curve. On the other hand, the geometric active contour models represent the curve as the zero level set of an implicit function and evolve the level set function in an Eulerian framework. The geometric active contours models have several advantages over the parametric active contour models. Firstly, the level set representation is independent of the curve parametrization and enables to topologically change of the curve. Secondly, the efficient numerical schemes of the level set function make the calculation flexible and easy.

Some level set based active contour methods are calculated by partial differential equations (PDE) [123]. Other active contour models, which are known as variational level set methods, directly derive the level set evolution function by minimizing a certain energy function [124],[125]. Additional information, like region information [126] and shape-prior information[127] can be easily incorporated into the variational level sets energy function.

According to the segmentation methodologies, the active contours can be mainly divided into edge based active contours[128]–[130] and region based active contours [131]–[133]. Edge based active contours use edge information for curve evolution. Region based active contours on the other hand utilize region information instead of image gradient. The edge based active contour models are sensitive to the noise and poor image contrast, which result in bad segmentation. The region based active contours use the region information such as intensity statistics in the energy function and are more robust than the edge based active contours. By integrating the prior shape knowledge of the objects into the active contours energy functions, the active contours are able to solve the occlusion problems or the missing edge problems. More information about the shape prior active contours can be found in [134]–[136].

1.4.1 Level set

The image segmentation problem can be represented as an optimization problem. By evolving the curve according to a certain energy function, the curve reaches the optimized position which is also the result of the segmentation. Level set method was first introduced in [137]. The level set based segmentation methods are efficient, flexible and are able to deal with topological change.

Let I be a given image. Let γ be a family of closed curves and let a curve $\Gamma: s, t \in [0,1] \times \mathcal{R}^+ \rightarrow \Gamma(s, t) = (x(s, t), y(s, t), t) \in \Omega \times \mathcal{R}^+$ so that $\forall t$ curve

$\Gamma_t: s \rightarrow (x(s, t), y(s, t))$ is in γ [138]. The curve Γ can be represented by the zero level-set of a Lipschitz-continuous function ϕ called level set function:

$$\begin{cases} \phi > 0 & \forall x, y \in \Omega_i \\ \phi < 0 & \forall x, y \in \Omega_o \\ \phi = 0 & \forall x, y \in \Gamma \end{cases} \quad (1.6)$$

where x, y is a point coordination in Ω . Ω_i represents the region inside Ω bounded by Γ and Ω_o represents the region $\Omega_o = \Omega \setminus \Omega_i$.

In the level set formulation, for every s and t , the curve can be represented by

$$\phi(\Gamma(s, t)) = \phi(x(s, t), y(s, t), t) = 0 \quad (1.7)$$

In general, the total derivative of (1.7) with respect to time t is

$$\frac{d\phi}{dt} = \frac{\partial\phi}{\partial x} \frac{\partial x}{\partial t} + \frac{\partial\phi}{\partial y} \frac{\partial y}{\partial t} + \frac{\partial\phi}{\partial t} = \langle \nabla\phi, \frac{\partial\Gamma}{\partial t} \rangle + \frac{\partial\phi}{\partial t} = 0 \quad (1.8)$$

Let $\frac{\partial\Gamma}{\partial t} = V\mathbf{n}$, where V is the velocity and \mathbf{n} is the normal outward direction, the following equation is obtained:

$$\frac{\partial\phi}{\partial t} = -V \langle \nabla\phi, \mathbf{n} \rangle \quad (1.9)$$

The evolution of equation (1.9) only involves the normal velocity. Only the normal velocity contributes to the curve evolution, the tangential velocity doesn't change the geometry of the curve [138].

The segmentation problem can be represented as the minimization of a specific energy criterion E of the level set curve evolution. The steady state of the curve divides the image into the region of targets and the region of background:

$$\hat{\phi} = \underset{\phi}{\operatorname{argmin}} \{E(\phi)\} \quad (1.10)$$

The first variation of E with respect to ϕ is:

$$\frac{\partial E}{\partial\phi} = \lim_{t \rightarrow 0} \frac{1}{t} \{E(\phi + t\varepsilon) - E(\phi)\} \quad (1.11)$$

Using the gradient descent method the following equation is obtained:

$$\frac{\partial\phi}{\partial t} = - \frac{\partial E}{\partial\phi} \quad (1.12)$$

Figure 1.4 shows an illustration of the level set method.

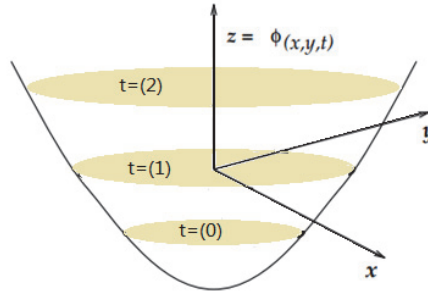


Figure 1.4 Level set method illustration

1.4.2 Edge based active contour models

Many edge based active contour algorithms have been proposed for different application purposes. Edge based active contour algorithms use edge information to detect the borders of the objects. Generally the edge based approaches do not assume homogeneous image intensities. The edge based active contours are usually sensitive to the initialization of the curve.

a) Kass-Witkin-Terzopoulos Snake model

The Kass-Witkin-Terzopoulos snake model was proposed in [139]. The snake model drives the curve evolving toward the high image gradient. The snake model is based on solving the following energy function:

$$E_{snake} = \int_0^1 \alpha |\gamma'|^2 dq + \int_0^1 \beta |\gamma''|^2 dq - \lambda \int_0^1 |I(\gamma(q))|^2 dq \quad (1.13)$$

where $\gamma(q) = (x(q), y(q)) \in \Omega (q \in [0,1])$ is a parametric planar curve. The first two terms of (1.13) correspond to the internal energy term which used to enforce the smoothness of the curve. The last term of (1.13) is the external energy term which determines the curve evolution and drives the curve towards the high image gradient.

The shortcomings of the snake model are several. It is sensitive to noise in the image. Also, it is unable to deal with the topology change during the curve evolution. Therefore, only the single connected object is segmented from the background.

b) Geodesic active contour model

The geodesic active contour model was introduced in [140]. The energy function of geodesic active contour model is:

$$E_{GAC} = \int_a^b g(|\nabla I(\gamma(q))|) |\gamma'(q)| dq \quad (1.14)$$

where $g(\cdot)$ is an edge indicator function. Commonly, the choice of g is:

$$g = \frac{1}{1 + t^2} \quad (1.15)$$

The minimization of the geodesic active contour energy function is obtained by solving the following equation:

$$\frac{\partial \gamma}{\partial t} = - \frac{\partial E}{\partial \gamma} \quad (1.16)$$

The minimization of the energy function is obtained by the following equation:

$$\frac{\partial \gamma}{\partial t} = -(g(|\nabla I(\gamma)|)k + \langle \nabla g |\nabla I(\gamma)|, \mathbf{n} \rangle) \mathbf{n} \quad (1.17)$$

where k is the the curvature of the curve.

The disadvantage of the geodesic active contour method is that it uses only the image information along the curve. So it is easy to get trapped in local minima or evolve toward the wrong direction. Also, it is difficult for the geodesic active contour to get correct results if the initial curve is too far away from the desired position. Figure 1.5 shows the segmentation results of geodesic active contour model on a noisy image.

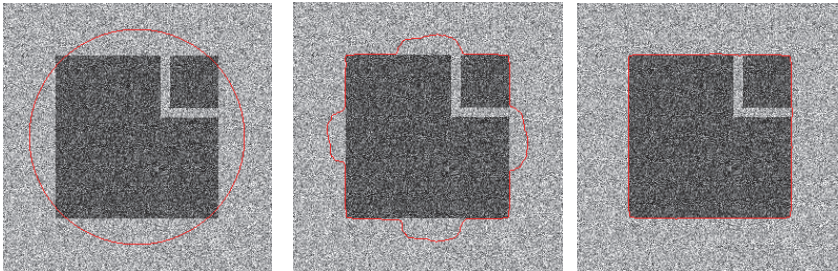


Figure 1.5 Segmentation results of geodesic active contour

1.4.3 Region based active contour models

The region based active contours are an alternative to edge based active contours. The region based active contours utilize region information instead of the image gradient. The most general region based active contour's energy function can be written as:

$$E = \alpha \int_{\Omega_i} f_i(\phi, x) dx + \beta \int_{\Omega_o} f_o(\phi, x) dx + \gamma \int_{\Omega_\Gamma} f_c(\phi, x) |\nabla \phi| dx \quad (1.18)$$

The first two terms are the region term and the last term is called the contour term which is associated with the curve Γ .

a) Mumford and Shah model

The Mumford and Shah (MS) [141] model is an important model in image segmentation. The MS model has been intensively studied and has influenced numerous methods. The image segmentation problem is treated as image smoothing and boundary detection in the MS model. The energy function of the MS model is:

$$E_{MS} = \int_{\Omega_i} (I - M)^2 dx + \rho \int_{\Omega_o} |\nabla M|^2 dx + \lambda \rho l(K) \quad (1.19)$$

where M is a smooth approximation and K is a set of discontinuous edges. The first term of the MS model is the data term which drives the curve evolving toward the desired place. The second term is the smoothness prior term. The last term is the length prior term which is used to regularize the boundaries.

b) Chan & Vese model

The Chan & Vese (CV) model was proposed in [142]. The CV model is a simplified model of MS model. In CV method, the image features are assumed to be similar within a segment. In this case, the image I is assumed to be consisting of two segments with approximately piecewise-constant intensities. Suppose a curve Γ divides the image domain into two parts: Ω_i and Ω_o , the energy function of CV model is:

$$E_{cv} = \lambda_1 \int_{\Omega_i} (I - u)^2 dx + \lambda_2 \int_{\Omega_o} (I - v)^2 dx + \lambda_3 \int_{\Omega_\Gamma} ds + \lambda_4 \int_{\Omega_i} dx \quad (1.20)$$

where u is the mean of the intensity inside the curve Γ and v is the mean intensity of the region outside Γ . The CV model assumes that foreground and

background regions can be separated by maximizing the mean intensities between them. The energy optimization will move the curve toward the largest difference between interior and exterior means.

For the level-set formulation, the Heaviside function $H(\phi)$ is usually used. The Heaviside function is expressed as:

$$H(\phi) = \begin{cases} 1, & \text{if } \phi \geq 0 \\ 0, & \text{if } \phi < 0 \end{cases} \quad (1.21)$$

and the Dirac function $\delta(\phi)$ is defined as:

$$\delta(\phi) = \frac{d}{d\phi} H(\phi) \quad (1.22)$$

the Heaviside function H and the Dirac function δ can be approximated as H_ε and δ_ε by the following equations:

$$\begin{aligned} H_\varepsilon(x) &= \frac{1}{2} \left[1 + \frac{2}{\pi} \arctan\left(\frac{x}{\varepsilon}\right) \right] \\ \delta_\varepsilon(x) &= H'_\varepsilon(x) = \frac{1}{\pi} \frac{\varepsilon}{\varepsilon^2 + x^2} \end{aligned} \quad (1.23)$$

Using Heaviside function $H(\phi)$ and the Dirac function $\delta(\phi)$, the CV model can be written as:

$$\begin{aligned} E_{cv} &= \lambda_1 \int_{\Omega} (I - u)^2 H(\phi) dx + \lambda_2 \int_{\Omega} (I - v)^2 (1 - H(\phi)) dx \\ &\quad + \lambda_3 \int_{\Omega} |\nabla \phi| \delta(\phi) dx \end{aligned} \quad (1.24)$$

The evolution of equation (1.24) is:

$$\frac{\partial \phi}{\partial t} = \delta(\phi) \left[\lambda_1 (I - u)^2 - \lambda_2 (I - v)^2 + \lambda_3 \nabla \left(\frac{\nabla \phi}{|\nabla \phi|} \right) \right] \quad (1.25)$$

Figure 1.6 illustrates the CV algorithm.

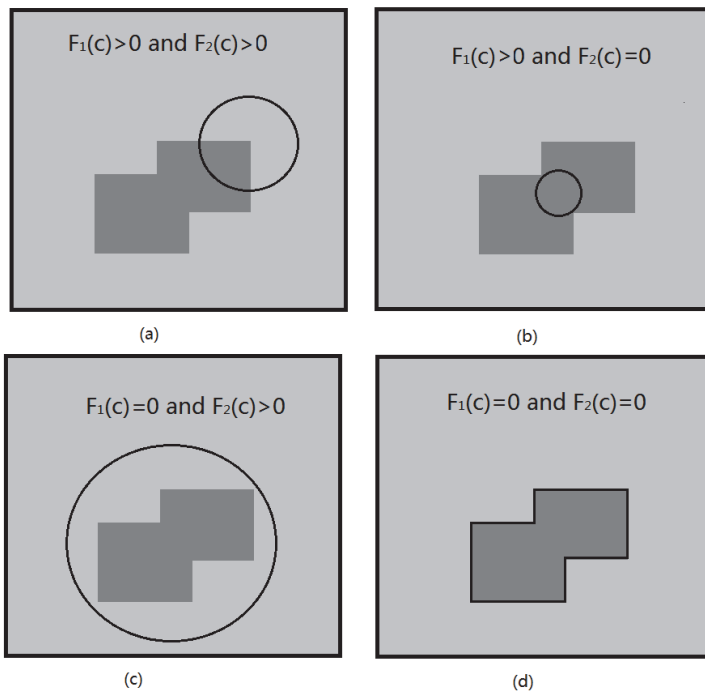


Figure 1.6 Illustration of CV algorithm

1.5 Summary

In this section, ultrasound imaging system is introduced. Then the speckle phenomenon is discussed, and speckle phenomenon is presented. Various kinds of ultrasound image distributions are introduced. Later, an overview about the image segmentation algorithms is given and various kinds of different existing active contour models are presented.

2 Region based statistical segmentation

An ultrasound image is obtained through a chain of transformations from the RF signal, the analytic signal, and the envelope detected signal to the final display image. B-mode images are the most popular type of ultrasound images in clinical applications [143],[144]. For ultrasound image segmentation, it is crucial to determine the image intensity by an adequate statistical distribution. In this section, an active contour algorithm which combines the Chan & Vese algorithm and Bhattacharyya distance together is proposed to solve the ultrasound image segmentation problem. The algorithm described in this chapter is related to publication B.

2.1 Inhomogeneous image segmentation problem

The artifacts in an ultrasound image make the tissue borders difficult to distinguish from the ultrasound image [145]. The intensity inhomogeneity in the ultrasound image leads to blurry boundaries, therefore the segmentation of an inhomogeneous image is a challenging task.

In section 1.4 the Chan & Vese (CV) segmentation algorithm is introduced which is an important region based active contour algorithm. The CV algorithm is a global algorithm, and it is robust to noise and works well on low contrast images. But the global minimization of the CV algorithm does not always guarantee satisfactory results. The convergence of CV algorithm depends on the segmented object's homogeneity. If the image is very noisy or contains large inhomogeneous regions, the CV method has trouble to correctly segment the objects. For example Figure 2.1 shows a segmentation result of CV algorithm in which the CV algorithm fails to produce correct result.

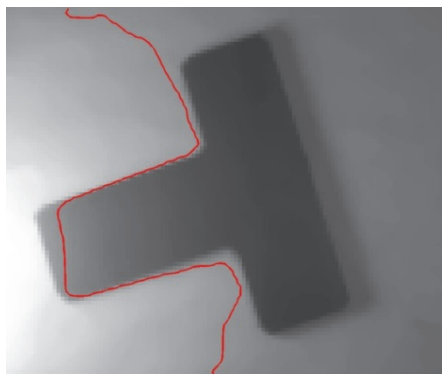


Figure 2.1 Segementaion result of CV algorithm

To improve the segmentation result, one approach is to incorporate the prior knowledge of the image with the algorithm. A short description about the Bhattacharyya distance is given in section 2.2 and a new algorithm is proposed which considering the statistics of the ultrasound image with the CV algorithm in section 2.3.

2.2 Bhattacharyya distance

The goal of image segmentation is to partition the image region into a number of sub-regions according to certain properties so that each sub-region is homogeneous. A more practical way to think of the segmentation problem is to decompose the image into distinct fragments. Therefore, statistical methods can be applied to model the image fragments.

For ultrasound image segmentation, under the assumption that the intensity distributions between different objects are different, an intuitive way is to define a criterion which minimizes the overlap between the image's objects and the background. The ideal measurement is that a measurement that can minimize the difference within each segment and maximize the difference between segments.

In literature, there are many measurement metrics which measure the difference between probability distribution functions such as Kullback–Leibler divergence [146], the Wasserstein distance [147] and Bhattacharyya distance [148]. The Bhattacharyya distance has several advantages such as that it has a simple analytical form and it can work with arbitrary distributions, while the Kullback–Leibler divergence requires mean separated distributions to yield good results and the Wasserstein distance based segmentation model assumes an independently identical distributed image intensity [149].

Also, the Bhattacharyya distance has recently been successfully applied in object tracking [150], and image segmentation [151]. In [151] an image segmentation algorithm based on the Bhattacharyya distance was introduced. Specifically, the algorithm maximized the difference between image regions with respect to the given metrics. By incorporating the Bhattacharyya distance, the mutual information between the separated regions is maximized.

The Bhattacharyya distance measures the similarity between two probability distribution functions $P_i(z)$ and $P_o(z)$ with $z \in R^N$. The Bhattacharyya distance is defined as $D = -\log B$ where B is the Bhattacharyya coefficient:

$$B = \int_{R^N} \sqrt{P_i(z)P_o(z)} dz \quad (2.1)$$

The range of Bhattacharyya coefficient is between [0, 1] Since the logarithm function is monotonically increasing, the minimization of B is equivalent to the maximization of D .

2.3 Novel contribution: combining CV and Bhattacharyya distance

Based on above discussions, an active contour algorithm is proposed here which uses the statistical model to segment the ultrasound image. The Rayleigh distribution is incorporated with the level set active contour algorithm. This choice is made because of the following reasons:

- Using active contours framework, it is very easy to embed a prior statistical knowledge of the image to be segmented.
- The level set approach allows the geometric change of the curve and therefore is able to deal with the topological change of the object.
- The Rayleigh distribution has been widely used in US image segmentation with satisfactory results.

The CV algorithm is a global algorithm. In CV algorithm, the curve divides the image domain into two parts: internal and external regions. The reason why CV algorithm fails in producing satisfactory segmentation result for an inhomogeneous object is that only the mean value is used, which is not sufficient. Therefore, to improve the segmentation result, the whole image intensity information should be considered instead of using only the mean value. Under the assumption that the intensity between one object and the background is different, a criterion is defined which can maximize the difference. As mentioned in section 2.2, the Bhattacharyya distance is an efficient metric and it can measure the closeness between the segments. The Bhattacharyya distance is used to measure the similarity between these segments and the difference of the measurement is then added as additional energy term with the CV energy function. By properly balancing two parts, the difference within each segment is minimized and the difference between separated segments is maximized. The new evolution function is implemented in a level set framework and it is able to deal with topological changes.

The whole energy function of the proposed algorithm incorporating the Bhattacharyya distance with the CV model is:

$$E(C) = \alpha F(C) + (1 - \alpha)B(C) + \beta Length(C) \quad (2.2)$$

where α and β are the weighting parameters and $\alpha \in [0,1]$. The energy function of the proposed algorithm consists of three parts: the region CV fitting term $F(C)$, the Bhattacharyya distance term $B(C)$, and the regularization component $Length(C)$. The outcome of this algorithm is the minimization of the difference within each segment and the maximization of the difference between the separated segments.

Using the level set method, the energy function of (2.2) can then be written as:

$$\begin{aligned}
E(\phi) &= \alpha F(\phi) + (1 - \alpha)B(\phi) + \beta \text{Length}(\phi) \\
&= \left\{ \alpha \int_{\Omega} (I - u)^2 H(\phi(x)) dx + (I - v)^2 (1 - H(\phi(x))) dx \right\} \\
&+ (1 - \alpha) \int_{R^N} \sqrt{P_i(z)P_o(z)} dz + \beta \int_{\Omega} |\nabla H(\phi(x))| dx \quad (2.3)
\end{aligned}$$

Rayleigh distribution is chosen to model the ultrasound image's statistical intensity distribution. According to [152] the Bhattacharyya coefficient with Rayleigh distribution is calculated as:

$$B(\phi(x)) = 2 \cdot \frac{\sigma_i(\phi(x)) \cdot \sigma_o(\phi(x))}{\sigma_i^2(\phi(x)) + \sigma_o^2(\phi(x))} \quad (2.4)$$

The parameter u and v are calculated by equation (2.5). The parameters σ_i^2 and σ_o^2 are calculated by Maximum-Likelihood (ML) method. The value of σ_i^2 and σ_o^2 is obtained by following equations:

$$\begin{aligned}
u &= \frac{\int_{\Omega} IH(\phi(x)) dx}{\int_{\Omega} H(\phi(x)) dx} & v &= \frac{\int_{\Omega} IH(1 - \phi(x)) dx}{\int_{\Omega} H(1 - \phi(x)) dx} \\
\sigma_o^2 &= \frac{\int_{\Omega} I^2 H(1 - \phi(x)) dx}{2 \int_{\Omega} H(1 - \phi(x)) dx} & \sigma_i^2 &= \frac{\int_{\Omega} I^2 H(\phi(x)) dx}{2 \int_{\Omega} H(\phi(x)) dx} \quad (2.5)
\end{aligned}$$

The first variation of (2.3) with respect to ϕ can be calculated as:

$$\frac{\partial E}{\partial \phi} = \alpha \frac{\partial F(\phi(x))}{\partial \phi(x)} + (1 - \alpha) \frac{\partial B(\phi(x))}{\partial \phi(x)} + \beta \delta(\phi(x)) \text{div} \left(\frac{\nabla \phi(x)}{|\nabla \phi(x)|} \right) \quad (2.6)$$

The level set equation of (2.6) is derived as:

$$\begin{aligned}
\frac{\partial \phi}{\partial t} &= - \frac{\partial E(\phi(x))}{\partial \phi(x)} \\
&= \alpha \delta(\phi) [(I - u)^2 - (I - v)^2] - (1 - \alpha) \frac{(\sigma_i \cdot \sigma_o) \cdot (\sigma_i^2 - \sigma_o^2)}{(\sigma_i^2 + \sigma_o^2)^2} \\
&\left\{ \frac{1}{A_i} \left[\frac{I^2(x)}{2\sigma_i^2} - 1 \right] + \frac{1}{A_o} \left[\frac{I^2(x)}{2\sigma_o^2} - 1 \right] \right\} \delta(\phi(x)) + \beta \delta(\phi(x)) \text{div} \left(\frac{\nabla \phi(x)}{|\nabla \phi(x)|} \right) \quad (2.7)
\end{aligned}$$

where A_i is the interior region and A_o is the exterior region:

$$A_i = \int_{\Omega} H(\phi(x)) dx \quad A_o = \int_{\Omega} (1 - H(\phi(x))) dx \quad (2.8)$$

2.4 Implementation

In this section, the algorithm implementation details will be discussed. The narrow band and reinitialization approach will be discussed, following by the numerical implementation details of the algorithm.

2.4.1 Narrow band and reinitialization approach

A narrow band method [153] is used in the implementation of the algorithm. The narrow band method is an efficient method in the evolution of level set. Instead of calculating the whole image domain which is computationally expensive, the narrow band method performs the calculation only in a neighborhood of the zero level set. Figure 2.2 shows an illustration of the narrow band. The grid points in the dark area are belonged to the narrow band.

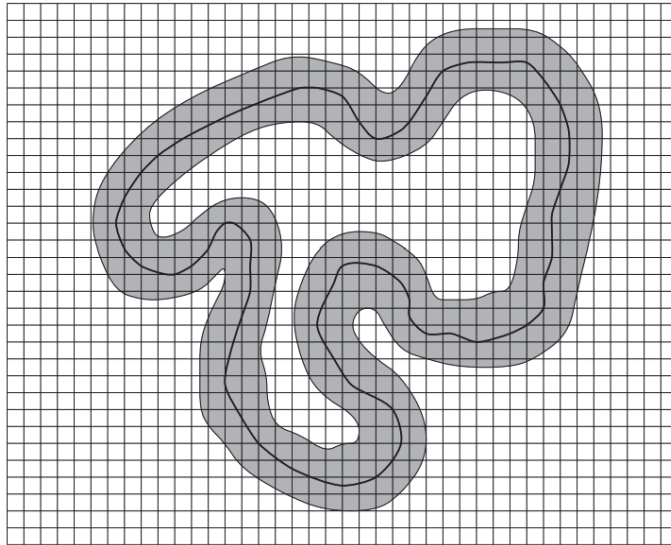


Figure 2.2 Illustration of narrow band [154]

In the implementation of the algorithm, reinitialization [137],[155] is necessary to keep the level set function from being too flat or too steep. Reinitialization

technique has been extensively used to maintain the stability of the curve evolution [156],[157] in traditional level set methods. The reinitialization keeps the level set function as a signed distance function during the curve evolution. The standard reinitialization method is to solve the following equation:

$$\frac{\partial \phi}{\partial t} = \text{sign}(\phi_k)(1 - |\nabla \phi|) \quad (2.9)$$

where $\text{sign}(\cdot)$ is the sign function and ϕ_k is the function to be reinitialized. Fast marching method [158] is used to reinitialize level set function in the proposed algorithm.

2.4.2 Numerical implementation details

The Heaviside function H can be approximated by a smooth function H_ε using the following equation [142]:

$$H_\varepsilon(x) = \frac{1}{2} \left[1 + \frac{2}{\pi} \arctan\left(\frac{x}{\varepsilon}\right) \right] \quad (2.10)$$

and the Dirac function δ is approximated by δ_ε using the following equation:

$$\delta_\varepsilon(x) = H'_\varepsilon(x) = \frac{1}{\pi} \frac{\varepsilon}{\varepsilon^2 + x^2} \quad (2.11)$$

The parameter ε is set as $\varepsilon = 1.0$ here.

A Finite difference scheme [159] is used to calculate the gradient of $\nabla \phi$. Let h be the space step, and x, y be the grid points, the calculation of term $\text{div}\left(\frac{\nabla \phi}{|\nabla \phi|}\right)$ is achieved by using the central difference scheme:

$$\text{div}\left(\frac{\nabla \phi}{|\nabla \phi|}\right) = \frac{\phi_{xx}\phi_y^2 - 2\phi_x\phi_y\phi_{xy} + \phi_{yy}\phi_x^2}{(\phi_x^2 + \phi_y^2)^{3/2}} \quad (2.12)$$

where

$$\begin{aligned} \phi_x &= \frac{\phi_{x+1,y} - \phi_{x-1,y}}{2h}, & \phi_y &= \frac{\phi_{x,y+1} - \phi_{x,y-1}}{2h} \\ \phi_{xx} &= \frac{\phi_{x+1,y} - 2\phi_{x,y} + \phi_{x-1,y}}{h^2}, & \phi_{yy} &= \frac{\phi_{x,y+1} - 2\phi_{x,y} + \phi_{x,y-1}}{h^2} \\ \phi_{xy} &= \frac{\phi_{x+1,y+1} - \phi_{x-1,y+1} - \phi_{x+1,y-1} + \phi_{x-1,y-1}}{4h^2} \end{aligned} \quad (2.13)$$

Upwind scheme [158] is used to calculate the temporal partial derivative $\frac{\partial \phi}{\partial t}$. The level set evolution equation can be expressed in a general form [138]:

$$\frac{\partial \phi}{\partial t} = (F - \lambda \kappa) \|\nabla \phi\| \quad (2.14)$$

where F is a function depending on time and position, λ is a scalar parameter and κ is the curvature of the contour. Let Δt be the time step. The discretization of (2.14) is obtained by:

$$\frac{\phi_{i,j}^{n+1} - \phi_{i,j}^n}{\Delta t} = \max(F, 0) \nabla_{i,j}^+ + \min(F, 0) \nabla_{i,j}^- \quad (2.15)$$

where $\nabla_{i,j}^+$ and $\nabla_{i,j}^-$ is calculated by:

$$\begin{aligned} \nabla_{i,j}^+ &= (\max(D_{i,j}^{-x}, 0)^2 + \min(D_{i,j}^{+x}, 0)^2 + \max(D_{i,j}^{-y}, 0)^2 + \min(D_{i,j}^{+y}, 0)^2)^{1/2} \\ \nabla_{i,j}^- &= (\min(D_{i,j}^{-x}, 0)^2 + \max(D_{i,j}^{+x}, 0)^2 + \min(D_{i,j}^{-y}, 0)^2 + \max(D_{i,j}^{+y}, 0)^2)^{1/2} \end{aligned} \quad (2.16)$$

$D_{i,j}^{+x}$ is the forward difference of x , $D_{i,j}^{-x}$ is the backward difference of x ; $D_{i,j}^{+y}$ is the forward difference of y , $D_{i,j}^{-y}$ is backward difference of y .

Figure 2.3 shows the pseudo-code of the proposed algorithm:

-
- 1) $k=0$, initialize ϕ^k by ϕ_0 .
 - 2) Compute the mean value \mathbf{u} and \mathbf{v} inside and outside the level set according to (2.5).
 - 3) Compute the σ_i and σ_o according to (2.5).
 - 4) Calculate \mathbf{A}_i and \mathbf{A}_o according to (2.8).
 - 5) Evolve the curve according to (2.7) to obtain ϕ^{k+1} .
 - 6) Reinitialize the ϕ^{k+1} by fast marching method.
 - 7) Check if ϕ is convergent. If not, $k=k+1$ and go back to step 2.
-

Figure 2.3. Pseudo-code of the proposed algorithm

2.5 Results

In this section the experimental setup and the evaluation method is described. All the proposed algorithms in this thesis are implemented in Matlab. All experiments are conducted on a PC workstation (Intel Quad Q8300, 8 GB RAM, Windows 7 Professional).

Dice [160] coefficient is used to quantitatively evaluate the performance of the algorithm. The Dice coefficient is defined as:

$$\text{Dice} = \frac{2(A \cap B)}{A \cup B} \quad (2.17)$$

Where A is the reference region and B is the segmentation result of an algorithm. The Dice measurement is often used to measure the accuracy of a segmentation algorithm. The Dice coefficient range is [0, 1]. If there is no overlap between two regions, the Dice value is 0; if two regions are completely overlapping, the Dice value is 1.

A kidney phantom ultrasound image is firstly used to test the performance of the proposed algorithm. An organ phantom is an artificial replica of a real organ routinely used in medical training. It usually has a simplified internal structure and simpler features than the real human organ. The detailed description of the phantom can be found in [161]. Figure 2.4 shows the segmentation result of the proposed algorithm on a kidney phantom ultrasound image with a tumor inside it. The image size is 360*290 pixels. As we can see from Figure 2.4, the border of the tumor is not very clear, but the proposed algorithm can segment the border of the tumor with the Dice value of 0.9198.

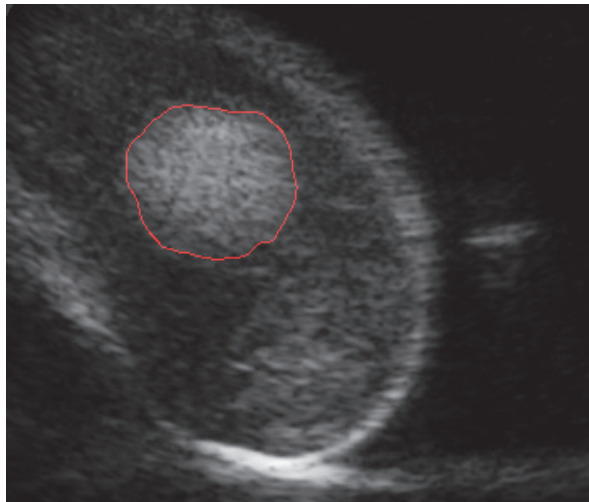
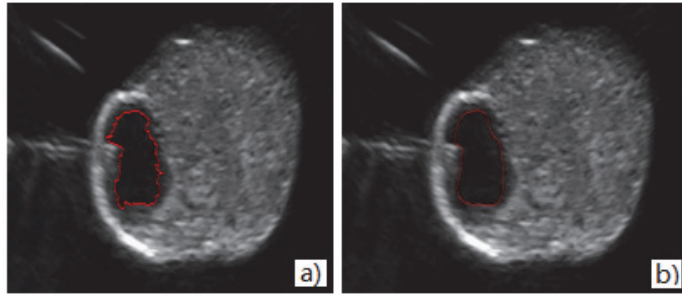
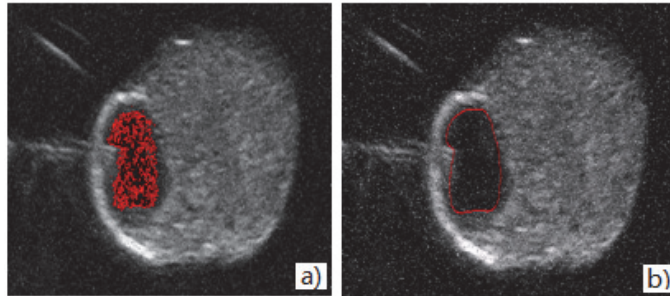


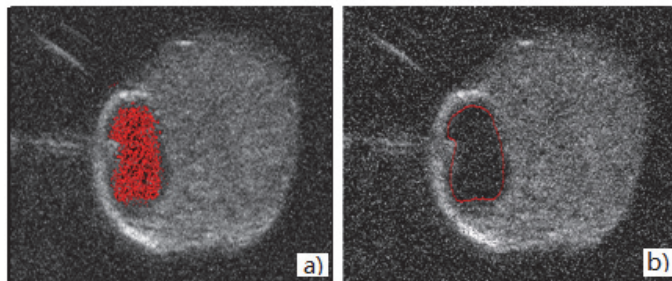
Figure 2.4 Kidney phantom ultrasound image segmentation result



Noise free



Salt-and-pepper noise, $d=0.1$



Salt-and-pepper noise, $d=0.3$

Figure 2.5 Segmentation results for (a) CV algorithm and (b) proposed algorithm

To test the performance of the proposed algorithm, kidney cyst phantom images with different salt-and-pepper noise are used as the evaluation images. The first row of Figure 2.5 shows the original image without adding noise. The image size is 520×230 pixels. Then two different salt-and-pepper densities noise ($d = \{0.1, 0.3\}$) are added to the original image. The larger the value d is, the more noise is added to the image. The first column of Figure 2.5 shows the results of the CV algorithm. As we can see from the segmentation results, when the image is noise free, the CV algorithm works well, but when the amount of noise in the image increases, the performance of the CV algorithm decreases. Figure 2.5 b) shows

the results of the proposed algorithm the same images. The proposed algorithm converges to the desired border even when the image contains high level of noise. From Figure 2.5 b) we can see, even when the image contains high level of noise ($d=0.3$), the proposed algorithm can still produce good result.

In addition to the phantom images, the proposed algorithm is also tested on a patient kidney ultrasound image obtained from East Tallinn Central Hospital, Estonia. Figure 2.6 a) shows the result of the proposed algorithm. The size of the kidney image is 400×240 . Figure 2.6 b) is the reference image which is obtained manually by an expert radiologist. A value of Dice = 0.9263 is found using the proposed approach. The segmentation results of the proposed algorithm on both kidney phantom images and the patient image show that the proposed algorithm can produce good segmentation even through the image is very noisy.



a) Segmentation result of the proposed algorithm



b) Ground truth

Figure 2.6 Kidney ultrasound image segmentation result

The performance of the proposed algorithm is evaluated using 3 types of images: one synthesized ultrasound image (Figure 2.7 b), one ultrasound image of a phantom (Figure 2.4), and one ultrasound image of a patient (Figure 2.6). The

synthesized image is obtained by adding speckle noise to a predefined image (Figure 2.7 a). The variance of speckle noise added into this image is $d=0.1$. The running times, the iteration counts and the Dice values of the proposed algorithm are shown in Table 2.1.

Table 2.1 Performance of the proposed algorithm

Image types	The proposed algorithm		
	Time(s)	Iterations	Dice
Synthetic image (128*64 pixels)	1.574	200	0.9854
Phantom image (360*290 pixels)	14.980	500	0.9198
Patient image (400*240 pixels)	120.059	4000	0.9263

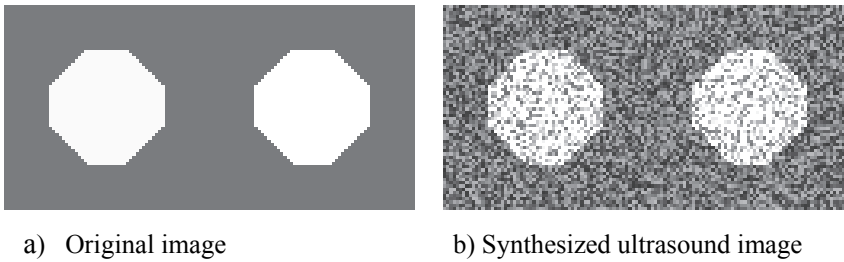


Figure 2.7 Synthesized images

The proposed method improves the segmentation accuracy compared to the CV algorithm because in the proposed algorithm, not only the mean value is considered, but also the variance value is considered. While in the CV algorithm, only the mean value is considered and it cannot provide enough image intensity information. Therefore, some images with intensity inhomogeneity the CV algorithm can give inaccurate segmentation results.

2.6 Conclusions

In this section, the limitations of CV algorithm on inhomogeneous image are discussed. Then an algorithm which combines the CV algorithm with Bhattacharyya distance is proposed to solve segmentation problem of the inhomogeneous image. The Rayleigh distribution is used in the Bhattacharyya distance. Combining the Bhattacharyya distance with the CV algorithm, the proposed algorithm is capable of segmenting inhomogeneous images. Synthesized ultrasound image, phantom ultrasound images and patient ultrasound image are used to test the performance of the proposed algorithm. Compared to the CV algorithm, the proposed algorithm is more robust and provides improved segmentation results.

3 Localized active contour segmentation

Ultrasound images usually contain a lot of noise and the granular texture of the ultrasound image makes the segmentation a challenging task. Different algorithms for ultrasound image segmentation have been proposed in literature [21],[162]. In this chapter, a localized active contour algorithm is introduced and then novel algorithms based on the localized active contour algorithms using the Rayleigh distribution and the shifted Rayleigh distribution are proposed for ultrasound image segmentation. The algorithms described in this chapter are related to publication C.

3.1 Localized region based active contour algorithm

Region based active contours have several advantages and have been successfully applied for medical image segmentation. The region based approaches are usually derived under the assumption that the region of interest can be separated by using the global statistical information. But when the image is inhomogeneous, for example when the intensity profile of a target contains a lot of noise, the traditional active contour algorithm may produce incorrect segmentation results. In literature, many studies focus on an alternative way of image segmentation by using the local region in the segmentation process [163]–[165].

A localized active contour algorithm has been proposed in [166], in which a level set formulation is implemented, and a localized region factor is utilized. The localized active contour is based on the assumption that, if the global homogeneity requirement is not satisfied in a region, there is a high probability that it can be satisfied in a small sub region. In the localized active contour algorithm, a localized factor is defined as:

$$W(x,y)=\begin{cases} 1, & ||x - y| < r \\ 0, & \text{otherwise} \end{cases} \quad (3.1)$$

where x, y represents a point in Ω respectively and r represents a radius parameter. Figure 3.1 describes the concept of the localized active contour algorithm. In the localized region representation, the region inside the curve is represented by $W(x, y) \cdot H(\phi(x, y))$ whereas the region outside of the curve is represented by $W(x, y) \cdot (1 - H(\phi(x, y)))$.

In localized active contour algorithm, the foreground and background regions are not represented by global statistical information. The localized active contour uses a small region in the curve evolution. For each point along the curve, its neighborhood regions are split into two parts: interior and exterior region. The energy optimization is calculated at each single point. The general form of the localized active contour energy function can be written as:

$$E = \int \delta(\phi(x)) \left\{ \int W(x, y) F(I(y), \phi(x)) dy \right\} dx + \mu \int \delta(\phi(x)) \|\nabla\phi(x)\| dx \quad (3.2)$$

The above equation provides a simple way to transform the region based criterion to its localized counterpart. Using equation (3.2), the curve evolution of the localized active contour can be calculated.

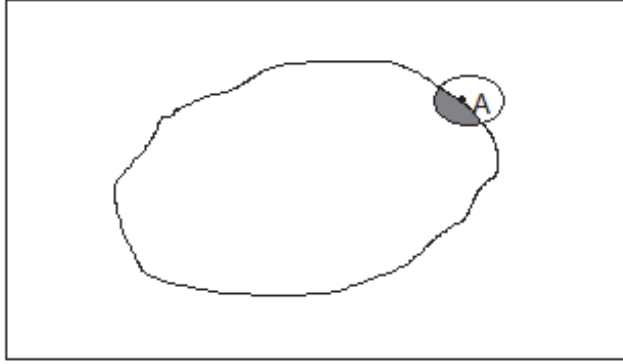


Figure 3.1 Localized active contour algorithm

3.2 Novel contribution : Localized active contour with Rayleigh distribution

As mentioned before, due to the presence of the speckle noise in ultrasound image, the standard image processing technics are usually ineffective for segmenting ultrasound image. One way to improve the result is to adopt the ultrasound image statistical properties into the evolution criterion for the segmentation problem.

Using the localized active contour with the statistical intensity distribution of the ultrasound image, the energy function of the localized active contour becomes:

$$E = \int \delta(\phi(x)) \left\{ \int W(x, y) P_{in}(I) dy + \int W(x, y) P_{out}(I) dy \right\} dx + \mu \int \delta(\phi(x)) \|\nabla\phi(x)\| dx \quad (3.3)$$

where $P_{in}(I)$ and $P_{out}(I)$ is referred as to the intensity distribution of the region inside and outside the curve, respectively.

From equation (3.3) we can see that it is crucial to determine $P_{in}(I)$ and $P_{out}(I)$ to achieve successful segmentation results. Different ultrasound image intensity distributions were introduced in Chapter 1. Section 1.3.3 points out that the display image follows the Fisher-Tippett distribution. The Fisher-Tippett distribution has a very complicated analytical expression and difficult to implement. Rayleigh distribution is commonly used as the image intensity distribution for ultrasound envelope-detected image and has a simple analytical expression. Therefore, Rayleigh distribution is chosen as the image intensity distribution here. An algorithm using the localized active contour by Rayleigh distribution is proposed. Since the Rayleigh distribution is used to approximate the display image intensity distribution, it has a bias from the true image intensity distribution. The shifted Rayleigh distribution has been used as the ultrasound image intensity distribution in literature [21],[167]. Therefore, another algorithm is proposed using the shifted Rayleigh distribution in the same localized active contour framework and the segmentation results between these two algorithms are compared in this section. The relation between the Rayleigh distribution and the shifted Rayleigh distribution is shown in Figure 3.2.

The parameters estimation of the Rayleigh distribution is usually obtained by maximum likelihood method. The maximum likelihood estimation for the Rayleigh distribution parameters will be firstly introduced in next section and then the localized Rayleigh active contour (LRAC) algorithm and the Localized shifted Rayleigh active contour (LSRAC) algorithm will be presented.

3.2.1 Maximum a posteriori estimation

The image segmentation problem can be expressed by the Bayesian maximum *a posteriori* (MAP) estimation. The MAP estimates the possible partitions of a given image I by [138]:

$$\hat{\mathcal{P}}_{\Omega} = \arg \max_{\mathcal{P}_{\Omega}} P(\mathcal{P}_{\Omega}|I) = \arg \max_{\mathcal{P}_{\Omega}} P(I|\mathcal{P}_{\Omega})P(\mathcal{P}_{\Omega}) \quad (3.4)$$

By taking the negative of the logarithm of equation (3.4) and assuming the image partitions R_k are conditionally independent from each other, the following equation is obtained which converts the Bayesian estimation (3.4) into minimization problem:

$$\hat{\mathcal{P}}_{\Omega} = \arg \min_{\mathcal{P}_{\Omega}} \sum_i \int_{R_i} -\log P(I|R_i) dx - \log P(\mathcal{P}_{\Omega}) \quad (3.5)$$

The equation (3.5) is the general function for most of the variational segmentation algorithms. The first term is the data term which measures the likelihood of the image. The image is modeled by a specified distribution which is generally a parametric distribution. The region R_i is characterized by the estimation of the parameters in the distribution.

As mentioned in the chapter 2, Rayleigh distribution is commonly used as the intensity distribution for the ultrasound envelope-detected image. For an image I , the corresponding Rayleigh distribution is:

$$P(I) = \frac{I}{\sigma^2} \exp\left(-\frac{I^2}{2\sigma^2}\right) \quad (3.6)$$

where σ^2 is the parameter of the Rayleigh distribution.

For a curve dividing the image I into regions R_i , $i \in 1, 2$, the Rayleigh distribution with parameter σ_i^2 is:

$$P_{Rayleigh}(I|R_i) = \frac{I}{\sigma_{R_i}^2} \exp\left(-\frac{I^2}{2\sigma_{R_i}^2}\right) \quad (3.7)$$

Calculating the negative logarithm of the data term in (3.5) by using the Rayleigh distribution, the following equation is obtained:

$$\mathcal{L} = \sum_i \int_{R_i} G(I, \sigma_{R_i}^2) dx \quad (3.8)$$

with

$$\begin{aligned} G(I, \sigma_{R_i}^2) &= -\log P_{Rayleigh}(I|R_i) \\ &= \log \sigma_{R_i}^2 + \frac{I^2}{2\sigma_{R_i}^2} \end{aligned} \quad (3.9)$$

The optimization of parameter $\sigma_{R_i}^2$ is obtained by using the ML method:

$$\sigma_{R_i}^2 = \frac{\int_{R_i} I^2 dx}{2 \int_{R_i} dx} \quad (3.10)$$

3.2.2 Localized Rayleigh active contour

The Rayleigh distribution has been widely applied in ultrasound image segmentation. The Rayleigh distribution has a simple analytical form which makes it easy to calculate the integrals of the segmentation flow. In general, using the Rayleigh distribution the following energy function is obtained:

$$E = \log P_{in} + \log P_{out} + \mu \text{length}(c) =$$

$$\int_{\Omega_{in}} \log P_{in}(I) dx dy + \int_{\Omega_{out}} \log P_{out}(I) dx dy + \mu \int_{\Omega_{\Gamma}} dx dy \quad (3.11)$$

The level set equation is derived as:

$$\frac{\partial \phi}{\partial t} = \delta(\phi) \left(\mu \text{div} \left(\frac{\nabla \phi}{|\nabla \phi|} \right) + \log \frac{\sigma_{in}}{\sigma_{out}} + \frac{I^2}{\sigma_{in}^2} - \frac{I^2}{\sigma_{out}^2} \right) \quad (3.12)$$

Using the localized factor $W(x, y)$, the curve evolution for the localized Rayleigh active contour (LRAC) algorithm is calculated as:

$$\begin{aligned} \frac{\partial \phi}{\partial t} = \delta(\phi(x)) \int W(x, y) \delta(\phi(y)) \left(\log \frac{\sigma_{in}}{\sigma_{out}} + \frac{I(y)^2}{\sigma_{in}^2} - \frac{I(y)^2}{\sigma_{out}^2} \right) dy \\ + \mu \delta(\phi(x)) \text{div} \left(\frac{\nabla \phi(x)}{|\nabla \phi(x)|} \right) \end{aligned} \quad (3.13)$$

The parameters σ_{in}^2 and σ_{out}^2 in the LRAC algorithm are calculated by:

$$\begin{aligned} \sigma_{in}^2 &= \frac{\int_{\Omega} W(x, y) I^2 H(\phi(x, y)) dx dy}{2 \int_{\Omega} W(x, y) H(\phi(x, y)) dx dy} \\ \sigma_{out}^2 &= \frac{\int_{\Omega} W(x, y) I^2 H(1 - \phi(x, y)) dx dy}{2 \int_{\Omega} W(x, y) H(1 - \phi(x, y)) dx dy} \end{aligned} \quad (3.14)$$

3.2.3 Localized shifted Rayleigh active contour

Some approaches [114],[168] use shifted Rayleigh distribution as the intensity statistical distribution of ultrasound image. In this section, ultrasound image segmentation by using the shifted Rayleigh distribution is investigated. The shifted Rayleigh distribution is defined as:

$$p(I) = \frac{(I - u)}{\sigma^2} \exp\left(-\frac{(I - u)^2}{2\sigma^2}\right) \quad (3.15)$$

where the parameter u is calculated by using the mean intensity of the region. Figure 3.2 shows the relation between standard Rayleigh distribution and the shifted Rayleigh distribution.

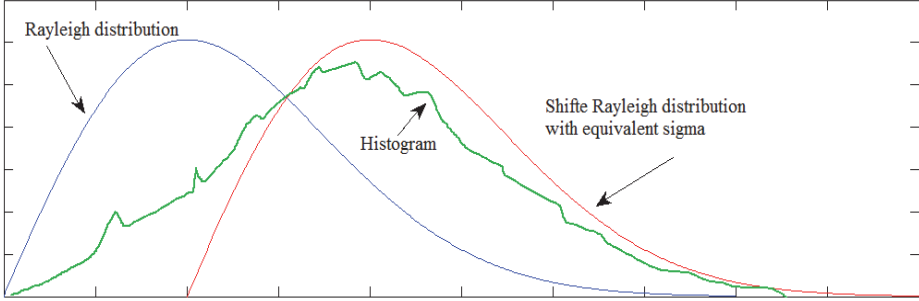


Figure 3.2 Shifted Rayleigh distribution

The active contour energy function of the shifted Rayleigh distribution is similar to the Rayleigh distribution:

$$E = \log P_{in} + \log P_{out} + \mu \text{length}(c) =$$

$$\int_{\Omega_{in}} \log P_{in}(I) dx dy + \int_{\Omega_{out}} \log P_{out}(I) dx dy + \mu \int_{\Omega_{\Gamma}} dx dy \quad (3.16)$$

The level set equation of the shifted Rayleigh distribution is derived as:

$$\frac{\partial \phi}{\partial t} = \delta(\phi) \left(\mu \text{div} \left(\frac{\nabla \phi}{|\nabla \phi|} \right) + \log \frac{\sigma_{in}}{\sigma_{out}} + \frac{(I - u_{in})^2}{\sigma_{in}^2} - \frac{(I - u_{out})^2}{\sigma_{out}^2} \right) \quad (3.17)$$

where u_{in} is the mean intensity inside of the curve ϕ and u_{out} is the mean intensity outside of the curve ϕ .

By incorporating localized factor into the energy function (3.17), the evolution function for the localized shifted Rayleigh active contour (LSRAC) can be calculated as:

$$\begin{aligned} \frac{\partial \phi}{\partial t}(x) = & \delta(\phi(x)) \int W(x,y) \delta(\phi(y)) \cdot \left(\log \frac{\sigma_{in}}{\sigma_{out}} + \frac{(I(y) - u_{in})^2}{\sigma_{in}^2} \right. \\ & \left. - \frac{(I(y) - u_{out})^2}{\sigma_{out}^2} \right) dy + \mu \delta(\phi(x)) \operatorname{div} \left(\frac{\nabla \phi(x)}{|\nabla \phi(x)|} \right) \end{aligned} \quad (3.18)$$

The parameter u_{in} and u_{out} in (3.18) is obtained by:

$$\begin{aligned} u_{in} &= \frac{\int_{\Omega} W(x,y) I H(\phi(x,y)) dx dy}{\int_{\Omega} W(x,y) H(\phi(x,y)) dx dy} \\ u_{out} &= \frac{\int_{\Omega} W(x,y) I H(1 - \phi(x,y)) dx dy}{\int_{\Omega} W(x,y) H(1 - \phi(x,y)) dx dy} \end{aligned} \quad (3.19)$$

The parameter σ_{in} and σ_{out} in (3.18) is calculated by:

$$\begin{aligned} \sigma_{in}^2 &= \frac{\int_{\Omega} W(x,y) (I - u_{in})^2 H(\phi(x,y)) dx dy}{2 \int_{\Omega} W(x,y) H(\phi(x,y)) dx dy} \\ \sigma_{out}^2 &= \frac{\int_{\Omega} W(x,y) (I - u_{out})^2 H(1 - \phi(x,y)) dx dy}{2 \int_{\Omega} W(x,y) H(1 - \phi(x,y)) dx dy} \end{aligned} \quad (3.20)$$

3.3 Implementation

The proposed algorithm is implemented in a level set framework. To improve the efficiency, narrow band method is used. Fast marching method is applied to prevent the level set from being too flat or too steep. The numerical implementation of level set has been discussed in section 2.4.

In the proposed localized active contour algorithm, the local region statistical properties are calculated at each point along the contour. The calculation of local region statistical properties consists of two parts: initialization and update. In the initialization step, the local interior and exterior statistics of each pixel in the narrow band are calculated. When the narrow band moves across a pixel which is uninitialized, the local region statistical properties of this pixel will be initialized. The initialization operation is performed only once for each pixel. The update step happens when a initialized pixel along the contour is moved by the contour from the exterior to the interior or vice versa. When the contour moves across a pixel, the local statistical properties of all pixels within the $W(x,y)$ of this pixel are updated.

The pseudo-code of the LRAC algorithm is shown in Figure 3.3. The LSRAC algorithm is implemented in a similar way.

-
- 1) $k=0$, initialize ϕ^k by ϕ_0 .
 - 2) Compute the value σ_{in} and σ_{out} inside and outside the level set ϕ^k according to (3.14).
 - 3) Evolve the contour according to (3.13) to obtain ϕ^{k+1} .
 - 4) Reinitialize the ϕ^{k+1} by fast marching method.
 - 5) Check if ϕ is convergent. If not, $k = k+1$ and go back to step 2.
-

Figure 3.3 Pseudo-code of the LRAC algorithm

3.4 Results

In this section, the segmentation results of the proposed two algorithms are presented. The algorithms are implemented in Matlab and executed on a PC workstation (Intel Quad Q8300, 8 GB RAM, Windows 7 Professional), as in section 2. The Dice coefficient is used as the quantitative evaluation method.

Synthesized images are used to test the performance of the proposed two algorithms. One synthesized image is generated and shown in the first row of Figure 3.4. The size of the synthesized image is 128*64 pixels. Gaussian noise with different variances ($v1=0.1$, $v2=0.2$, $v3=0.3$) are added into this image. The segmentation results of the LRAC algorithm and LSRAC algorithm on the synthesized images are shown in the second and the third column in Figure 3.4. As we can see from the segmentation results, both LRAC and LSRAC algorithm can produce reasonable segmentation results. Table 3.1 shows the Dice values of LRAC and LSRAC algorithm on the synthetic images.

Table 3.1 Dice values of the proposed algorithms

Values of Gaussian Noise added	LRAC	LSRAC
0.1	0.9632	0.9615
0.2	0.9578	0.9674
0.3	0.9285	0.9431

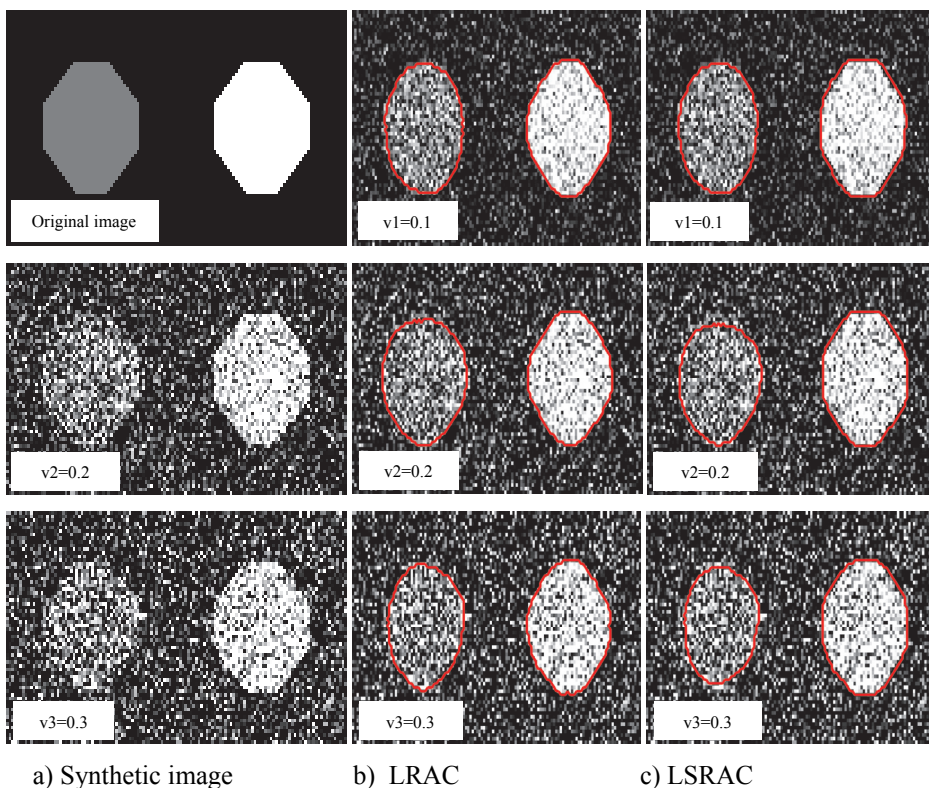


Figure 3.4 Segmentation results of the synthesized images

A kidney phantom ultrasound image (520*230 pixels) with a cyst inside it is used to test the performance of the proposed two algorithms. The segmentation result of LRAC is shown in Figure 3.5 a). The segmentation result of LSRAC is shown in Figure 3.5 b).

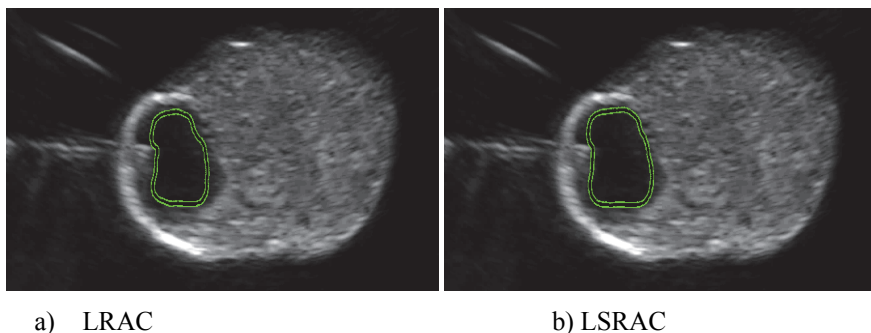


Figure 3.5 Segmentation results of ultrasound image without noise

Salt-and-paper noise (noise density $d=0.1$) is added to Figure 3.5 to test the capability of the proposed algorithms. The segmentation result of LRAC is shown in Figure 3.6 a). The segmentation result of LSRAC is shown in Figure 3.6 b). From the segmentation results we can see that the proposed algorithms work efficiently on both images.

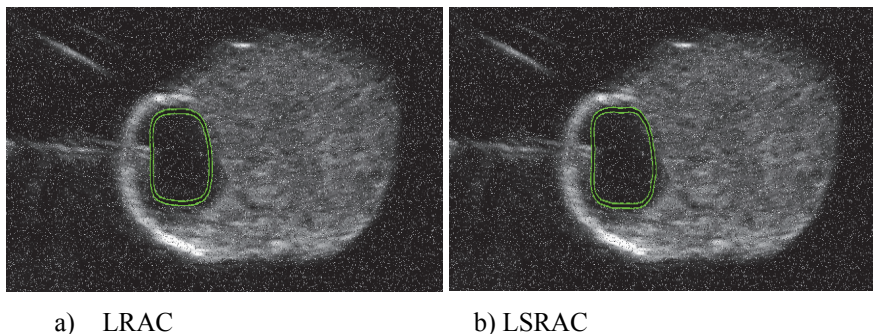


Figure 3.6 Segmentation results of ultrasound image with noise

Ten kidney phantom ultrasound images (251*201 pixels) with a tumor inside are used to test the performance of the proposed two algorithms. Figure 3.7 shows one of these images. For a kidney phantom ultrasound image with a tumor, the segmentation is more difficult because the edge of the tumor is not very clear. The segmentation of LRAC algorithm on the tumor image is shown in Figure 3.7 a). Figure 3.7 b) shows the segmentation of LSRAC algorithm on the same image. Table 3.2 shows the average Dice values of LRAC algorithm and LSRAC algorithm respectively. From Table 3.2, we can see that the LSRAC algorithm obtain better segmentation results compared to the LRAC algorithm on the kidney phantom ultrasound images.

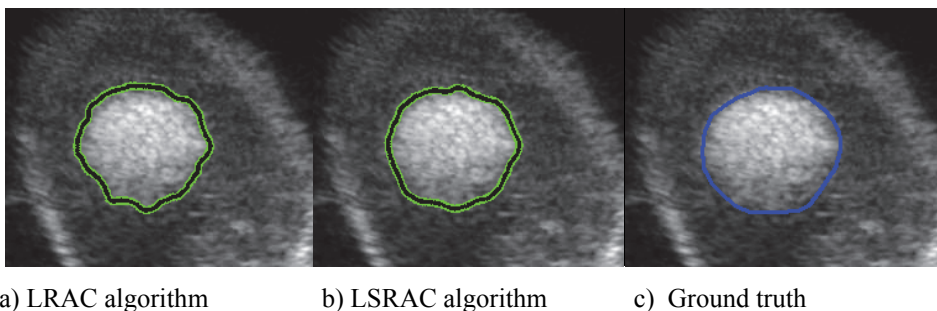
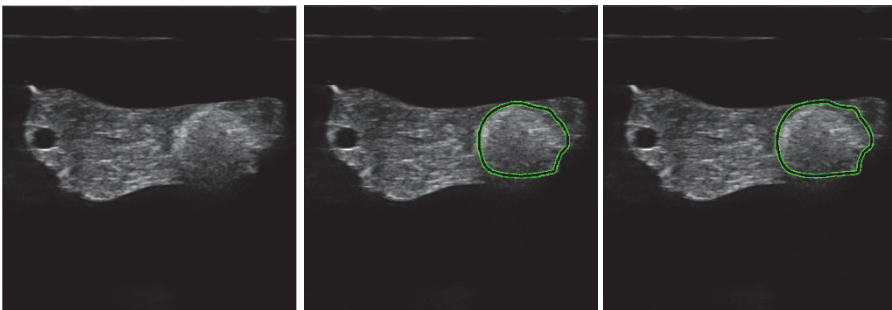


Figure 3.7 Segmentation results of kidney tumor phantom ultrasound image

Table 3.2 LRAC and LSRAC segmentation results

Algorithm	Dice
LRAC	0.9093
LSRAC	0.9452

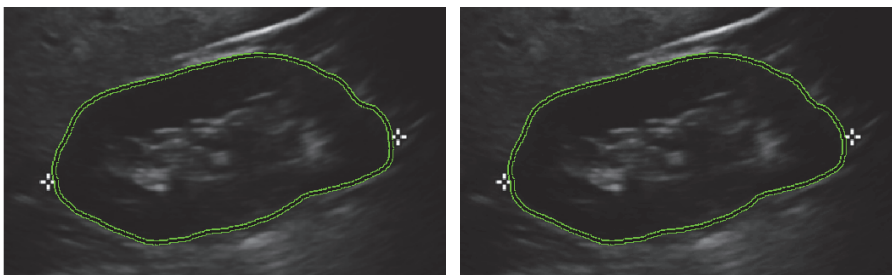
Figure 3.8 b) shows the segmentation result of the LRAC algorithm on a pancreas phantom ultrasound image with a tumor and Figure 3.8 c) shows the segmentation result of LSRAC algorithm on the same image. The image size is 395*408 pixels.



a) Original image b) LRAC algorithm c) LSRAC algorithm

Figure 3.8 Segmentation results of pancreas tumor phantom ultrasound image

Figure 3.9 a) shows the segmentation result of the LRAC algorithm on a patient kidney ultrasound image (400*240 pixels) and Figure 3.9 b) shows the segmentation result of the LSRAC algorithm on the same image. The segmentation result shows that both the LRAC algorithm and the LSRAC algorithm can produce desirable segmentation result.



a) LRAC algorithm b) LSRAC algorithm

Figure 3.9 Segmentation results of patient ultrasound image

Similar to chapter 2, the performance of the proposed algorithms is also evaluated by three types of images: one synthesized ultrasound image (Figure 2.7 b), one ultrasound image of a phantom (Figure 3.8), and one ultrasound image of a patient (Figure 3.9). Table 3.3 shows the evaluation results of the LRAC algorithm and the LSRAC algorithm including the running time, the iteration counts and the Dice values.

Table 3.3 Performance of the LRAC algorithm and the LSRAC algorithm

Image types	LRAC			LSRAC		
	Time(s)	Iterations	Dice	Time(s)	Iterations	Dice
Synthetic image (128*64 pixels)	20.538	300	0.9906	22.140	300	0.9877
Phantom image (395*408 pixels)	37.863	300	0.8866	38.623	300	0.9060
Patient image (400*240 pixels)	179.843	1000	0.9037	186.593	1000	0.9146

From above segmentation results, the LSRAC algorithm in general has better segmentation performance with higher Dice values than the LRAC algorithm. The reason is because the LSRAC considers both the mean μ and the variance σ of an image in the segmentation process while the LRAC only uses the variance σ of an image.

3.5 Conclusions

In this section, a localized region based active contour algorithm is introduced. Then a localized active contour method with Rayleigh distribution (LRAC) is proposed to solve the segmentation problem of ultrasound images. Another localized active contour algorithm with shifted Rayleigh distribution (LSRAC) is also proposed. The performances of the LRAC algorithm and the LSRAC algorithm are evaluated on synthetic ultrasound images, phantom ultrasound images and patient kidney ultrasound image. From the segmentation results, both algorithms can work well on the synthetic ultrasound images, phantom ultrasound images and patient ultrasound image. In general, segmentation results of the LSRAC algorithm are more accurate compared to the LRAC algorithm.

4 Localized region scalable fitting and the Bhattacharyya distance

Due to the noise in the ultrasound images, the ultrasound images are usually inhomogeneous. For an inhomogeneous image, the boundary of a heterogeneous object is difficult to segment. The global region methods do not always generate satisfactory results in an inhomogeneous image. The localized active contour method is able to segment objects with inhomogeneous features, which is difficult otherwise if a global method is used [166]. In section 3 showed that using the local region information can improve the segmentation results. In this chapter an alternative way of localized active contour method is introduced. The algorithm described in this chapter is related to publication A.

4.1 Region scalable fitting algorithm

In [169] a region scalable fitting (RSF) algorithm is proposed to solve the segmentation problem of inhomogeneous images. A kernel factor is used in the RSF algorithm. The RSF algorithm is capable of solving the segmentation problem of inhomogeneous images. The results of the RSF algorithm show that the RSF algorithm is able to deal with noisy images. The general energy function of the RSF model is:

$$E = \gamma_i \iint_{\Omega_i} k(x, y) (I(y) - f_i)^2 dydx + \gamma_o \iint_{\Omega_o} k(x, y) (I(y) - f_o)^2 dydx \quad (4.1)$$

where γ_i and γ_o are scale parameters; $k(x, y)$ is the kernel function and a Gaussian kernel function k_σ is used in [169]; f_i and f_o are the functions approximating the intensities inside and outside of the curve respectively. The calculation of f_i and f_o are obtained by using following equations:

$$f_i = \frac{\int_{\Omega} k_\sigma(x - y) I(y) H(\phi) dy}{\int_{\Omega} k_\sigma(x - y) H(\phi) dy}$$

$$f_o = \frac{\int_{\Omega} k_\sigma(x - y) I(y) (1 - H(\phi)) dy}{\int_{\Omega} k_\sigma(x - y) (1 - H(\phi)) dy} \quad (4.2)$$

The kernel function k_σ plays an important role in the RSF algorithm. The kernel function k_σ is non-negative and has the following properties:

1. $k_\sigma(-u) = k_\sigma(u)$
2. $k_\sigma(u) \geq k_\sigma(v)$, if $|u| < |v|$, and $\lim_{|u| \rightarrow \infty} k_\sigma(u) = 0$
3. $\int k_\sigma(x) dx = 1$

In RSF algorithm, the image intensities are calculated in a local region centered at the point x , and the size of the region is controlled by the kernel function k_σ . The choice of the kernel function is flexible and usually a Gaussian kernel is chosen:

$$k_\sigma = \frac{1}{(2\pi)^{n/2}\sigma^n} e^{-|u|^2/2\sigma^2} \quad (4.3)$$

The kernel function k_σ is a local factor and the contribution of intensity $I(y)$ decreases as y moves away from the center point x . Therefore the kernel function k_σ acts like a low pass filter. The value of Gaussian kernel $k_\sigma(x - y)$ function drops significantly to zero as y moves away from x [169].

While the image is not very noisy, the RSF algorithm can produce good segmentation results. However, for an extremely inhomogeneous image, the RSF algorithm could not provide a desirable segmentation result. Figure 4.1 shows an example of such a case.

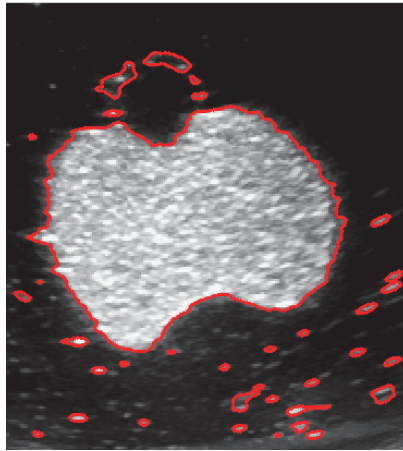


Figure 4.1 RSF algorithm on noisy image

In section 3 a localized active contour algorithm using localized factor $W(x,y)$ was discussed. The localized factor $W(x,y)$ considers the neighbor region around the center point x . Since the kernel function k_σ in the RSF algorithm and the localized factor $W(x,y)$ are both local region factors, the intuitive idea is to see if

using the localized factor in the RSF algorithm can improve the segmentation result. This leads to the proposed algorithm presented in next section.

4.2 Novel contribution: Localized RSF algorithm

As discussed in section 4.1, for a very inhomogeneous image, the RSF algorithm cannot successfully produce desirable results. Considering that using the localized factor $W(x,y)$ can increase the segmentation results in chapter 3, in this section, a new algorithm which combines the RSF algorithm and the localized factor will be presented.

Here, the RSF energy function is written as:

$$E_R = \gamma_i \iint_{\Omega_i} k_g(x-y)(I(y) - u_i)^2 dydx + \gamma_o \iint_{\Omega_o} k_g(x-y)(I(y) - u_o)^2 dydx \quad (4.4)$$

where k_g is the Gaussian kernel function. The u_i and u_o are the mean values inside and outside of the curve, respectively.

The localized factor $W(x,y)$ is written as k_u here. Using localized factor k_u and approximating the Heaviside function H by H_ε , the localized RSF energy function is written as:

$$E_R(\phi) = \gamma_i \iint_{\Omega} k_u(x-y)(I(y) - u_i)^2 H_\varepsilon(\phi) dydx + \gamma_o \iint_{\Omega} k_u(x-y)(I(y) - u_o)^2 (1 - H_\varepsilon(\phi)) dydx \quad (4.5)$$

The u_i and u_o are calculated by using the localized factor k_u as follows:

$$u_i = \frac{\int_{\Omega_i} k_u(x-y)I(y)dy}{\int_{\Omega_i} k_u(x-y)dy}$$

$$u_o = \frac{\int_{\Omega_o} k_u(x-y)I(y)dy}{\int_{\Omega_o} k_u(x-y)dy} \quad (4.6)$$

In section 2, the Bhattacharyya distance was discussed to measure the difference between the internal and external regions. In this algorithm, the Bhattacharyya distance measurement is added into the energy function (4.5) to improve the segmentation results. Gaussian distribution is used as the image intensity distribution to calculate the Bhattacharyya distance. The Bhattacharyya distance can be calculated by using the following equation:

$$D_g = \frac{1}{4} \ln \left\{ \frac{1}{4} \left(\frac{\sigma_i^2}{\sigma_o^2} + \frac{\sigma_o^2}{\sigma_i^2} + 2 \right) \right\} + \frac{1}{4} \left\{ \frac{(u_i - u_o)^2}{\sigma_i^2 + \sigma_o^2} \right\} \quad (4.7)$$

where u_i and u_o are the mean values of the two regions and σ_i^2 and σ_o^2 are the variances of those regions.

The calculation of parameters u_i, u_o, σ_i^2 and σ_o^2 are also obtained by using the localized factor k_u . The u_i and u_o are obtained by equation (4.6) and σ_i^2 and σ_o^2 are calculated as follows:

$$\sigma_i^2 = \frac{\int_{\Omega} k_u(x-y)(I(y) - u_i)^2 H_{\varepsilon}(\phi) dy}{\int_{\Omega} k_u(x-y) H_{\varepsilon}(\phi) dy}$$

$$\sigma_o^2 = \frac{\int_{\Omega} k_u(x-y)(I(y) - u_o)^2 (1 - H_{\varepsilon}(\phi)) dy}{\int_{\Omega} k_u(x-y)(1 - H_{\varepsilon}(\phi)) dy} \quad (4.8)$$

Regularization is an important part for active contour method. The role of regularization in the level set algorithm is to smoothen the curves and is necessary for the curve to achieve correct results. The regularization term of the energy function is calculated as follows:

$$E_p = \frac{1}{2} \eta_1 \int_{\Omega} (|\nabla \phi(x)| - 1)^2 dx + \frac{1}{2} \eta_2 \int_{\Omega} |\nabla H(\phi(x))| dx \quad (4.9)$$

where η_1 and η_2 are scale parameters. The first part of the above equation is to penalize the level set deviation from a signed distance function [170]. The second term is to penalize the length to smoothen the curve during evolution as in most of the active contour methods.

A new active contour algorithm is derived here which combines the localized RSF algorithm, the Bhattacharyya distance and the regularization. The total energy function of the proposed algorithm is:

$$E = (1 - \beta)E_R + \beta E_B + E_p \quad (4.10)$$

where β is a scale parameter, the E_R is the localized RSF term obtained by (4.5), E_B is the Bhattacharyya distance term obtained by (4.7), and E_p is the regularization term calculated by (4.9).

The level set equation of (4.10) is derived as:

$$\frac{\partial \phi}{\partial t} = -\delta_{\varepsilon}(1 - \beta)(\gamma_i e_1 - \gamma_o e_2) + \beta e_B + e_p \quad (4.11)$$

According to [171] the calculation of e_1 and e_2 can be achieved by using convolution. Therefore e_1 can be re-written as:

$$\begin{aligned} e_1 &= \int_{\Omega} k_g(x-y) ((I(y) - u_i)^2) dy \\ &= I(y)^2 [k_g(x) * 1] - 2I(y) [k_g(x) * u_i] + k_g(x) * u_i^2 \end{aligned} \quad (4.12)$$

and e_2 can be re-written as:

$$\begin{aligned} e_2 &= \int_{\Omega} k_g(x-y) ((I(y) - u_o)^2) dy \\ &= I(y)^2 [k_g(x) * 1] - 2I(y) [k_g(x) * u_o] + k_g(x) * u_o^2 \end{aligned} \quad (4.13)$$

e_B is the Bhattacharyya term which is calculated as:

$$e_B = \frac{1}{4} \ln \left\{ \frac{1}{4} \left(\frac{\sigma_i^2}{\sigma_o^2} + \frac{\sigma_o^2}{\sigma_i^2} + 2 \right) \right\} + \frac{1}{4} \left\{ \frac{(u_i - u_o)^2}{\sigma_i^2 + \sigma_o^2} \right\} \quad (4.14)$$

The regularization e_p is calculated as:

$$e_p = \eta_1 \left(\Delta \phi - \operatorname{div} \left(\frac{\nabla \phi}{|\nabla \phi|} \right) \right) + \eta_2 \delta_{\varepsilon} \operatorname{div} \left(\frac{\nabla \phi}{|\nabla \phi|} \right) \quad (4.15)$$

The parameters u_i , u_o , σ_i^2 and σ_o^2 in (4.13), (4.14) and (4.15) are calculated by using convolution:

$$\begin{aligned} u_i &= \frac{k_u(x-y) * [I(y)H_{\varepsilon}(\phi)]}{k_u(x-y) * H_{\varepsilon}(\phi)} \\ u_o &= \frac{k_u(x-y) * [I(y)(1 - H_{\varepsilon}(\phi))]}{k_u(x-y) * (1 - H_{\varepsilon}(\phi))} \\ \sigma_i^2 &= \frac{k_u(x-y) * [(I(y) - u_i)^2 H_{\varepsilon}(\phi)]}{k_u(x-y) * H_{\varepsilon}(\phi)} \\ \sigma_o^2 &= \frac{k_u(x-y) * [(I(y) - u_o)^2 (1 - H_{\varepsilon}(\phi))]}{k_u(x-y) * (1 - H_{\varepsilon}(\phi))} \end{aligned} \quad (4.16)$$

4.4 Implementation

As mentioned in section 2.4, the reinitialization is important to reshape the degraded level set function and maintain the stability of the level set. In [170] proposed a variational formulation to regularize the level set function during the evolution, and the reinitialization step is eliminated. This variational level set method without reinitialization is easy to implement compared to the traditional level set methods. The proposed algorithm in this chapter is implemented using the variational level set without reinitialization technique. The upwind scheme is not needed in the proposed algorithm.

The variational level set without reinitialization proposed using the following equation to penalize the level set function and therefore no reinitialization is needed:

$$P(\phi) = \frac{1}{2} \int_{\Omega} (|\nabla\phi| - 1)^2 dx dy \quad (4.17)$$

Let τ be the time step, the update of ϕ^{n+1} is obtained by:

$$\phi^{n+1} = \phi^n + \tau \Delta \phi^n \quad (4.18)$$

where Δ is the Laplacian operator.

The pseudo-code of the proposed algorithm is outlined in Figure 4.2:

-
- 1) $k=0$, initialize ϕ^k by ϕ_0 .
 - 2) Compute the \mathbf{u}_i, σ_i^2 and \mathbf{u}_o, σ_o^2 according to (4.16).
 - 3) Compute the \mathbf{e}_1 and \mathbf{e}_2 according to (4.12) and (4.13).
 - 4) Compute the \mathbf{e}_B according to (4.14).
 - 5) Compute the term \mathbf{e}_p by (4.15).
 - 6) Evolve the curve ϕ^k by (4.11) to obtain ϕ^{k+1} .
 - 7) Check if ϕ is convergent. If not, $k=k+1$ and go back to step 2.
-

Figure 4.2 Pseudo-code of the proposed algorithm

4.5 Results

The proposed algorithm is implemented in Matlab and the experimental platform is the same as in section 2. The performances of the proposed algorithm are quantitatively measured by calculating the Dice coefficient and the root-mean-squared error of pairs of images (the segmented image and the ground-truth image).

The root-mean-squared error (RMSE) [172] measures the distance between the segmented contour and the ground truth contour. The RMSE is defined as:

$$RMSE = \sqrt{\frac{\sum_{i=0}^{n-1} [(x_i - \bar{x}_i)^2 + (y_i - \bar{y}_i)^2]}{n}} \quad (4.19)$$

where x_i and y_i are the points on the segmented image; \bar{x}_i and \bar{y}_i are the corresponding points on the ground truth contour which has the closet distance to the points x_i and y_i . Lower RMSE values mean that the contour is closer to the ground truth, and thus a segmentation result is more accurate.

Firstly, synthesized images are used to evaluate the performance of the proposed algorithm. A synthesized image (Figure 4.3 a) is generated and Gaussian noise with different variances (listed in Table 4.1) is added to this image to produce the test images. The size of the synthesized image is 128*64 pixels. Figure 4.3 b), Figure 4.3 c), and Figure 4.3.e) show the synthesized images with Gaussian variance $\nu=0.02, 0.4, 1.0$, respectively. The segmentation results of these images are shown in Figure 4.3 b), Figure 4.3 d) and Figure 4.3 f), respectively. The Dice and RMSE results of proposed algorithm are shown in Table 4.1.

Table 4.1 Dice and RMSE values of the proposed algorithm

Variations of Gaussian Noise	Dice	RMSE
0.02	0.9993	0.0191
0.2	0.9783	0.1025
0.3	0.9730	0.1148
0.4	0.9572	0.1428
0.8	0.9444	0.1639
1.0	0.9202	0.1920

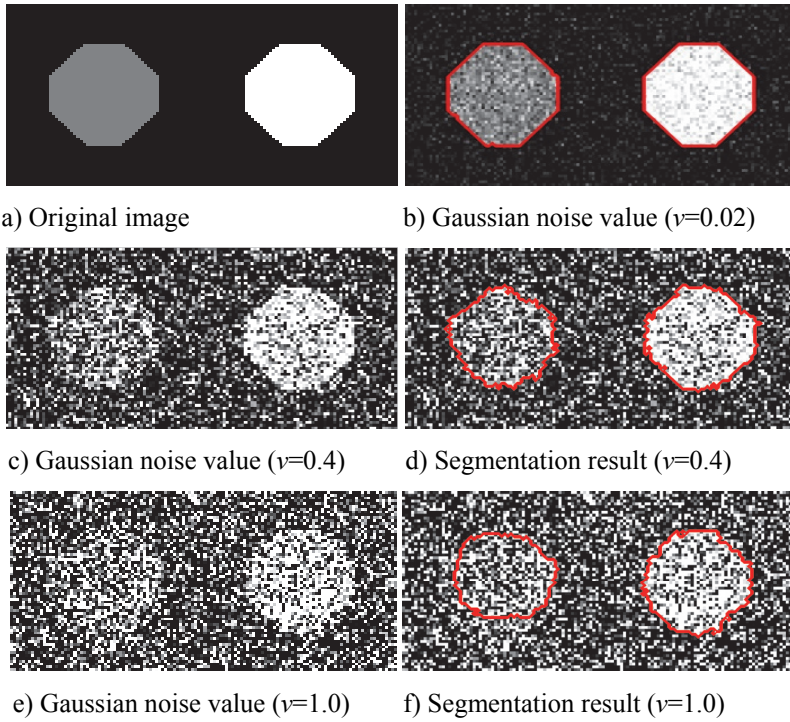
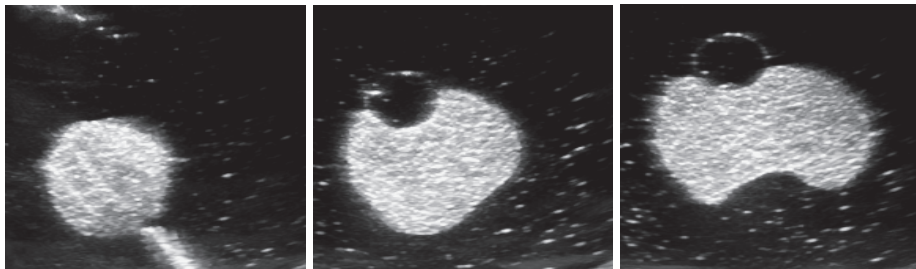


Figure 4.3 Segmentation results of synthesized images

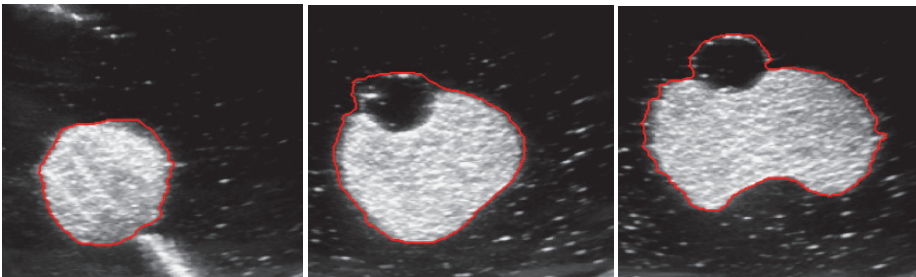
A series of kidney phantom images consisting of a sequence of 110 ultrasound images are used to test the proposed algorithm. The image size is 191*211 pixels. Out of the series, 3 images are shown here together with the results in Figure 4.4. Figure 4.4 a) is the phantom ultrasound image; the second row represents the results of the proposed algorithm; the third row shows the results of the RSF algorithm. The kidney phantom's border is difficult to detect and has a discontinuous edge in Figure 4.4. However, the proposed algorithm is able to extract the edge of the kidney correctly while RSF algorithm fails to accurately segment the kidney's edge. The average Dice and the RMSE results of the proposed algorithm are shown in Table 4.2.

Table 4.2 Dice and RMSE value of phantom images

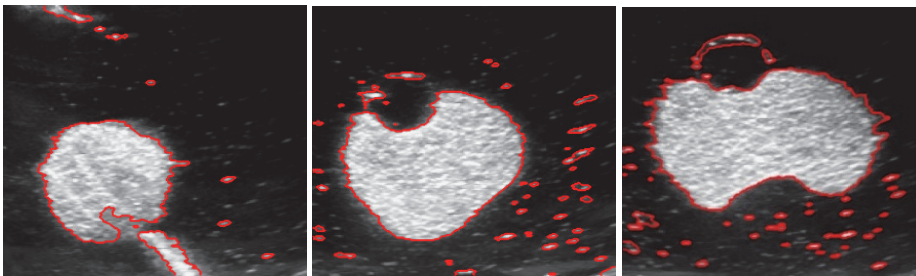
	Phantom images
Dice	0.9595
RMSE	0.1425



a) Original image



b) Proposed algorithm



c) RSF algorithm

Figure 4.4 Segmentation results of phantom images

Figure 4.5 shows the segmentation results of the proposed algorithm on two human kidney ultrasound images obtained from East Tallinn Central Hospital, Estonia. Compared to the phantom kidney images, in a human kidney ultrasound image, the kidney is surrounded by human tissue, therefore the differences in intensities between the interior kidney and exterior kidney are small and the segmentation of the kidney becomes more difficult. From the segmentation results of the human kidney ultrasound images, we can see that the proposed algorithm is able to segment the kidney ultrasound images with satisfactory results.

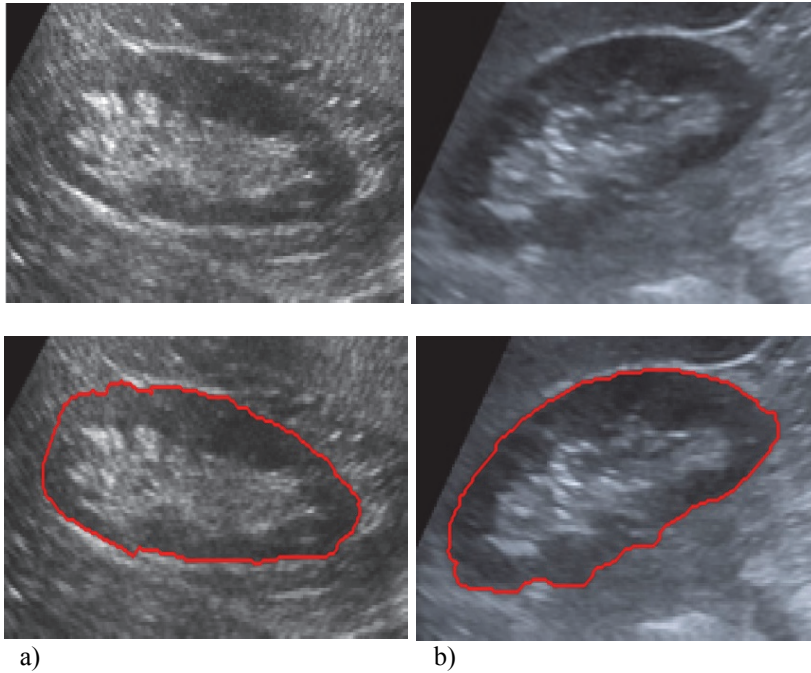


Figure 4.5 Segmentation results of patient kidney ultrasound images

Three types of images are used to evaluation the performance of the proposed algorithm: one synthesized ultrasound image (Figure 2.7 b), one ultrasound image of a phantom (the first image in Figure 4.4), and one ultrasound image of a patient (Figure 4.5 a). Table 4.3 shows the running times, the iteration counts and the Dice values of the proposed algorithm and the RSF algorithm.

Table 4.3 Performance of the proposed algorithm and the RSF algorithm

Image types	The proposed algorithm			RSF algorithm		
	Time(s)	Iterations	Dice	Time(s)	Iterations	Dice
Synthetic image (128*64 pixels)	1.458	100	0.9857	2.580	100	0.9804
Phantom image (191*211 pixels)	13.493	400	0.9476	12.1472	400	0.7583
Patient image (177*189 pixels)	34.357	800	0.8739	Not converge		

4.6 Conclusions

In this section, the drawbacks of RSF algorithm on segmenting very inhomogeneous images are discussed, and a solution for segmenting such images is proposed. An algorithm which combines the localized factor with the RSF algorithm is proposed. To increase the segmentation precision, the Bhattacharyya distance is also included into the algorithm. Different types of synthetic images are used to test the performance of the algorithm. The results show that the proposed algorithm can segment inhomogeneous images and produce satisfactory results. The performance of the proposed algorithm is also evaluated on kidney phantom ultrasound images and patient kidney ultrasound images. The results show that the proposed algorithm is able to deal with inhomogeneous images and has desirable segmentation results on images with weak boundaries.

5 Conclusions

This thesis addresses the segmentation problem of ultrasound images. Ultrasound image is commonly used in clinical applications. However, the speckle phenomenon in the ultrasound imaging affects the ultrasound image quality. Due to the speckle noise in the ultrasound images, the segmentation is a difficult task. Traditional algorithms which are designed for natural scenes have difficulty to produce desirable segmentation results. To improve the ultrasound image segmentation results, the statistical properties of ultrasound images are investigated in this PhD research. In this thesis, three novel algorithms for ultrasound image segmentation are proposed by using the statistical properties of the ultrasound images during the segmentation process.

An algorithm which combined the Chan & Vese algorithm and the Bhattacharyya distance was proposed in section 2. Phantom images with added noise and a real patient kidney ultrasound image were used to test the performance of the algorithm. The segmentation results showed that the proposed algorithm was able to deal with inhomogeneous ultrasound images. Compared to the Chan & Vese algorithm, the proposed algorithm was more robust and provided better segmentation results.

In section 3, a localized region based active contour framework was used. Two algorithms using the localized region based active contour are proposed: the localized Rayleigh active contour algorithm and the localized shifted Rayleigh active contour algorithm. The performances of these two algorithms were analysed. Synthetic images, phantom ultrasound images and patient ultrasound image were used as the evaluation images. The results showed that the proposed algorithms were capable of segmenting ultrasound images and could produce desirable segmentation results on ultrasound images with blurry edges. The comparison of the localized Rayleigh active contour algorithm and the localized shifted Rayleigh active contour algorithm showed that the localized shifted Rayleigh active contour algorithm had better segmentation performance than the localized Rayleigh active contour algorithm.

In section 4, a localized active contour algorithm was proposed which combined the region scalable fitting algorithm and the localized region based algorithm. The segmentation results of the proposed algorithm were evaluated on synthetic images, phantom ultrasound images and patient ultrasound images. The results showed that the proposed algorithms could produce satisfactory segmentation results on ultrasound images with weak boundaries. The performance of the proposed algorithm was compared with region scalable fitting algorithm. Compared to the region scalable fitting algorithm, the proposed algorithm is more robust. The evaluation and comparison results showed that the proposed algorithm had better performance than the region scalable fitting algorithm.

By considering the statistical properties of ultrasound images, three novel segmentation algorithms are proposed in this thesis. Various ultrasound images

are used to evaluate the performance of the proposed algorithms. The evaluation results show that the proposed algorithms can improve the ultrasound image segmentation results.

References

- [1] K. R. Erikson, F. J. Fry, and J. P. Jones, "Ultrasound in Medicine-A Review," *IEEE Trans. Sonics Ultrason.*, vol. 21, no. 3, pp. 144–170, 1974.
- [2] P. N. T. Wells, "Doppler ultrasound in medical diagnosis," *Br. J. Radiol.*, vol. 62, no. 737, pp. 399–420, 1989.
- [3] C. C. Mottin, M. Moretto, A. V Padoin, A. M. Swarowsky, M. G. Toneto, L. Glock, and G. Repetto, "The role of ultrasound in the diagnosis of hepatic steatosis in morbidly obese patients.," *Obes. Surg.*, vol. 14, pp. 635–637, 2004.
- [4] P. Burns, "Introduction to The Physical Principles Of Ultrasound Imaging And Doppler," *Fundam. Med. Biophys. retrieved*, pp. 1–26, 2005.
- [5] J. A. Jensen, O. Holm, L. J. Jensen, H. Bendsen, S. I. Nikolov, B. G. Tomov, P. Munk, M. Hansen, K. Salomonsen, J. Hansen, K. Gormsen, H. M. Pedersen, and K. L. Gammelmark, "Ultrasound research scanner for real-time synthetic aperture data acquisition," *IEEE Trans. Ultrason. Ferroelectr. Freq. Control*, vol. 52, no. 5, pp. 881–891, 2005.
- [6] R. T. O'Brien and S. P. Holmes, "Recent Advances in Ultrasound Technology," *Clin. Tech. Small Anim. Pract.*, vol. 22, pp. 93–103, 2007.
- [7] C. J. Harvey, J. M. Pilcher, R. J. Eckersley, M. J. K. Blomley, and D. O. Cosgrove, "Advances in Ultrasound," *Clin. Radiol.*, vol. 57, no. 3, pp. 157–177, 2002.
- [8] J. a Noble and D. Boukerroui, "Ultrasound image segmentation: A survey," *IEEE Trans. Med. Imaging*, vol. 25, no. 8, pp. 987–1010, 2006.
- [9] P. J. J. Benkeser, a. L. L. Churchwell, C. K. Lee, and D. M. M. Abouelnasr, "Resolution limitations in intravascular ultrasound imaging," *J. Am. Soc. Echocardiogr.*, vol. 6, no. 2, pp. 158–65, 1991.
- [10] E. L. Rosen and M. S. Soo, "Tissue harmonic imaging sonography of breast lesions," *Clin. Imaging*, vol. 25, no. 6, pp. 379–384, 2001.

- [11] T. S. Desser and R. B. Jeffrey, "Tissue harmonic imaging techniques: physical principles and clinical applications.," *Semin. Ultrasound. CT. MR*, vol. 22, no. 1, pp. 1–10, 2001.
- [12] J. S. Huber, W. W. Moses, and I. C. Hsu, "Dual-Modality PET/Ultrasound Imaging of the Prostate," *Nucl. Sci. Symp. Conf. Rec. IEEE*, 2005.
- [13] D. a. Guenther and W. F. Walker, "Optimal apodization design for medical ultrasound using constrained least squares part I: theory," *IEEE Trans. Ultrason. Ferroelectr. Freq. Control*, vol. 54, no. 2, pp. 343–358, 2007.
- [14] D. a. Guenther and W. F. Walker, "Optimal apodization design for medical ultrasound using constrained least squares Part II: Simulation results," *IEEE Trans. Ultrason. Ferroelectr. Freq. Control*, vol. 54, no. 2, pp. 343–358, 2007.
- [15] J. U. Quistgaard, *Signal acquisition and processing in medical diagnostic ultrasound*, vol. 14, no. 1. 1997.
- [16] J. S. Duncan and N. Ayache, "Medical image analysis: progress over two decades and the challenges ahead," *IEEE Trans. Pattern Anal. Mach. Intell.*, vol. 22, no. 1, pp. 85–106, 2000.
- [17] J. A. Noble, N. Navab, and H. Becher, "Ultrasonic image analysis and image-guided interventions," *Interface Focus*, 2011.
- [18] T. Walter, J.-C. Klein, P. Massin, and A. Erginay, "A contribution of image processing to the diagnosis of diabetic retinopathy--detection of exudates in color fundus images of the human retina.," *IEEE Trans. Med. Imaging*, vol. 21, no. 10, pp. 1236–1243, 2002.
- [19] F. Han and S. Zhu, "Bayesian reconstruction of 3D shapes and scenes from a single image," *FHigher-Level Knowl. 3D Model. Motion Anal. 2003. HLK 2003. First IEEE Int. Work. on. IEEE*, pp. 12–20, 2003.
- [20] S. H. Contreras Ortiz, T. Chiu, and M. D. Fox, "Ultrasound image enhancement: A review," *Biomed. Signal Process. Control*, vol. 7, no. 5, pp. 419–428, 2012.
- [21] J. A. Noble and D. Boukerroui, "Ultrasound image segmentation: a survey.," *IEEE Trans. Med. Imaging*, vol. 25, no. 8, pp. 987–1010, Aug. 2006.

- [22] K. Saini, M. L. Dewal, and M. Rohit, "Ultrasound imaging and image segmentation in the area of ultrasound: a review," *Int. J. Adv. Sci. Technol.*, vol. 24, pp. 41–60, 2010.
- [23] B. Solaiman, R. Debon, F. Pipelier, J.-M. Cauvin, and C. Roux, "Information fusion: application to data and model fusion for ultrasound image segmentation," *IEEE Trans. Biomed. Eng.*, vol. 46, no. 10, pp. 1171–1175, 1999.
- [24] Z. Chang ming, G. Guo chang, L. Hai bo, S. Jing, and Y. Hualong, "Segmentation of Ultrasound Image Based on Texture Feature and Graph Cut," *2008 Int. Conf. Comput. Sci. Softw. Eng.*, pp. 795–798, 2008.
- [25] J. Blackall, D. Rueckert, M. C.R., G. P. Penney, H. D.L.G., and D. J. Hawkes, "An image registration approach to automated calibration for freehand 3D ultrasound," *Med. Image Comput. Comput. Interv.*, pp. 462–471, 2000.
- [26] S. Standring, *Gray's Anatomy: The Anatomical Basis of Clinical Practice*. 2015.
- [27] A. Go, G. Chertow, D. Fan, C. E. Mcculloch, and C. Hsu, "Chronic Kidney Disease and the Risks of Death, Cardiovascular Events, and Hospitalization," *New Eng J Med*, vol. 351, no. 13, pp. 1296–1305, 2004.
- [28] J. Ferlay, P. Autier, M. Boniol, M. Heanue, M. Colombet, and P. Boyle, "Estimates of the cancer incidence and mortality in Europe in 2006," *Ann. Oncol.*, vol. 18, no. 3, pp. 581–592, 2006.
- [29] J. Coresh, B. C. Astor, T. Greene, G. Eknoyan, and A. S. Levey, "Prevalence of chronic kidney disease and decreased kidney function in the adult US population: Third national health and nutrition examination survey," *Am. J. Kidney Dis.*, vol. 41, no. 1, pp. 1–12, 2003.
- [30] Y. J. Chiang, S. H. Chu, K. L. Liu, W. J. Lai, H. H. Wang, H. W. Chen, T. M. Wang, J. Y. Huang, P. C. Lai, and Y. C. Tian, "Kidney Ultrasound Is Useful Tool in Posttransplant Follow-Up," *Transplant. Proc.*, vol. 38, no. 7, pp. 2018–2019, 2006.
- [31] S. Mustonen, I. O. Ala-Houhala, P. Vehkalahti, P. Laippala, and T. L. Tammela, "Kidney ultrasound and Doppler ultrasound findings during and after acute urinary retention.," *Eur. J. Ultrasound*, vol. 12, no. 3, pp. 189–96, 2001.

- [32] G. Ascenti, S. Mazziotti, G. Zimbaro, N. Settineri, C. Magno, D. Melloni, R. Caruso, and E. Scribano, “Complex cystic renal masses: characterization with contrast-enhanced US.,” *Radiology*, vol. 243, no. 1, pp. 158–65, 2007.
- [33] E. Quaia, M. Bertolotto, V. Cioffi, A. Rossi, E. Baratella, R. Pizzolato, and M. A. Cova, “Comparison of Contrast-Enhanced Sonography with Unenhanced Sonography and Contrast-Enhanced CT in the Diagnosis of Malignancy in Complex Cystic Renal Masses,” *Am. J. Roentgenol.*, vol. 191, no. 4, pp. 1239–1249, 2008.
- [34] D. K. Boal and R. L. Teele, “Sonography of infantile polycystic kidney disease.,” *AJR. Am. J. Roentgenol.*, vol. 135, no. 3, pp. 575–580, 1980.
- [35] R. Albayrak, B. Degirmenci, M. Acar, A. Haktanir, M. Colbay, and M. Yaman, “Accuracy of Sonography for Detecting Renal Stone: Comparison with CT,” *J. Clin. Ultrasound*, vol. 35, no. 1, pp. 27–33, 2007.
- [36] W. Wein, S. Brunke, A. Khamene, M. R. Callstrom, and N. Navab, “Automatic CT-ultrasound registration for diagnostic imaging and image-guided intervention,” *Med. Image Anal.*, vol. 12, no. 5, pp. 577–585, 2008.
- [37] J. Xie, Y. Jiang, and H. Tsui, “Segmentation of kidney from ultrasound images based on texture and shape priors.,” *IEEE Trans. Med. Imaging*, vol. 24, no. 1, pp. 45–57, Jan. 2005.
- [38] M. Martín-Fernández and C. Alberola-López, “An approach for contour detection of human kidneys from ultrasound images using Markov random fields and active contours.,” *Med. Image Anal.*, vol. 9, no. 1, pp. 1–23, Feb. 2005.
- [39] A. Fenster and D. B. Downey, “3-D ultrasound imaging: a review,” *IEEE Eng. Med. Biol. Mag.*, vol. 15, pp. 41–51, 1996.
- [40] J. a. Jensen, O. Holm, L. J. Jensen, H. Bendsen, H. M. Pedersen, K. Salomonsen, J. Hansen, and S. Nikolov, “Experimental ultrasound system for real-time synthetic imaging,” *IEEE Ultrason. Symp. Proceedings. Int. Symp.*, vol. 2, no. 1, pp. 1595–1599, 1999.
- [41] G. R. Lockwood, J. R. Talman, and S. S. Brunke, “Real-time 3-D ultrasound imaging using sparse synthetic aperture beamforming.,” *IEEE Trans. Ultrason. Ferroelectr. Freq. Control*, vol. 45, no. 4, pp. 980–988, 1998.

- [42] R. Lencioni, D. Cioni, and C. Bartolozzi, "Tissue harmonic and contrast-specific imaging: back to gray scale in ultrasound," *Eur. Radiol.*, vol. 12, no. 1, pp. 151–165, 2002.
- [43] M. Barva and J. Kybic, "Radial Radon transform dedicated to micro-object localization from radio frequency ultrasound signal," *IEEE Ultrason. Symp.*, vol. 3, no. 2, pp. 1836–1839, 2004.
- [44] <http://www.hitachi-aloka.com/products>. .
- [45] R. N. Bracewell, *The Fourier Transform and its Applications*. New York, 1965.
- [46] J. Kirkhorn, "Introduction to IQ-demodulation of RF-data," *Ifft, Ntnu*, pp. 1–13, 1999.
- [47] U. R. Abeyratne, A. P. Petropulu, J. M. Reid, and L. Fellow, "Higher Order Spectra Based Deconvolution of Ultrasound Images," *Ieee Trans. Ultrason. Ferroelectr. Freq. Control*, vol. 42, no. 6, pp. 1064–1075, 1995.
- [48] P. Suetens, *Fundamentals of Medical Imaging*. Cambridge university press, 2009.
- [49] M. Ali, D. Magee, and U. Dasgupta, "Signal processing overview of ultrasound systems for medical imaging," *SPRAB12, Texas*, no. November, pp. 1–27, 2008.
- [50] C. B. Burckhardt, "Speckle in ultrasound B-mode scans," *IEEE Trans. Sonics Ultrason.*, vol. 25, no. 1, pp. 1–6, 1978.
- [51] E. Brusseau, C. L. de Korte, F. Mastik, J. Schaar, and A. F. W. van der Steen, "Fully automatic luminal contour segmentation in intracoronary ultrasound imaging--a statistical approach.," *IEEE Trans. Med. Imaging*, vol. 23, no. 5, pp. 554–66, May 2004.
- [52] L. H. Prager, R. W., Gee, A. H., Treece, G. M., Berman, "Decompression and speckle detection for ultrasound images using the homodyned k-distribution," *Pattern Recognit. Lett.*, vol. 24, no. 4–5, pp. 705–713, 2003.
- [53] R. F. Wagner, S. W. Smith, J. M. Sandrik, and H. Lopez, "Statistics of Speckle in Ultrasound B-Scans," *IEEE Trans. Sonics Ultrason.*, vol. 30, no. 3, pp. 156–163, 1983.

- [54] M. Karaman, M. A. Kutay, and G. Bozdagi, "Adaptive speckle suppression filter for medical ultrasonic imaging," *IEEE Trans. Med. Imaging*, vol. 14, no. 2, pp. 283–292, 1995.
- [55] R. Sivaramakrishna, K. a Powell, M. L. Lieber, W. a Chilcote, and R. Shekhar, "Texture analysis of lesions in breast ultrasound images," *Comput. Med. Imaging Graph.*, vol. 26, pp. 303–307, 2002.
- [56] O. V. Michailovich and A. Tannenbaum, "Despeckling of medical ultrasound images," *IEEE Trans. Ultrason. Ferroelectr. Freq. Control*, vol. 53, no. 1, pp. 64–78, 2006.
- [57] G. V. S. R. M. Rekha, CH. Kranthi, K, "Speckle Noise Reduction in 3D Ultrasound Images – A Review," *Signal Process. Commun. Eng. Syst.*, pp. 257–259, 2015.
- [58] Q. Sun, J. a Hossack, J. Tang, and S. T. Acton, "Speckle reducing anisotropic diffusion for 3D ultrasound images.," *Comput. Med. Imaging Graph.*, vol. 28, no. 8, pp. 461–70, Dec. 2004.
- [59] R. S. Sudha, S., G. R. Suresh, "Speckle noise reduction in ultrasound images using context-based adaptive wavelet," *IETE J. Res.*, vol. 55, no. 3, pp. 135–142, 2009.
- [60] R. N. Czerwinski, D. L. Jones, and W. D. . J. O'Brien, "Ultrasound speckle reduction by directional median filtering," *Proceedings., Int. Conf. Image Process.*, vol. 1, pp. 358–361, 1995.
- [61] J. Kim, J. W. Fisher, a J. Yezzi, M. Cetin, and a S. Willsky, "Nonparametric methods for image segmentation using information theory and curve evolution," *Proc. Int. Conf. Image Process.*, pp. 797–800, 2002.
- [62] J. Kimt, K. F. Iip, M. Cetint, A. Yezzi, and S. Nskyt, "Incorporating complex statistical information in active contour-based image segmentation," *Image Process. 2003. ICIP 2003. Proceedings. 2003 Int. Conf.*, vol. 2, pp. 2–5, 2003.
- [63] X. Hao, S. Gao, and X. Gao, "A novel multiscale nonlinear thresholding method for ultrasonic speckle suppressing.," *IEEE Trans. Med. Imaging*, vol. 18, no. 9, pp. 787–94, 1999.
- [64] A. Achim, A. Bezerianos, and P. Tsakalides, "Novel Bayesian multiscale method for speckle removal in medical ultrasound

- images,” *IEEE Trans. Med. Imaging*, vol. 20, no. 8, pp. 772–783, 2001.
- [65] D. Shen, Y. Zhan, and C. Davatzikos, “Segmentation of Prostate Boundaries From Ultrasound Images Using Statistical Shape Model,” *Med. Imaging, IEEE Trans.*, vol. 22, no. 4, pp. 539–551, 2003.
- [66] M. G. Strintzis, S. Member, and I. Kokkinidis, “Maximum likelihood motion estimation in ultrasound image sequences,” *IEEE Signal Process. Lett.*, vol. 4, no. 6, pp. 156–157, 1997.
- [67] P. Mohana Shankar, “A general statistical model for ultrasonic backscattering from tissues,” *IEEE Trans. Ultrason. Ferroelectr. Freq. Control*, vol. 47, no. 3, pp. 727–736, 2000.
- [68] Q. M. Kaplan, David, “On the statistical characteristics of log \square compressed Rayleigh signals,” *Ultrason. Symp.*, no. 1978, pp. 961–964, 1993.
- [69] A. Sarti, C. Corsi, E. Mazzini, and C. Lamberti, “Maximum likelihood segmentation of ultrasound images with Rayleigh distribution,” *IEEE Trans. Ultrason. Ferroelectr. Freq. Control*, vol. 52, no. 6, pp. 947–60, Jun. 2005.
- [70] D. Sijbers, J., den Dekker, A. J., Scheunders, P., Van Dyck, “Maximum-likelihood estimation of Rician distribution parameters,” *IEEE Trans. Med. Imaging*, vol. 17, no. 3, pp. 357–361, 1998.
- [71] M. Insana and R. Wagner, “Analysis of ultrasound image texture via generalized Rician statistics,” *Opt. Eng.*, vol. 25, no. 6, pp. 256743–256743, 1986.
- [72] C. J. Bruce, C. Pislaru, and J. F. Greenleaf, “Characterization of reperfused infarcted myocardium from high-frequency intracardiac ultrasound imaging using homodyned K distribution,” *IEEE Trans. Ultrason. Ferroelectr. Freq. Control*, vol. 49, no. 11, pp. 1530–1542, 2002.
- [73] R. Krupiński and J. Purczyński, “Approximated fast estimator for the shape parameter of generalized Gaussian distribution,” *Signal Processing*, vol. 86, no. 2, pp. 205–211, 2006.
- [74] O. Bernard, J. D’hooge, and D. Friboulet, “Statistical Modeling of the Radio-Frequency Signal in Echocardiographic Images Based

- on Generalized Gaussian Distribution,” *Biomed. Imaging Nano to Macro, 2006. 3rd IEEE Int. Symp.*, vol. 5, 2006.
- [75] P. M. Shankar, V. a Dumane, J. M. Reid, V. Genis, F. Forsberg, C. W. Piccoli, and B. B. Goldberg, “Classification of ultrasonic B-mode images of breast masses using Nakagami distribution.” *IEEE Trans. Ultrason. Ferroelectr. Freq. Control*, vol. 48, no. 2, pp. 569–580, 2001.
- [76] P. M. Shankar, “Ultrasonic tissue characterization using a generalized Nakagami model.” *IEEE Trans. Ultrason. Ferroelectr. Freq. Control*, vol. 48, no. 6, pp. 1716–1720, 2001.
- [77] O. Bernard, B. Touil, J. D. and D. Friboulet, “Statistical modeling of the radio-frequency signal for partially-and fully-developed speckle based on a generalized gaussian model with application to echocardiography,” *Ultrason. Ferroelectr. Freq. Control. IEEE Trans.*, vol. 54, no. 10, pp. 2189–2194, 2007.
- [78] A. Richard and I. Walker, “Mixture densities, maximum likelihood and the EM algorithm,” *SIAM Rev.*, vol. 26, no. 2, pp. 195–239, 1984.
- [79] S. G. Mallat, “A Theory for Multiresolution Signal Decomposition: The Wavelet Representation,” *Pattern Anal. Mach. Intell. IEEE Trans.*, vol. 11, no. 7, pp. 674–693, 1989.
- [80] G. Slabaugh, G. Unal, M. Wels, T. Fang, and B. Rao, “Statistical region-based segmentation of ultrasound images.” *Ultrasound Med. Biol.*, vol. 35, no. 5, pp. 781–795, May 2009.
- [81] M. A. Kutay, A. P. Petropulu, and C. W. Piccoli, “Breast tissue characterization based on modeling of ultrasonic echoes using the power-law shot noise model,” *Pattern Recognit. Lett.*, vol. 24, no. 4–5, pp. 741–756, 2003.
- [82] R. F. Chang, W. J. Wu, W. K. Moon, and D. R. Chen, “Automatic ultrasound segmentation and morphology based diagnosis of solid breast tumors.” *Breast Cancer Res. Treat.*, vol. 89, no. 2, pp. 179–185, 2005.
- [83] Thomas., T. Fischer, H. Frey, R. Ohlinger, S. Grunwald, J.-U. Blohmer, K.-J. Winzer, S. Weber, G. Kristiansen, B. Ebert, and S. Kümmel, “Real-time elastography — an advanced method of ultrasound: first results in 108 patients with breast lesions,” *Ultrasound Obstet. Gynecol.*, vol. 28, no. 3, pp. 335–340, 2006.

- [84] L. Gong, L. Ng, S. D. Pathak, I. Tutar, P. S. Cho, D. R. Haynor, and Y. Kim, "Prostate ultrasound image segmentation using level set-based region flow with shape guidance," *Med. Imaging. Int. Soc. Opt. Photonics*, no. 206, pp. 1648–1657, 2005.
- [85] S. D. Pathak, V. Chalana, D. R. Haynor, and Y. Kim, "Edge-guided boundary delineation in prostate ultrasound images," *IEEE Trans. Med. Imaging*, vol. 19, no. 12, pp. 1211–1219, 2000.
- [86] G. Houston, S. B. Premkumar, D. E. Pitts, and R. J. Babaian, "Prostate ultrasound image analysis: localization of cancer lesions to assist biopsy," *Proc. Eighth IEEE Symp. Comput. Med. Syst.*, pp. 94–101.
- [87] G. D. Dodd 3rd, W. J. Miller, R. L. Baron, M. L. Skolnick, and W. L. Campbell, "Detection of malignant tumors in end-stage cirrhotic livers: efficacy of sonography as a screening technique," *AJR Am J Roentgenol*, vol. 159, no. 4, pp. 727–733, 1992.
- [88] S. Tanaka, T. Kitamura, M. Fujita, and K. Nakanishi, "Color Doppler flow imaging of liver tumors," *Am. J. Roentgenol.*, vol. 154, no. 3, pp. 509–514, 1990.
- [89] J. Hohmann, T. Albrecht, a. Oldenburg, J. Skrok, and K.-J. Wolf, "Liver metastases in cancer: detection with contrast-enhanced ultrasonography," *Abdom. Imaging*, vol. 29, no. 6, pp. 669–681, 2004.
- [90] G. Pilu and M. Segata, "A novel technique for visualization of the normal and cleft fetal secondary palate: angled insonation and three-dimensional ultrasound," *Ultrasound Obstet. Gynecol.*, vol. 29, no. 2, pp. 166–169, 2007.
- [91] L. F. Gonçalves, W. Lee, J. Espinoza, and R. Romero, "Examination of the fetal heart by four-dimensional (4D) ultrasound with spatio-temporal image correlation (STIC)," *Ultrasound Obstet. Gynecol.*, vol. 27, no. 3, pp. 336–348, 2006.
- [92] H. H. Radermacher, Jörg, Ajay Chavan, Jörg Bleck, Annabel Vitzthum, Birte Stoess, Michael Jan Gebel, Michael Galanski, Karl Martin Koch, "Use of Doppler ultrasonography to predict the outcome of therapy for renal-artery stenosis," *N. Engl. J. Med.*, vol. 344, no. 6, pp. 410–417, 2001.
- [93] H. Tamai, Y. Takiguchi, M. Oka, N. Shingaki, S. Enomoto, T. Shiraki, M. Furuta, I. Inoue, M. Iguchi, K. Yanaoka, K. Arii, Y.

- Shimizu, H. Nakata, T. Shinka, T. Sanke, and M. Ichinose, "Contrast-enhanced ultrasonography in the diagnosis of solid renal tumors.," *J. Ultrasound Med.*, vol. 24, no. 12, pp. 1635–1640, 2005.
- [94] R. O. Illing, J. E. Kennedy, F. Wu, G. R. ter Haar, a S. Protheroe, P. J. Friend, F. V Gleeson, D. W. Cranston, R. R. Phillips, and M. R. Middleton, "The safety and feasibility of extracorporeal high-intensity focused ultrasound (HIFU) for the treatment of liver and kidney tumours in a Western population.," *Br. J. Cancer*, vol. 93, no. 8, pp. 890–895, 2005.
- [95] T. Hoshi, Y. Kobayashi, and M. G. Fujie, "Developing a system to identify the material parameters of an organ model for surgical robot control," *Proc. 2nd Bienn. IEEE/RAS-EMBS Int. Conf. Biomed. Robot. Biomechatronics, BioRob 2008*, pp. 730–735, 2008.
- [96] E. C. Pua, M. P. Fronheiser, J. R. Noble, E. D. Light, P. D. Wolf, D. von Allmen, and S. W. Smith, "3-D ultrasound guidance of surgical robotics: a feasibility study.," *IEEE Trans. Ultrason. Ferroelectr. Freq. Control*, vol. 53, no. 11, pp. 1999–2008, 2006.
- [97] K. C. Zorn, O. N. Gofrit, M. a. Orvieto, A. a. Mikhail, G. P. Zagaja, and A. L. Shalhav, "Robotic-Assisted Laparoscopic Prostatectomy: Functional and Pathologic Outcomes with Interfascial Nerve Preservation," *Eur. Urol.*, vol. 51, no. 3, pp. 755–763, 2007.
- [98] V. Ficarra, S. Cavalleri, G. Novara, M. Aragona, and W. Artibani, "Evidence from Robot-Assisted Laparoscopic Radical Prostatectomy: A Systematic Review," *Eur. Urol.*, vol. 51, no. 1, pp. 45–56, 2007.
- [99] V. Hlavac, "Fundamentals of Image Processing," *Opt. Digit. Image Process. Fundam. Appl.*, pp. 71–96, 2011.
- [100] K. Diaz and B. Castaneda, "Semi-automated segmentation of the prostate gland boundary in ultrasound images using a machine learning approach," *Med. Imaging. Int. Soc. Opt. Photonics*, vol. 6914, p. 69144A–69144A, 2008.
- [101] J. G. Thomas, R. a Peters, and P. Jeanty, "Automatic segmentation of ultrasound images using morphological operators.," *IEEE Trans. Med. Imaging*, vol. 10, no. 2, pp. 180–186, 1991.

- [102] C. Bruce, C. Pislaru, and J. F. Greenleaf, "A novel region growing method for segmenting ultrasound images," *Ultrason. Symp. 2000 IEEE*, pp. 1717–1720, 2000.
- [103] S. Poonguzhali and G. Ravindran, "A complete automatic region growing method for segmentation of masses on ultrasound images," in *Biomedical and Pharmaceutical Engineering, 2006. ICBPE 2006. International Conference on*, 2006, pp. 88–92.
- [104] A. Thakur and R. S. Anand, "A local statistics based region growing segmentation method for ultrasound medical images," *Int. J. Medical, Heal. Pharm. Biomed. Eng.*, vol. 1, no. 10, pp. 565–570, 2007.
- [105] Y. Zhan and D. Shen, "Deformable segmentation of 3-D ultrasound prostate images using statistical texture matching method.," *IEEE Trans. Med. Imaging*, vol. 25, no. 3, pp. 256–272, Mar. 2006.
- [106] D. Boukerroui, A. Baskurt, J. A. Noble, and O. Basset, "Segmentation of ultrasound images-multiresolution 2D and 3D algorithm based on global and local statistics," *Pattern Recognit. Lett.*, vol. 24, no. 4–5, pp. 779–790, 2003.
- [107] G. Slabaugh, G. Unal, and M. Wels, "Ultrasound-Specific Segmentation via Decorrelation and Statistical Region-Based Active Contours," *2006 IEEE Comput. Soc. Conf. Comput. Vis. Pattern Recognit. - Vol. 1*, pp. 45–53.
- [108] M. Mart and C. Alberola, "A Bayesian Approach to in vivo Kidney Ultrasound Contour Detection Using Markov Random Fields," *Ultrasound*, pp. 397–404, 2002.
- [109] L. Cordero-Grande, G. Vegas-Sánchez-Ferrero, P. Casaseca-de-la-Higuera, J. Alberto San-Román-Calvar, A. Revilla-Orodea, M. Martín-Fernández, and C. Alberola-López, "Unsupervised 4D myocardium segmentation with a Markov Random Field based deformable model," *Med. Image Anal.*, vol. 15, no. 3, pp. 283–301, 2011.
- [110] A. Madabhushi and D. N. Metaxas, "Combining low-, high-level and empirical domain knowledge for automated segmentation of ultrasonic breast lesions.," *IEEE Trans. Med. Imaging*, vol. 22, no. 2, pp. 155–169, Feb. 2003.

- [111] G. D. Giannoglou, Y. S. Chatzizisis, V. Koutkias, I. Kompatsiaris, M. Papadogiorgaki, V. Mezaris, E. Parissi, P. Diamantopoulos, M. G. Strintzis, N. Maglaveras, G. E. Parcharidis, and G. E. Louridas, “A novel active contour model for fully automated segmentation of intravascular ultrasound images: In vivo validation in human coronary arteries,” *Comput. Biol. Med.*, vol. 37, no. 9, pp. 1292–1302, 2007.
- [112] M. Alemán-Flores, L. Álvarez, and V. Caselles, “Texture-Oriented Anisotropic Filtering and Geodesic Active Contours in Breast Tumor Ultrasound Segmentation,” *J. Math. Imaging Vis.*, vol. 28, no. 1, pp. 81–97, 2007.
- [113] G. Hamarneh and T. Gustavsson, “Combining snakes and active shape models for segmenting the human left ventricle in echocardiographic images,” *Comput. Cardiol. 2000*, pp. 115–118, 2000.
- [114] J. Meunier, G. Soulez, and G. Cloutier, “Intravascular Ultrasound Image Segmentation: A Fast-Marching Method,” *J. Opt. Nouv. Rev. D’Optique*, pp. 432–439.
- [115] X. Zhu, P. Zhang, J. Shao, Y. Cheng, Y. Zhang, and J. Bai, “A snake-based method for segmentation of intravascular ultrasound images and its in vivo validation,” *Ultrasonics*, vol. 51, no. 2, pp. 181–189, 2011.
- [116] A. K. Jumaat, W. E. Z. W. A. Rahman, A. Ibrahim, and R. Mahmud, “Segmentation of Masses from Breast Ultrasound Images using Parametric Active Contour Algorithm,” *Procedia - Soc. Behav. Sci.*, vol. 8, no. 5, pp. 640–647, 2010.
- [117] H. D. Cheng, J. Shan, W. Ju, Y. Guo, and L. Zhang, “Automated breast cancer detection and classification using ultrasound images: A survey,” *Pattern Recognit.*, vol. 43, no. 1, pp. 299–317, Jan. 2010.
- [118] I. Mikić, S. Krucinski, and J. D. Thomas, “Segmentation and tracking in echocardiographic sequences: active contours guided by optical flow estimates,” *IEEE Trans. Med. Imaging*, vol. 17, no. 2, pp. 274–284, Apr. 1998.
- [119] V. Chalana, D. T. Linker, D. R. Haynor, and Y. Kim, “A multiple active contour model for cardiac boundary detection on

- echocardiographic sequences.” *IEEE Trans. Med. Imaging*, vol. 15, no. 3, pp. 290–298, Jan. 1996.
- [120] R. Prevost, B. Mory, R. Cuingnet, J. Correas, L. D. Cohen, and R. Ardon, “Kidney Detection and Segmentation in Contrast-Enhanced Ultrasound 3D Images,” *Abdomen Thorac. Imaging*, pp. 37–67, 2014.
- [121] C. Xu and J. L. Prince, “Snakes, shapes, and gradient vector flow.”, *IEEE Trans. Image Process.*, vol. 7, no. 3, pp. 359–369, Jan. 1998.
- [122] Y. Chen, “Using Prior Shapes in Geometric Active Contours in a Variational Framework,” *Int. J. Comput. Vis.*, vol. 50, no. 3, pp. 315–328, 2002.
- [123] D. Peng, B. Merriman, S. Osher, H. Zhao, and M. Kang, “A PDE-Based Fast Local Level Set Method,” *J. Comput. Phys.*, vol. 155, pp. 410–438, 1999.
- [124] S. Osher, S. Osher, R. P. Fedkiw, and R. P. Fedkiw, “Level Set Methods: An Overview and Some Recent Results,” *J. Comput. Phys.*, vol. 169, no. 2, pp. 463–502, 2001.
- [125] C. Li, R. Huang, Z. Ding, C. Gatenby, D. Metaxas, and J. Gore, “A variational level set approach to segmentation and bias correction of images with intensity inhomogeneity.”, *Med. Image Comput. Comput. Interv. 2008*, pp. 1083–1091, 2008.
- [126] L. Vese and T. Chan, “A multiphase level-set framework for image segmentation using the Mumford and Shah model,” *Int. J. Comp. Vis.*, vol. 50(3), no. 3, pp. 271–279, 2002.
- [127] T. Chan and W. Zhu, “Level Set Based Shape Prior Segmentation,” *2005 IEEE Comput. Soc. Conf. Comput. Vis. Pattern Recognit.*, vol. 2, pp. 1164–1170.
- [128] S. Kichenassamy, a. Kumar, P. Olver, a. Tannenbaum, and a. Yezzi, “Gradient flows and geometric active contour models,” *Proc. IEEE Int. Conf. Comput. Vis.*, pp. 4–9, 1995.
- [129] R. Malladi, J. a. Sethian, and B. C. Vemuri, “Shape modeling with front propagation: a level set approach,” *IEEE Trans. Pattern Anal. Mach. Intell.*, vol. 17, no. 2, pp. 158–175, 1995.
- [130] R. Kimmel, A. Amir, and A. Bruckstein, “Finding shortest paths on surfaces using level sets propagation,” *IEEE Trans. Pattern Anal. Mach. Intell.*, vol. 17, no. 6, pp. 635–640, 1995.

- [131] X. Bresson, S. Esedoğlu, P. Vandergheynst, J.-P. Thiran, and S. Osher, “Fast Global Minimization of the Active Contour/Snake Model,” *J. Math. Imaging Vis.*, vol. 28, no. 2, pp. 151–167, Jul. 2007.
- [132] K. Zhang, L. Zhang, H. Song, and W. Zhou, “Active contours with selective local or global segmentation: A new formulation and level set method,” *Image Vis. Comput.*, vol. 28, no. 4, pp. 668–676, Apr. 2010.
- [133] C. Samson, L. Blanc-Féraud, G. Aubert, and J. Zerubia, “A variational model for image classification and restoration,” *IEEE Trans. Pattern Anal. Mach. Intell.*, vol. 22, no. 5, pp. 460–472, 2000.
- [134] M. Gastaud, M. Barlaud, and G. Aubert, “Combining Shape Prior and Statistical Features for Active Contour Segmentation,” *IEEE Trans. Circuits Syst. Video Technol.*, vol. 14, no. 5, pp. 726–734, May 2004.
- [135] D. Cremers, S. J. Osher, and S. Soatto, “Kernel Density Estimation and Intrinsic Alignment for Shape Priors in Level Set Segmentation,” *Int. J. Comput. Vis.*, vol. 69, no. 3, pp. 335–351, May 2006.
- [136] D. Cremers, M. Rousson, and R. Deriche, “A Review of Statistical Approaches to Level Set Segmentation: Integrating Color, Texture, Motion and Shape,” *Int. J. Comput. Vis.*, vol. 72, no. 2, pp. 195–215, Aug. 2006.
- [137] J. A. S. Osher, Stanley, “Fronts propagating with curvature-dependent speed algorithms based on Hamilton-Jacobi formulations.,” *J. Comput. Phys.*, pp. 12–49, 1988.
- [138] I. B. A. Mitiche, Amar, *Variational and level set methods in image segmentation*. Springer Science & Business Media, 2010.
- [139] D. T. Kass, Michael, Andrew Witkin, “Snakes: Active contour models,” *Int. J. Comput. Vis.*, vol. 4, pp. 321–331, 1988.
- [140] R. Goldenberg, R. Kimmel, E. Rivlin, and M. Rudzsky, “Geodesic active contours,” *IEEE Trans. Image Process.*, vol. 10, no. 10, pp. 1467–1475, Jan. 2001.

- [141] J. S. Mumford, David, "Optimal approximations by piecewise smooth functions and associated variational problems," *Commun. pure Appl. Math.*, pp. 577–685, 1989.
- [142] T. F. Chan and L. a Vese, "Active contours without edges.," *IEEE Trans. Image Process.*, vol. 10, no. 2, pp. 266–277, Jan. 2001.
- [143] Y. M. Kadah, A. a. Farag, J. M. Zurada, A. M. Badawi, and A. B. M. Youssef, "Classification algorithms for quantitative tissue characterization of diffuse liver disease from ultrasound images," *IEEE Trans. Med. Imaging*, vol. 15, no. 4, pp. 466–478, 1996.
- [144] B. B. Gosink, S. K. Lemon, W. Scheible, and G. R. Leopold, "Accuracy of ultrasonography in diagnosis of hepatocellular disease," *Am. J. Roentgenol.*, vol. 133, no. 1, pp. 19–23, 1979.
- [145] K. J. T. Kremkau, F. W., "Artifacts in ultrasound imaging," *J. ultrasound Med.*, pp. 227–237, 1986.
- [146] H. Zhu, "On information and sufficiency," *Ann. Math. Stat.*, pp. 79–86, 1951.
- [147] T. Chan, S. Esedoglu, and K. Ni, "Histogram Based Segmentation Using Wasserstein Distances," *Scale Sp. Var. Methods Comput. Vis.*, pp. 697–708, 2007.
- [148] I. Communicatiopi, T. Technology, and O. N. Vol, "The Diver , gence and Bhattacharyya Distance Measures in Signal Selection," *Commun. Technol.*, vol. 15, no. 1, pp. 52–60, 1967.
- [149] P. T. H. Truc, T.-S. Kim, S. Lee, and Y.-K. Lee, "Homogeneity- and density distance-driven active contours for medical image segmentation.," *Comput. Biol. Med.*, vol. 41, no. 5, pp. 292–301, May 2011.
- [150] D. Freedman and T. Zhang, "Active contours for tracking distributions.," *IEEE Trans. Image Process.*, vol. 13, no. 4, pp. 518–526, 2004.
- [151] A. T. Michailovich, Oleg, Yogesh Rathi, "Image segmentation using active contours driven by the Bhattacharyya gradient flow," *mage Process. IEEE Trans.*, vol. 16, no. 11, pp. 2787–2801, 2007.
- [152] M. Alessandrini, D. Friboulet, O. Basset, J. D'hooge, and O. Bernard, "Level-set segmentation of myocardium and epicardium in ultrasound images using localized Bhattacharyya distance," *2009 IEEE Int. Ultrason. Symp.*, pp. 2468–2471, Sep. 2009.

- [153] D. Adalsteinsson and J. a. Sethian, “A fast level set method for propagating interfaces,” *J. Comput. Phys.*, vol. 118, no. 2, pp. 269–277, 1995.
- [154] J. a Sethian, “Evolution, Implementation, and Application of Level Set and Fast Marching Methods for Advancing Fronts,” *J. Comput. Phys.*, vol. 169, pp. 503–555, 2001.
- [155] J. a Sethian, “A fast marching level set method for monotonically advancing fronts.,” *Proc. Natl. Acad. Sci. U. S. A.*, vol. 93, no. 4, pp. 1591–1595, 1996.
- [156] M. Sussman, P. Smereka, and S. Osher, “A Level Set Approach for Computing Solutions to Incompressible Two-Phase Flow,” *Journal of Computational Physics*, vol. 114, no. 1. pp. 146–159, 1994.
- [157] M. Sussman and E. Fatemi, “An Efficient, Interface-Preserving Level Set Redistancing Algorithm and Its Application to Interfacial Incompressible Fluid Flow,” *SIAM J. Sci. Comput.*, vol. 20, no. 4, pp. 1165–1191, 1999.
- [158] J. Sethian, “Level set methods and fast marching methods,” Cambridge university press, 1999.
- [159] G. Aubert, M. Barlaud, O. Faugeras, and S. Jehan-Besson, “Image Segmentation Using Active Contours: Calculus of Variations or Shape Gradients?,” *SIAM J. Appl. Math.*, vol. 63, no. 6, pp. 2128–2154, 2003.
- [160] L. R. Dice, “Measures of the amount of ecologic association between species,” *Ecology*, vol. 26, no. 3, pp. 297–302, 1945.
- [161] A. Hunt, A. Ristolainen, P. Ross, R. Öpik, A. Krumme, and M. Kruusmaa, “Low cost anatomically realistic renal biopsy phantoms for interventional radiology trainees,” *Eur. J. Radiol.*, vol. 82, no. 4, pp. 594–600, 2013.
- [162] S. Egmentation, D. L. Pham, C. Xu, and J. L. Prince, “Current methods in medical image segmentation,” *Annu. Rev. Biomed. Eng.*, vol. 2, no. 1, pp. 315–337, 2000.
- [163] S. C. Zhu, “Region competition: Unifying snakes, region growing, and bayes/mdl for multiband image segmentation,” *IEEE Trans. Pattern Anal. Mach. Intell.*, vol. 18, no. 9, pp. 884–900, 1996.
- [164] K. Sum and P. Cheung, “A novel active contour model using local and global statistics for vessel extraction,” *Med. Biol. Soc.*, 2006.

- [165] K. W. Sum and P. Y. S. Cheung, "Vessel extraction under non-uniform illumination: a level set approach.," *IEEE Trans. Biomed. Eng.*, vol. 55, no. 1, pp. 358–360, 2008.
- [166] S. Lankton and A. Tannenbaum, "Localizing region-based active contours," *IEEE Trans. Image Process.*, vol. 17, no. 11, pp. 2029–2039, Nov. 2008.
- [167] C. Baillard and C. Barillot, "Robust 3D Segmentation of Anatomical Structures," *Med. Image Comput. Comput. Interv. 2000*, pp. 236–245, 2000.
- [168] M. Mignotte and J. Meunier, "A multiscale optimization approach for the dynamic contour-based boundary detection issue," *Comput. Med. Imaging Graph.*, vol. 25, no. 3, pp. 265–275, 2001.
- [169] C. Li, C.-Y. Kao, J. C. Gore, and Z. Ding, "Minimization of region-scalable fitting energy for image segmentation.," *IEEE Trans. Image Process.*, vol. 17, no. 10, pp. 1940–1949, Oct. 2008.
- [170] M. D. Fox, "Level Set Evolution without Re-Initialization: A New Variational Formulation," *2005 IEEE Comput. Soc. Conf. Comput. Vis. Pattern Recognit.*, pp. 430–436, 2005.
- [171] K. Zhang, H. Song, and L. Zhang, "Active contours driven by local image fitting energy," *Pattern Recognit.*, vol. 43, no. 4, pp. 1199–1206, Apr. 2010.
- [172] Z. Wang, S. Member, and A. C. Bovik, "A Universal Image Quality Index," *Signal Process. Lett.*, vol. 9, no. 3, pp. 81–84, 2002.

Abstract

Ultrasound imaging is commonly used in clinical diagnosis. Ultrasound imaging has several advantages over other medical imaging techniques such as X-ray, computed tomography (CT) and magnetic resonance imaging (MRI). The ultrasound imaging system is cheap, portable and has short acquisition times. Also the ultrasound technique is safe for patients.

At the same time, ultrasound imaging has some limitations which reduce its applicability. The quality of ultrasound images is relatively poor with speckle noise and artifacts. The objects' edges in an ultrasound image are usually very blurry or missing at some places. Due to the noisy nature of ultrasound images, traditional segmentation algorithms have difficulty in producing desirable results. In this thesis, we focus on using statistical methods for ultrasound images segmentation, and propose three new algorithms.

The first algorithm combines the Chan & Vese algorithm and the Bhattacharyya distance. The Chan & Vese algorithm is a global algorithm, and it divides the image domain into two parts: internal and external regions. By using the Bhattacharyya distance, the proposed algorithm can maximize the difference between image regions and minimize the difference within the image regions. In the second algorithm, a localized region based active contour is used under the assumption that if the global requirement is not fulfilled in the image domain, then it can be satisfied in a small sub region with a high probability. Rayleigh distribution and shifted Rayleigh distribution are used to model the ultrasound image intensity distribution. The third algorithm combines a localized factor into the region scalable fitting algorithm and incorporates the Bhattacharyya distance in this algorithm.

To validate the performance of the proposed three algorithms, synthetic ultrasound images, phantom ultrasound images and patient ultrasound images are used as evaluation images. The segmentation results of the proposed algorithms show that the proposed algorithms are able to deal with ultrasound images with blurry edges and can produce desirable segmentation results. The segmentation results of the proposed algorithms are also compared with other algorithms to prove the efficiency of the proposed algorithms.

Kokkuvõte

Ultraheliuuringuid kasutatakse laialdaselt meditsiinilise diagnostika eesmärgil. Ultraheliuuringutel on mitmeid eeliseid võrreldes teiste meditsiinis kasutatavate uuringumeetoditega nagu röntgenülesvõtted, kompuutertomograafia (KT) ja magnetresonantstomograafia (MRT). Ultraheliuuringud on odavad, ultraheliseadmeid on lihtne transportida ja uuringud võtavad vähe aega. Ühtlasi on ultraheli patsiendile ohutu.

Samas on ultrahelitehnoloogial puudusi mis piiravad selle kasutatavust. Ultrahelipiltide kvaliteet on võrdlemisi kehv omades teralist tekstuuri ja artefakte. Objektide servad ultrahelipiltidel on harilikult väga hägused ja kohati puuduvad üldse. Ultrahelipiltide mürasuse tõttu on traditsioonilistel segmentatsioonialgoritmidel raskusi vajalike tulemuste saavutamisel. Käesolevas väitekirjas keskendutakse statistiliste meetodite kasutamisele ultraheli piltide segmenteerimiseks ja pakutakse välja kolm uut algoritmi.

Esimene algoritm kombineerib Chan&Vese algoritmi ja Bhattacharyya kauguse. Chan&Vese algoritm on globaalne algoritm, mis jagab pildidomeeni kaheks osaks: sisemine ja välimine piirkond. Loodud algoritm maksimeerib Bhattacharyya kaugust kasutades erinevust kahe pildiregiooni vahel ning minimeerib seda kummagi regiooni sees. Teises algoritmis kasutatakse lokaliseeritud regioonil põhinevat aktiivse kontuuri meetodit oletusel, et kui globaalne homogeensus ei ole pildidomeenil tagatud siis suure tõenäosusega on võimalik see täita väikses alamregioonis. Rayleigh jaotust ja nihutatud Rayleigh jaotust kasutatakse ultrahelipildi intensiivsuse jaotuse modelleerimiseks. Kolmas algoritm kombineerib lokaliseeritud regiooni faktoriseerimise ja regiooni skaleeriva lähendamise algoritmi ning kasutab Bhattacharyya kauguse meetodit.

Loodud kolme algoritmi toimimise hindamiseks kasutatakse tehislikke pilte ning fantoomidest ja inimestest tehtud ultrahelipilte. Teostatud segmenteerimise tulemustest on näha, et loodud algoritmid suudavad parandada ultrahelipiltide segmenteerimise tulemusi ja saavad hakkama ka ultrahelipiltidega millel struktuuride piirjooned on udused. Loodud algoritmidega teostatud segmenteerimise tulemusi võrreldakse ka teiste algoritmide omadega tõestamaks suuremat efektiivsust.

Appendix A

Muradore, R., Fiorini, P., Akgun, G., Barkana, D. E., Bonfe, M., Bonfe, F., Caprara, A., De Rossi, G., Dodi, R., Elle, O. J., Ferraguti, F., Gasperotti, L., Gassert, R., Mathiassen, K.; Handini, D., Lambercy, O., Li, L., Kruusmaa, M., Oberman Manurung, A., Meruzzi, G., Nguyen, H. Q. P., Preda, N., Riolfo, G., Ristolainen, A., Sanna, A., Secchi, C., Torsello, M., Yantac, A. E., "Development of a Cognitive Robotic System for Simple Surgical Tasks", *International Journal of Advanced Robotic Systems*, 2015, 12(37), pp.1 - 20.

Development of a Cognitive Robotic System for Simple Surgical Tasks

Invited Feature Article

Riccardo Muradore^{1*}, Paolo Fiorini¹, Gokhan Akgun², Duygun Erol Barkana³, Marcello Bonfe⁴, Fabrizio Boriero¹, Andrea Caprara¹¹, Giacomo De Rossi¹, Riccardo Dodi⁵, Ole Jakob Elle⁶, Federica Ferraguti⁷, Lorenza Gasperotti¹, Roger Gassert⁸, Kim Mathiassen⁶, Dilla Handini⁹, Olivier Lamercy⁸, Lin Li¹⁰, Maarja Kruusmaa¹⁰, Auralius Oberman Manurung⁸, Giovanni Meruzzi¹¹, Ho Quoc Phuong Nguyen⁹, Nicola Preda⁴, Gianluca Riolfo¹¹, Asko Ristolainen¹⁰, Alberto Sanna⁵, Cristian Secchi⁷, Marco Torsello¹¹ and Asim Evren Yantac¹²

1 Department of Computer Science, University of Verona, Italy

2 Cognitive Science Department, Yeditepe University, Istanbul, Turkey

3 Electrical and Electronics Engineering Department, Yeditepe University, Istanbul, Turkey

4 Engineering Department, University of Ferrara, Italy

5 e-Services for Life and Health Research Department, Fondazione Centro San Raffaele, Italy

6 Department of Informatics, University of Oslo, and The Intervention Center, Oslo University Hospital, Oslo, Norway

7 Department of Sciences and Methods for Engineering, University of Modena and Reggio Emilia, Italy

8 Rehabilitation Engineering Lab, Institute of Robotics and Intelligent Systems, Department of Health Sciences and Technology, ETH Zurich, Switzerland

9 The Intervention Center, Oslo University Hospital, Rikshospitalet, Norway

10 Tallinn University of Technology, Faculty of Information Technology, Centre for Biorobotics, Tallinn, Estonia

11 Department of Legal Studies, School of Law, University of Verona, Italy

12 Design Lab, Koc University, Istanbul, Turkey

* Corresponding author(s) E-mail: riccardo.muradore@univr.it

Received 29 September 2014; Accepted 29 January 2015

DOI: 10.5772/60137

© 2015 The Author(s). Licensee InTech. This is an open access article distributed under the terms of the Creative Commons Attribution License (<http://creativecommons.org/licenses/by/3.0>), which permits unrestricted use, distribution, and reproduction in any medium, provided the original work is properly cited.

Abstract

The introduction of robotic surgery within the operating rooms has significantly improved the quality of many surgical procedures. Recently, the research on medical robotic systems focused on increasing the level of autonomy in order to give them the possibility to carry out simple surgical actions autonomously. This paper reports on the development of technologies for introducing automation within the surgical workflow. The results have been obtained during the ongoing FP7 European funded project Intelligent Surgical Robotics (I-SUR). The main goal of the project is to demonstrate that autonomous robotic surgical

systems can carry out simple surgical tasks effectively and without major intervention by surgeons. To fulfil this goal, we have developed innovative solutions (both in terms of technologies and algorithms) for the following aspects: fabrication of soft organ models starting from CT images, surgical planning and execution of movement of robot arms in contact with a deformable environment, designing a surgical interface minimizing the cognitive load of the surgeon supervising the actions, intra-operative sensing and reasoning to detect normal transitions and unexpected events. All these technologies have been integrated using a component-based software architecture to control a novel

robot designed to perform the surgical actions under study. In this work we provide an overview of our system and report on preliminary results of the automatic execution of needle insertion for the cryoablation of kidney tumours.

Keywords Surgical robotics, Autonomous systems, High-performance robotics

1. Introduction

The introduction of minimally invasive surgery (MIS) first and, more recently, of surgical robots, has brought new perspectives to surgery and has significantly improved the quality of many surgical procedures (e.g., [1, 2, 3, 4, 5]). However, current surgical robots are not the final answer to surgeon's demands in terms of (1) high motion accuracy (to enable interventions that would otherwise be impossible), (2) dexterity, (3) presenting information in a more meaningful way (to improve the quality of the clinical result, e.g., virtual fixtures, active constraints) [6]. In fact, they are teleoperated devices without any embedded autonomy (e.g., the Da Vinci by Intuitive Surgical [7] and the MiroSurge developed by Deutschland für Luft- und Raumfahrt (DLR) [8] and therefore performance-bound by the perception and dexterity of their human operators.

Although it is well known that automation has been successfully used to enhance a great variety of human activities from aircraft control to manufacturing, the whole area of autonomous interaction of surgical tools with biological tissues is rather unexplored. In the applications where it has been used, automation has increased safety, accuracy, reproducibility, and has decreased human fatigue [9, 10]. Thus, we hypothesize that similar benefits could also be gained by introducing automation to specific aspects of surgery, provided that we can successfully solve the challenges of this concept [11]. In fact, reports in the general press [12] and in the FDA listing of safety alerts for medical devices [13] indicate the increasing occurrence of potentially dangerous situations during robot-assisted procedures.

In this paper we report the results achieved during the FP7 European project Intelligent Surgical Robotics (I-SUR) addressing the autonomous execution of basic surgical actions. Such technology will in the future allow surgeons to focus only on the most difficult aspects of the intervention, leaving the basic tasks to the autonomous system. In this paper we will focus on the puncturing task and in particular on the needle insertion for the cryoablation procedure. This procedure requires high accuracy and precision that a robotic system integrated with a sophisticated sensing system can guarantee.

To prove the feasibility of our approach to this problem, we develop general methods for a *cognitive surgical robotic*

architecture capable of combining sensing, dexterity, and cognitive capabilities to carry out this action autonomously. The algorithmic part is integrated with a novel, high dexterity robot specifically designed and fabricated during the project.

Currently we are improving the robotic platform to be able to autonomously execute other surgical tasks such as cutting and suturing. It is worth highlighting that several design choices made at the very beginning of this project (and reported in this paper) were also driven by these tasks to assure enough dexterity and manipulability, and to exploit the re-usability of common software components.

In summary, as an area of strategic interest and high social impact, autonomous robotic surgery requires methods and models for assessing its quality and its impact in operating room (OR) procedures and instrumentation. The objective of this paper is to report the results of our initial efforts to

1. design and fabricate a high accuracy robotic platform based on a macro-micro concept [14],
2. develop an integral diagnostic-planning-intervention workflow characterized by information and communication technology (ICT) methods and models.

The paper is organized as follows. In Section 2 we analyse the medical background relevant to the specific surgical action we want to automatize. In Section 3 the design of high accuracy phantom model of the human abdomen is described whereas Section 4 describes the design of a new surgical robot. Sections 5 and 6 present the development of new methods for interactive planning of surgery in deformable environments, intervention execution and monitoring, and of new methods for real-time data processing and medical situation awareness, respectively. In Section 7 the surgical interface is presented. These new systems and methods have been integrated and experimentally tested in Section 8. Section 9 discusses the legal implication and challenges of autonomous robotic surgery. Finally, conclusions are drawn in Section 10.

2. Medical background

The surgical action we will analyse in this paper is puncturing, and to identify a specific procedure we will focus on the insertion of a needle for the cryoablation of kidney tumours. *Puncturing* is defined as the act of penetrating a biological tissue with a needle, aiming at reaching a specified target point.

2.1 The cryoablation procedure

Percutaneous cryoablation of a small tumoural mass in the kidney is the least invasive treatment for kidney cancer based on thermal ablation, which aims at destroying neoplastic tissues through a thermal shock caused by short cycles of freezing and thawing.

The percutaneous approach, in contrast with open or laparoscopic surgery, is less invasive, decreases morbidity and ensures high efficacy by accurately targeting the cancer while preserving the healthy adjacent structures [15, 16].

Percutaneous cryoablation is performed using a tool called *cryoprobe* which is directly introduced through the skin towards the kidney tumour with the aid of clinical imaging devices (computer tomography CT, magnetic resonance imaging MRI, ultrasound US). Cryoprobes are hollow needles, similar to biopsy tools, whose temperature is conditioned by fluids circulating inside, generally argon for cooling and helium for heating. The very low temperature generated around the tip allows the freezing of the surrounding tissue, creating an *iceball* around the tumour. Rapid freezing and thawing cycles induce irreversible damage of the tissue within the iceball.

2.2 How robotics can improve the procedure

The most important issue for a puncturing task is to safely and correctly reach the target point. In fact the precision of insertion of the needle tip near the centre of the tumour is strictly correlated to the success of the treatment. For this reason, the cryoablation procedure can be improved by exploiting the intrinsic high accuracy and repeatability of robotic devices and the pre- and intra-operative images of the patient's anatomy.

Several experiences on robot-assisted percutaneous procedures have been reported in the literature in recent years. Good results have been obtained in terms of accuracy [17, 18], number of access attempts, time to successful access, and estimated blood loss and complications, compared to standard procedures where the radiologist has to rely on his/her experience [19]. The standard procedure usually requires several CT scans during the needle insertion to assess its actual position, exposing the patient to a considerable amount of radiation [20]. Thus an autonomous system able to plan and execute a puncturing procedure, managing possible hazardous events and reducing CT scans, represents a significant improvement in patient safety. Furthermore, this technology could be easily exploited in different surgical applications where accuracy and precision are important factors.

2.3 Medical and procedural requirements

To define the requirements of the robotic system it is necessary to analyse

- a. how the procedure is executed by a surgeon, and
- b. how the robot can perform the same task interacting with the operator and the partially unknown environment.

This analysis is used to 'translate' the surgical knowledge, professional experience and anatomical constraints into a mathematical formalism for the design of the cognitive

robotic architecture in all its aspects: control, sensing, dexterity, etc. Although most efficient automation is not done by duplicating human movements, here we need to ensure that a surgeon can continue the task by teleoperating the robots (teleoperation mode) in case of emergency. For this reason we strive to preserve the dexterity and cognitive aspects of the manual task.

Preliminarily, the surgical task is partitioned into subtasks and modelled as a state diagram to represent the sequence of actions to be performed. Then we select the critical variables and parameters involved in the procedure (i.e., distance to target, maximal force applied to the skin and so on) needed to trigger the transitions among the states in normal and emergency situations. Data collected by the sensing system during the intra-operative phase are used to compute these parameters and autonomously detect unexpected events or dangerous situations.

The pre-operative analysis is used to locate the tumour and to plan the insertion. The planning has to compute the end points of the cryoprobes so that the volume of the tumour is completely covered by the iceball. As a precautionary principle, cryoprobes are placed in order to generate 'killer' isotherms extending some millimetres beyond tumour edges. On the other hand, healthy tissue has to be preserved from the ablation as much as possible. Hence, we developed an optimal planning strategy that achieves whole tumour coverage (*hard constraint*) and minimizes the damage of surrounding healthy structures (*soft constraint*).

During the planning we define a set of *forbidden regions* from where the iceball has to be kept away. A safety distance of 5-10 mm is a safe distance to the bowel, ribs, nerves, spleen, liver and ureters. For this reason, a high accuracy robotic system is required to insert the needle with a position error smaller than 1 mm. Moreover, the sensing system should be able to detect critical/characteristic events such as *skin penetrated*, *tumour hit*, *tumour passed* and *forbidden region touched*.

To verify the plan quality, we developed a cryoablation simulator that computes the nominal trajectories and verifies the satisfaction of the constraints [21]. Figure 1 shows the interface of the simulator.

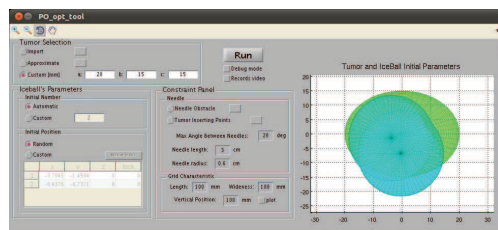


Figure 1. Graphical user interface of the cryoablation simulator from where the operator can load the CT scans of the patient

However, to compensate for registration mismatch, US guidance is required to monitor the needle path during the insertion. This is the reason for which a second robotic arm holding a US probe is needed. The control architecture has to coordinate the motion of the two arms during the procedure and avoid collisions.

The system should be able to understand how the tools are operating and what is happening on the surgical table. The accuracy of the needle insertion and the reliability of the procedure are, for the professional users, the most tangible benefits an autonomous system should offer. These characteristics are strictly related with (1) the correctness of the description of the surgical knowledge into technological processes, (2) the trustworthiness of procedural and anatomical models, (3) the acquisition of relevant data and their right interpretation, (4) the prompt detection of dangerous events and the possibility to put in action countermeasures to mitigate their effects (such as re-planning of the trajectories, teleoperation of the robots).

3. The model of human abdomen

For puncturing tests with US guidance a kidney box phantom was developed to represent the right side kidney of a human being and its surrounding structure. In order to increase the anatomical reality, a human CT scan was used to reconstruct the spatial location of the organs. Besides the kidney, the reconstruction considers also a section of liver, the ascending stretch of colon, ribs covering the liver, a simplified layer of skin and fat representing the right back side of the abdomen. The reconstruction of the models of the organs from the CT scan was made using 3D Slicer by segmenting a quarter of the right side of the abdomen as shown in Figure 2.

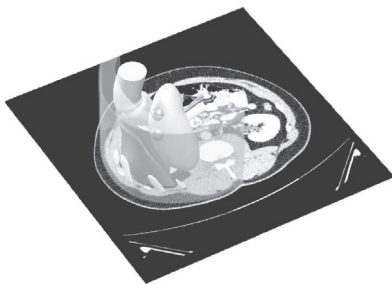


Figure 2. Region of segmented organs

The segmented organs were then imported into a CAD software (SolidWorks). A watertight box surrounding the organs, fixators for the organs, moulds for casting the organs and placement of the markers were designed in the CAD software. Two 20mm tumours were added to the lower pole on the posterior face on the kidney model. The fixators were designed to keep the liver, kidney and fat layer in place in the box.

The organ moulds were made of Polylactic Acid (PLA) using a rapid prototyper 3DTouch (manufactured by Bits and Bytes Inc). Ribs and the fixators for the liver, kidney and fat layer were fabricated in the same way.

The liver, kidney and fat layer were casted using gelatin mixtures which allowed the artificial organs to be visible on US images and CT scans. The preparation of the gelatin mixtures is described in [22]. Before casting the organs, fixators with reinforcing thin mesh were placed into the moulds. Tumours of the kidney were casted from clear gelatin mixture and were later fixed on the surface of the casted kidney by melting the gelatin between two bodies. The tumours were also covered with silicon (Elite Double 22, Zhermack SpA) mixed with graphite flakes to enhance border visibility. The box surrounding the organs was prepared from parts milled out from plywood and assembled using plastic bolts. For the descending colon we used a simple cylindrical piece of fabric attached to the phantom walls.

The liver was fixed on the wall after casting the box with bolts. The kidney was placed on two plastic rods on the box cover to stay in the middle of the box. The fat layer was fixed on top of plastic supports, then covered with coloured silicone (Dragon Skin series silicone) to represent human skin, and finally fixed from outside with a plastic strip.

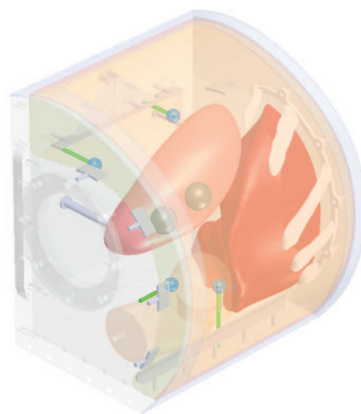


Figure 3. Placement of the US/CT markers: four blue balls on green rods

To calibrate the intra-operative US images with the preoperative CT scan, four markers were placed inside the kidney box phantom behind the organs (so that they did not shadow the organs) and as far away from each other as possible (for increasing the calibration accuracy). Markers were made of 10 mm rubber spheres fixed on 3 mm plastic tubes to the outer wall of the box phantom. Positioning of the markers can be seen in Figure 3. The visibility of the markers was further enhanced by painting the rubber balls with silicon (Elite Double 22, Zhermack SpA) mixed with graphite flakes.

The surrounding space around the kidney, liver and colon was filled with water which allows the US-based inspection of inner structures of the phantom. It was poured into the phantom box through the round opening, which was later sealed with transparent Plexiglas. The current version of the phantom has to be kept in the refrigerator and can be used for one month before organ degradation.

4. The robotic platform

Most of the existing robotic surgical platforms dedicated to autonomously achieving parts of or complete surgical interventions have been designed for one specific task, e.g., for joint replacement surgery (ROBODOC, [24]), or prostate resection (Probot¹), [25]). The automation of multiple surgical tasks with a single surgical platform, as described here, is a new major challenge, which motivated the design of a versatile and dexterous robotic platform.

Figure 4 shows the robotic platform for the needle insertion under US monitoring. The commercial robot UR5 [26] holds the US probe: the sensing system detects on the US images the motion of the needle to guarantee the safety of the procedure. The ISUR robot holds the needle and performs the puncturing according to the planned trajectory. During the needle insertion task, the US probe is first placed on the surface of the body, aligned with the expected needle tip trajectory, and then the needles are mounted on the robot end-effector and automatically inserted one by one.

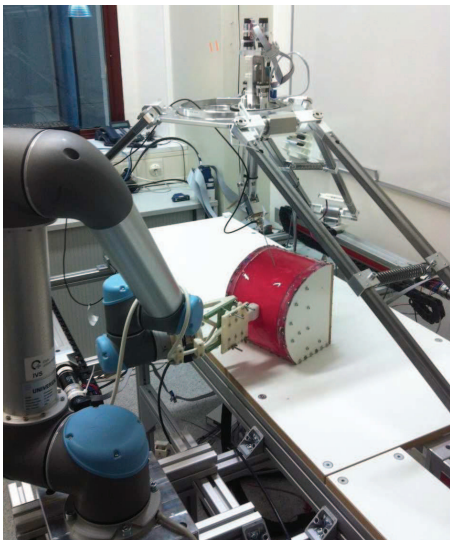


Figure 4. The overall ISUR robotic platform. On the left, the UR5 robot holding the US probe; on the right, the ISUR robot holding the needle; On the operating table, the phantom of the human abdomen.

¹ Probot is no longer on the market [23] whereas ROBODOC is sold by Curexo Technology Corporation.

4.1 Design Considerations

In order to perform automated puncturing for cryoablation a large workspace, high structural stiffness and the ability to generate output forces of up to 15N [27, 28] are required. In contrast, cutting and suturing, which will be implemented in the future by the same platform, require a dexterous end-effector capable of holding tools and performing complex manipulations similar to the hands of a surgeon, with low interaction force and within a small workspace. The minimum workspace to perform the three surgical tasks is the volume of the human abdomen plus a frame of 15 cm allowing the safe movement of the tools. Last but not least, the design of a surgical robot should consider the limited amount of space available in the operation room, and the possible interaction with other surrounding equipment, such as ultrasound probes and supporting structures used in procedures relying on intra-operative imaging.

These requirements motivated the design of a modular robotic platform based on a macro/micro unit architecture [14], consisting of two decoupled robotic structures that can be controlled independently as well as in concert (Figure 5).

- A *macro unit* with four degrees of freedom (DOF) serves as a gross positioning unit, to position the micro unit over the region of interest where the needle is to be inserted. For this purpose, a 3-DOF linear delta robot [29] was selected, as this parallel kinematics offers a rigid platform capable of carrying the weight of the micro unit, while ensuring high stiffness and positioning accuracy. The three parallelogram arms of the delta structure are actuated by three linear spindle drives. An additional DOF on the moving platform controls the rotation of the micro unit base to adjust its orientation during the surgical procedure. For the sake of convenience and space constraints, the linear delta was attached to a custom-made table 2 m in length in the first prototype. However, the arms of the delta structure could easily be flipped upwards, allowing the linear drives to be fixed to the ceiling or a supporting structure for installation in an operating room.
- A dexterous *micro unit* capable of manipulating different surgical tools is mounted to the moving platform of the macro unit. The micro unit is based on hybrid kinematics and offers 4-DOF, mimicking the arm of a surgeon (shoulder flexion/extension, shoulder rotation, elbow flexion/extension and forearm pronation/supination). In the case of the puncturing procedure, the needle is mounted to the distal end of the robotic arm of the micro unit. The first three DOF of the micro unit are used to orient the needle and are actuated remotely (from the moving platform of the macro unit) while the fourth DOF allows rotation of the needle around its axis via a belt and pulley drive located behind the needle holder.

The needle can be easily detached from its holder to allow for the successive insertion of multiple needles. The needle holder incorporates a six-axis force/torque sensor (ATI Nano 17, ATI Industrial Automation Inc., NC, USA) to measure interaction forces and torques during insertion. For more complex surgical tasks such as suturing, the needle is replaced with a cable-actuated wrist module that provides three additional DOF (wrist flexion/extension, radial/ulnar deviation, and a gripper) and can be easily attached to the force/torque sensor. A second arm with the same DOF can further be mounted to the moving base of the macro unit, resulting in a versatile, bimanual robotic surgical platform with 18-DOF.

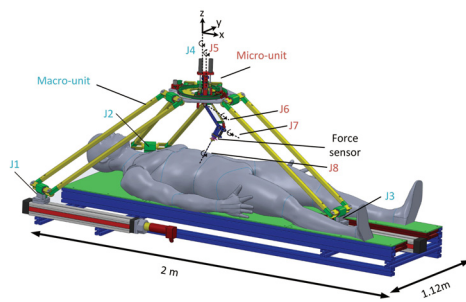


Figure 5. The robotic platform for automatic needle insertion. The robot consists of a macro unit (linear delta with 4-DOF, J1-J4) for gross positioning, and a micro unit (4-DOF, J5-J8) to hold and orient a cryoablation needle. The needle holder is attached via a six-axis force/torque sensor.

4.2 Control, Safety and Performance

Position sensing is achieved through encoders located at the level of each actuator, and through potentiometers along the drives, providing a redundant position measure for safety purposes. The end-effector position is computed by solving the kinematics of both the macro and micro units independently, and then combining them. The control architecture of the robotic surgical platform is organized in a hierarchical way. A low-level controller performs position and velocity control in a cascaded manner [30] at the joint level, and is used for trajectory following. A high-level controller implemented on a separate PC generates the commands for the automatic execution of the surgical tasks, and includes the reasoning and cognitive processes required for such tasks (the control architecture and the reasoning module will be described in the following Sections 5 and 6, respectively). The low-level control layer is implemented in real-time LabVIEW 2013 (National Instruments, USA), and runs on a PC with an eight-core Intel i-7 (3.4 GHz) processor. For optimal control of the multi-DOF robot, joint/velocity control runs at 10 kHz on an integrated field-programmable gate array board, while trajectory following is performed at 2 kHz on the PC.

Safety is a major requirement in robotic surgery. In the present scenario of a puncturing procedure, special care has

been taken to avoid collisions with the robotic arm holding the ultrasound probe (see Figure 4) and the surgical table (both during the planning and the real execution of the intervention). This is achieved by constantly monitoring the interaction forces/torques from the sensor integrated into the needle holder, as well as by monitoring motor current, position and velocity at the level of each joint. In addition to software limits (on position, velocity and current) implemented in the low-level controller, mechanical end-stops are integrated at the level of each joint. During normal operation, actions performed by the robot will be visualized on the surgical interface together with plots of the most important sensor readings, allowing the supervising surgeon to intervene at any moment to stop the system through emergency switches or take over the control through the teleoperated mode.

5. The control architecture

In this section we describe the control architecture that interacts with the low level controller described in the previous section (by sending reference positions and receiving force measurements) and with the reasoning module described in the next section (by sending and receiving events).

Validation-oriented design is mandatory for the application domain of surgical robotics. Therefore, design specifications for control algorithms and supervisory/coordination logic have been formalized using a requirements engineering approach, which is an increasingly recommended practice for safety-critical systems design (see for example the guidelines in [31]). The methodology applied in this work, described more precisely in [32], is as follows:

1. **Requirement collection:** a group of expert surgeons is interviewed on the objectives of the surgical process, the main procedures ('best practice') to be performed, the elements of the domain and the critical events related to the surgical actions.
2. **Requirements engineering:** surgical requirements are expressed using a goal-oriented methodology called FLAGS (Fuzzy Live Adaptive Goals for Self-adaptive systems, see [33]), that has two main features: it focuses on real objectives of an operation and on complications that may arise during its execution; and it is based on a formal language. The *goal model* is in fact a set of formal properties in the *Alloy language* (see [34], a specification language for expressing complex structural constraints and behaviour in a software system, based on first-order logic (FOL) and linear temporal logic (LTL, [35]). For example, a leaf goal of the cryoablation requires the avoidance of *forbidden regions* (i.e., bones, nerves, other organs) during needle insertion as explained in Section 2. This constraint is specified by:

$$MP \Rightarrow !(FR \wedge (FR.needle = MP.needle))$$

This formula asserts that every time a movement is performed (event *MP*), the *needle* entity associated to the movement must not touch a forbidden region (event *FR*).

3. **Operationalization:** the goal model is transformed into a sequence of operations and adaptations, satisfying the goals of the surgical procedure. This task is formally defined as a constraint satisfaction problem and provides a sequential model equivalent to the traces of a state machine, representing the whole system behaviour that guarantees the achievement of the root goal.

4. **Modular System Design:** the state model obtained after goal-oriented analysis is refined and partitioned into the structural units of the overall automated system, implementing a collaborative and coordinated behaviour compatible with the requirements. This task is performed by applying decomposition methods from classical discrete systems theory and using unified modelling language, UML, [36] as a modelling tool, to ease the software-oriented design specification.

5. **System Verification:** formal tools such as model checking (see [37] and the related SMV tool [38] are applied to verify that the UML system model preserves the properties expressed by the goal model.

5.1 Supervisor layer

The autonomous robotic system is supervised and controlled by the following three modules, corresponding also to software units deployed on different computational platforms: a *Surgical Interface* (described in Section 7), the *Robot Controllers*, and the *Sensing system with Reasoning and Situation Awareness* capabilities (described in Section 6).

The interaction among such system components has been specified with the help of UML sequence diagrams, which represent scenarios compatible with a given collaborative behavioural specification. As an example, Figure 6 shows an admissible scenario for the cryoablation execution, focused on needle insertion under US-based monitoring.

The scenario specifies the initial setup of the surgical task, in which preoperative medical imaging data are processed by the cryoablation planning algorithm presented in [21], whose result is the optimal placement of cryoprobe needles to obtain full tumour coverage with the expected iceball, without interferences with other organs (i.e., *forbidden regions*). The needle placement is referred to the centre of the tumour, therefore the task plan, once validated by the surgeon, must be adapted to the operative scenario by means of the registered coordinate transformations calculated by the sensing/reasoning module.

The complete behavioural specification of the robot control and supervision units is given by UML state diagrams associated to the control logic for the robot holding the needle and for the robot holding the US probe. Figure 7 shows the hierarchical state machine related to the robot inserting the needle.

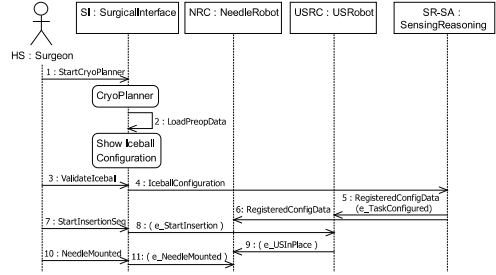


Figure 6. UML Sequence Diagram of the interaction among system components during the needle insertion

The UML state diagrams are translated in the programming language *Lua* [39] and then loaded by a component of the distributed system architecture. This component acts therefore as a supervisor of the control architecture [40].

The hierarchical features of UML state diagrams make it possible to embed exception handling mechanisms by means of transitions exiting composite states. In both state machines, in fact, the robotic task can be stopped because of an exception event that can be triggered either by the surgeons, through the surgical interface, or by the sensing/reasoning and situation awareness module. In particular, the latter is in charge of detecting if the needle is too close or even touching a forbidden region or any force value measured by the sensors exceeds a safety threshold. Whatever the exceptional event, if the task execution can be restarted after appropriate validation of the surgeons, the transitions marked by the *e_taskRecovered* event are executed. If necessary, the system allows the surgeon to switch to a teleoperated mode.

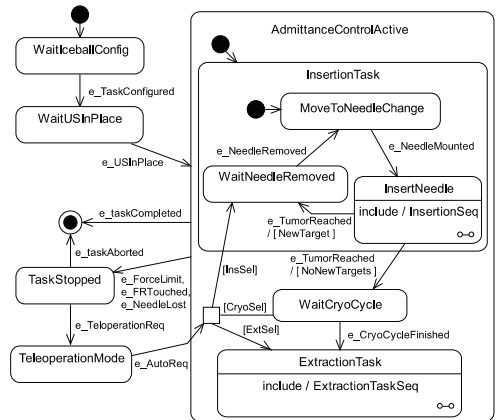


Figure 7. UML state diagram of the behavioural specification for the controller of the robot holding the needle

5.2 System architecture

The system architecture is organized according to the classification of system components shown in Figure 8. Such a classification reflects the definition of the three main modules previously described, but provides a further decomposition of software components into those whose behaviour is mainly event-driven and those performing data-driven computations.

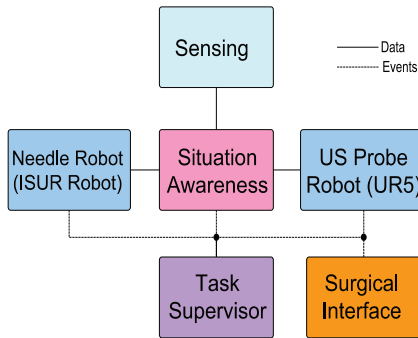


Figure 8. General scheme of the proposed control and coordination software architecture

The experimental setup described in Section 8 includes two different robots as shown in Figure 4: the macro/micro robotic platform used to perform the needle insertion and the UR5 robot used to hold and place the ultrasound probe. It follows that the planning and control system is composed of two similar control loops, one for each of the two robots. These control loops interact indirectly by exchanging events with the task supervisor.

Based on the planning created using the preoperative knowledge, the control module has to:

1. generate a valid Cartesian path (start pose) from the current robot pose and a desired one (goal pose)
2. parametrize the path in accordance to some constraints of the motion (i.e., maximum velocity and acceleration)
3. control the robot to make it follow the desired trajectory

Several distributed software frameworks are available in the literature to implement such architecture. Among others, the most used are the robot operating system [41] and the open robot control software [42]. The latter has been preferred because of its real-time properties [43].

As described in [44], an Orocos component is a basic unit of functionality that executes one or more (real-time) programs in a single thread. The *high-level control architecture* reported in Figure 9 is composed by five components:

Motion Planner: this component is in charge of planning a valid Cartesian path for a robot taking into account motion constraints. Since the complete system includes two

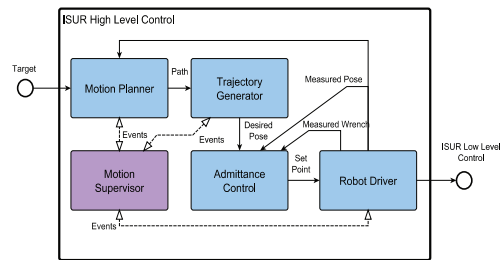


Figure 9. Interconnection scheme of robot motion planning and control components

instances of the motion planner component (one for UR5 robot and one for the ISUR robot), the path is calculated taking into account that each pose of the path must be reachable by the robot (i.e., within its workspace) and that the tool tip must not collide with anything in the operational space of the robot, including its own links (self-collisions), those of the other robot (inter-robot collisions) and other objects (obstacle collisions).

Trajectory Generator: From the start and goal poses, the trajectory generator generates a new trajectory given the path and the velocity and acceleration constraints (i.e., properties of the component).

Variable Admittance Control: a variable admittance control has been chosen for the high-level control of the ISUR robot. This choice was dictated both by the mechanical properties of the structure itself and by the need to vary the dynamical behaviour of the robot along the execution of the task. In this way it is possible to assign a different set of parameters at each different phase of the task. A passivity-based interactive control architecture has been implemented to ensure safe and stable time-varying interactive behaviours [45].

Robot Driver: to each robot a driver component is associated that is the only part of the architecture to be dependent on the specific hardware and software provided with the robot; these components have the function of being a bridge between the Orocos architecture and the outside world, receiving data from the corresponding robot and sending back set points generated by the control section.

Supervisor: the state machine describing the task is run by a component with the function of supervising the control architecture. Every component of the system is able to generate some elementary events, used to describe the progress of the architecture in implementing some action requested by the task, such as the success or failure in planning a path or generating a trajectory. All the events generated by the components are received by the supervisor and used, accordingly to the task, for the configuration and coordination of the system. The supervisor is the only event-driven component whereas the other components are updated periodically (time-driven).

5.3 Teleoperation mode

When the cognitive system is no longer able to complete the execution of the surgical procedure due to unexpected or unmanageable events, the surgeon has to take over the control of the surgical robots. We implemented a two-layered bilateral control architecture that ensures safe behaviour during the transition between autonomy and teleoperation and still retains high performance control after the switch, [46].

When the surgeon switches the robot platform from an autonomous mode to a teleoperated mode, it is likely that a kinematic mismatch occurs between the pose of the master console and that of the surgical robot (i.e., the slave robot). This mismatch can impose a high workload on the surgeon to mentally compensate the offset, and can therefore lead to risks for the patient because of unintentional motions transmitted to the robot. These problems are highly undesirable because the teleoperation mode is activated during critical situations, and mistakes in the teleoperation can cause severe injury to the patient. While many bilateral teleoperation control strategies ensuring efficient and safe behaviour have been proposed in the literature [47], to the best of the authors' knowledge there are no bilateral teleoperation systems where the safely switching between autonomous and teleoperated modes and kinematic mismatches compensation are proved in formal ways [48]. The passivity-based interactive control architecture shown in Figure 10 allows the implementation of safe and stable time-varying interactive behaviours and a transient-free kinematically-compensated bilateral teleoperation of a surgical robot.

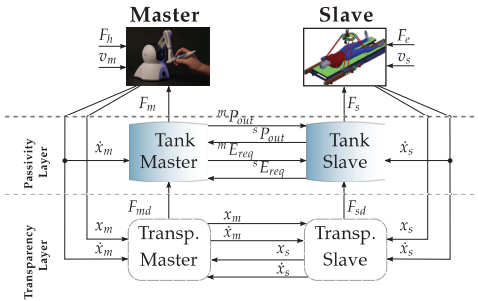


Figure 10. The two-layer architecture for the pose offset compensation. In the Transparency Layer, the desired coupling forces. These commands are sent to the passivity layer, the role of which is to check and guarantee the passivity of the total system.

6. The high level reasoning module

This section reports on the design of the real-time reasoning and situation-awareness module. This module uses intra-operative real-time sensory data and *a priori* medical knowledge to identify the task evolution and to trigger events for driving the control architecture. The module addresses the following topics: alignment of the robotic

system, registration of the subsystems (i.e., robots, phantom, US imaging), sensing techniques and, finally, development of the algorithms for reasoning and situation awareness.

6.1 Registration

The surgical scene in Figure 11 is composed of several objects: the UR5 robot holding the US probe, the ISUR robot holding the needle, the phantom of the human abdomen and the tracking system. In order for the robots to work together and to recognize the location of the phantom in the surgical scene, the robots and the phantom must be registered in a common coordinate system. This common coordinate system will be called in the following *world frame*. This preliminary phase is extremely important because it affects the overall accuracy and precision of the system and has to be done before starting any surgical procedure [49, 50].

A 6-DOF tracking system is used to estimate the transformation matrices between the local coordinate frames of the robots and the phantom. We used an Accutrack 500 from Atracsys LLC, Switzerland which is an active tracking system with a root mean square (RMS) position error of 0.19 mm [51]. The registration procedure goes through four steps as shown in Figure 11:

1. registration of the robot holding the needle,
2. registration of the UR5 robot,
3. calibration and registration of the images coming from the US probe,
4. registration of the phantom.

The letters *A* and *B* in the Figure refer to the kinematics-based transformations from the base to the end effector of the two robots, respectively.

To perform the registration we use a pointer tool attached to one of the tracking markers. The position of the pointer tool tip in the frame of the tracking system is estimated by pivoting the tip in a fixed location. The pointer tip can then be found using the estimation algorithm found in [52].

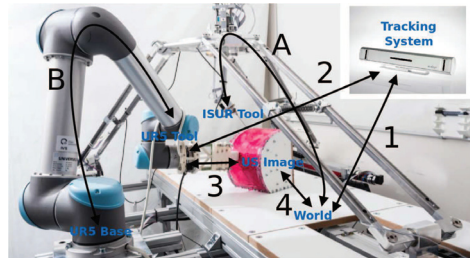


Figure 11. The four steps in the registration procedure, marked 1 to 4. A and B are the forward kinematics of the ISUR robot and the UR5 robot.

6.1.1 Robots registration

The base of the ISUR robot was defined as the world frame. The robot's base is located on the surgical table. A set of four points on the table was selected. These four points were also defined on the CAD model of the robot and measured by the pointer tool. The transformation between the world frame and the tracking frame can then be found using [53], by equating the same set of points in two different frames. This is step 1 in Figure 11.

For the UR5 robot, four points were defined on the CAD model of the US probe adapter. This defines the offset between the end effector of the robot and the measured points on the US probe adapter. The points are measured in the tracking system frame using the pointer tool. At the same time the coordinates of the same points on the base frame of the robot are obtained by using the forward kinematics and by adding the offsets from the end effector to the points. This is repeated for several poses of the robot. Using the algorithm in [54] on the two sets of points, the transformation between the base frame of the UR5 and the tracking frame can be calculated. Having the transformation between the tracking frame and the ISUR robot base frame, the transformation between the bases of the two robots is also known. This is step 2 in Figure 11.

6.1.2 US probe calibration and registration

The third step is to find out the transformation relating points in the US images and their coordinates in the world frame. The US probe is held by the UR5 robot, but the transformation between the US probe adapter and the US image is unknown and needs to be estimated. The US probe calibration is done using a single-point target phantom [55], where the target is a ball of 20 mm diameter in water mounted on a threaded rod. The location of the ball's centre in the tracking frame is obtained by acquiring the position of the top of the supporting rod before the ball is mounted. The ball's centre is also measured in the US image frame. The US stream is recorded together with the joint positions while the robot swept the probe over the ball. This acquisition is performed several times and each time the centre of the ball is manually identified. The scaling factor between the US image and the real ball size (i.e., mm/pixel) is known from the US image information. Using the position of the ball in both frames, the transformation is found using [53].

6.1.3 Phantom registration

The last step consists of registering the phantom of the abdomen. The CT scan of the phantom is used to plan the procedure and therefore the location of the phantom in the surgical table is needed to execute the procedure. The phantom has four embedded spherical landmarks (Figure 3) which are imaged using the US probe while it is mounted on the UR5 robot. Using all the previous transformations,

the position of the balls in the world frame can be calculated whereas their positions on the CT scan can be extracted via software. The transformation between the CT scan frame and the world frame is found using the same techniques as before. This is shown as step 4 in Figure 11 and completes the registration procedure.

Remark The current state of the art for the registration of scene with rigid and deformable objects is to compute a rigid registration among the objects and then measuring the deformation at run time by using intra-operative data. To evaluate the translation/rotation misalignment between pre-operative and intra-operative data we implemented a US-based segmentation of the organs inside the phantom. In this way we can evaluate the mis-registration and modify accordingly the trajectories planned on the pre-operative data. This procedure is executed before starting the autonomous procedure and not during the procedure itself². The reason is that it requires the sweeping of the US probe on the phantom to acquire the images; when the needle is partly inserted into the phantom, this procedure is no longer possible. Deformation due to the needle insertion cannot be detected in this way and the proposed solution is to track the needle tip (also using US images but with the probe away from the insertion point on the skin) to foresee a wrong path and collision with the forbidden regions. In the present setup the phantom is quite stiff and so minor deformations are expected whereas the possibility of missing the target points or moving close to the forbidden regions due to pre- and intro-operative misalignment has to be taken into account for safety reasons. The implemented algorithms will be explained in the experimental section.

6.2 Reasoning

From real-time sensor data and *a priori* knowledge of the surgical plan, the high level reasoning system is able to identify the current state in the surgical procedure by detecting the triggering events. Those events are *skin reached*, *skin penetrated*, *tumour hit* or *tumour passed* and *needle extracted*. Simultaneously, some risky situations are continuously monitored such as *force limit*, *needle tracking failed*, *forbidden region touched*.

In order to detect these events, a three-layer supervised machine learning engine is implemented

1. upper-layer reasoning with Bayesian networks
2. middle-layer Gaussian clustering with a hidden Markov model
3. lower-layer sensor filtering.

6.2.1 Bayesian Networks

Bayesian networks are used to represent the probabilistic relationship between the system inputs and the final

² This procedure is at the moment not fully automatized: the intervention of the operator is still necessary.

inference outputs [56]. A Bayesian network is either defined deterministically or obtained through a structure-learning method. This work focuses on the deterministic case.

Figure 12 shows the geometric relationship of the variables during the needle insertion towards the tumour, while Figure 13 shows the interpretation of the relationships into a Bayesian network. The Bayesian network is used for the detection of tumour hit/passed events with some given input states such as *force state*, *needle tip distance to the target*, *needle base distance to the target* and *angular error of the tip orientation to the target*. A simpler Bayesian network can be implemented to use the force and the tip distance to the forbidden region in order to detect the forbidden region touched event.

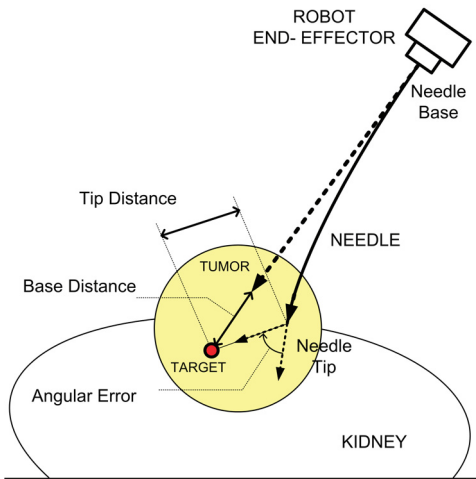


Figure 12. Definition of variables in needle insertion towards the target

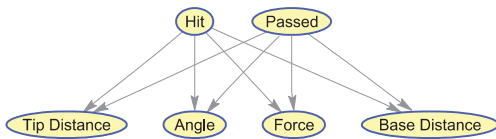


Figure 13. Bayesian network to detect tumour hit/passed events

Once the graphical model and evidence data are given, the parameter training for the model is performed in two steps: (1) the graphical model is converted to junction tree form, (2) the expectation maximization (EM) algorithm is used to estimate the training parameters.

The trained Bayesian network is able to infer on the incoming real-time input. The real-time discrete input states such as *force state*, *needle tip distance to the target* etc. are obtained from the hidden Markov model layer which is explained in the next section.

6.2.2 Hidden Markov Model based clustering

The hidden Markov model (HMM) method is a key algorithm in many applications, from hand-written character recognition to genome analysis and robotics. HMM is an outstanding machine learning algorithm to deal with sequential data classification. It involves a learning process and an inference process.

Figure 14 shows the graphical model for each of the HMMs being applied for the developed Bayesian network states such as *force state*, *needle base distance to the target* etc.

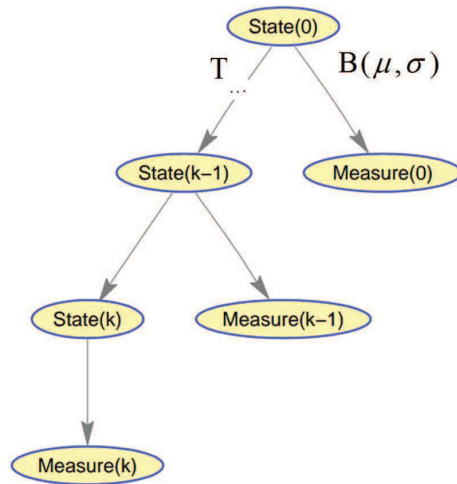


Figure 14. Sequence of observable vectors and states in the HMM

Each state of the HMM, namely hidden state, is assigned with a number from one to five. A five-dimensional ergodic HMM graphical structure is used that enables any state switching from one to five according to the probability transfer matrix T . Each measured state of the HMM is linked to a hidden state via a 2D probabilistic density function B . Because the sensor observation is considered Gaussian distributed, B is expressed in terms of a mean vector μ and a covariance matrix Σ [57]. The 5×5 dimensional transfer matrix T together with the matrices μ and Σ are estimated using the Baum-Welch learning algorithm. Subsequently, the inference process is performed using the *forward-backward algorithm* [58].

Observable vectors are formed by the iteration number k and the output of the active filters.

6.2.3 Active filtering

The force measurements are usually affected by a significant amount of uncertainty and noise; so is the vision-based needle tracking output. The developed Bayesian networks and HMM inferences are sensitive to uncertainty and noise [59]. Hence, active filters should be used to reduce the

sensor noise from the data to an acceptable level before being processed by the Bayesian networks and the HMM.

Two kinds of active filters have been implemented: a Kalman filter and a particle filter. The Kalman filter is applied to sensor data such as force measurements. A particle filter is implemented on the needle tracking algorithm because the input data are not Gaussian [60].

7. The graphical interface

The functionality, layout and appearance design of a surgical interface critically affects surgeons' ability to successfully use new robotic technologies and perform operations. Symbol size, contrast, colour and display depth and shape coding are important factors for facilitating the rapid identification of information from the user interfaces [61]. There are basic design principles that help to reduce uncertainty for all graphical user interfaces (GUI): (a) internal consistency and clear hierarchy of the elements [62]; (b) correct alignment of visual elements to reduce the visual load of the user and to help the user to understand the information structure [63]; and (c) relative scale of the elements to visualize functions in balance [64].

Various methods such as contextual inquiry, cognitive task analysis, usability tests, heuristics, cognitive walkthrough and focus groups have been used to determine design requirements for surgical interfaces [65]. Heuristic evaluation, which has previously been used to collect user feedback for radiotherapy systems [66], is an inexpensive and efficient method. However, heuristic evaluation is not enough as a standalone method [67]. Semi-structured interviews [63] and user observation [68] are the other methods used throughout the process together with user scenarios, personal and thematic analysis to pinpoint certain patterns in the surgical interfaces.

The choices for designing the surgical interface (SI) for the kidney tumour cryoablation procedure have been driven by (a) literature review, (b) eye-tracking studies [69], and (c) heuristic evaluation with the different prototypes [70].

The SI has been developed using Microsoft Visual Studio 2010 Development Environment and routines are written using C Sharp programming language. The visualization toolkit [71], which is an open source and freely available software, is used for 3D image processing and visualization to increase ease of use and efficiency [72, 73, 74].

The panels, buttons, windows in the developed SI have been organized to increase usability (Figure 15) [69]. The following functions have been grouped in the new currently used SI:

- surgery presentation: CAD model view, setting functions for CAD model view (organs, objects/tools, view angle), CT views (axial, coronal and sagittal),
- commands: cryoablation planning tool, iceball configured, new needle, ask extraction, and

- background information: e.g., robot applied forces.

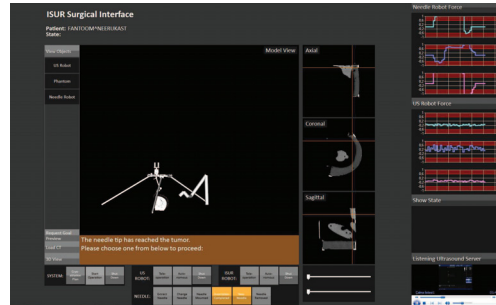


Figure 15. Surgical interface of the cognitive robotic system

Information Structure	prev.	current
The information is structured in a way that it is easy to understand the whole system.	5	5
Related information is grouped.	4	4
It was easy to find where to start from.	4	4
All visual elements on the screen were needed, nothing was excessive.	4	5
The command language employs user jargon and avoid computer jargon.	4	4
In any given time, it was easy to understand where you are.	4	5
Layout Design		
At any time, it was easy to find what I was looking for.	5	5
Related information and components are visibly grouped.	5	5
When popups and warning messages appear, I was able to see the part of the GUI that has the error.	5	5
The use of popup and warning screens distracts my attention.	2	1
Appearance		
The visual design of the GUI was consistent.	5	5
Buttons and interactive parts were easily recognizable.	5	5
Texts were readable.	5	5
The system gave feedback to every interaction I made.	5	5
Buttons and interactive components are easily manipulated.	5	5

Table 1. User Feedback Usability Survey

Important task and information panels (3D phantom, robot models, CT scan) are placed in the centre, and all log screens are located on the right side to help surgeon to focus on the important parts of the cryoablation procedure. Additionally, task-related buttons are placed at the bottom to avoid the hand covering the screen while 'turn off' buttons for each robot are placed at the top. Furthermore, patient information is added on the top of the screen for a consistent interface, and each component (windows, buttons,

texts) is aligned for faster visual grouping and directing of attention.

Surgeons are informed with a warning and process dialogue. Warning messages are displayed, overlaying on the model without covering the background when an unexpected situation happens, and optional functions are given by highlighting the regular buttons at the bottom.

A survey has been prepared to evaluate previous SIs and the currently used SI (Figure 15) in term of usability (i.e., information structure, layout design and appearance). The scores are 1-strongly disagree, 2-disagree, 3-neutral, 4-agree, 5-strongly agree, and the six participants were from the Department of Faculty of Medicine, Istanbul University: three surgeons (all male) from the Urology Department, and three radiologists (two female and one male) from the Radiology Department have filled the survey. All urologists had experience with laparoscopic surgery, and radiologists had experience in kidney biopsy process. No participants had any prior experience using a SI. It could be seen from Table 1 that the SI currently used has been improved compared to the previously developed SI in term of usability [72, 73, 74, 69].

8. Experimental results

In this section we describe a complete puncturing experiment and show how the proposed robotic system autonomously performs the insertion of the needle into a phantom of the human abdomen. The planning was done based on the CT scan and reference trajectories were designed for the UR5 robot holding the US probe and the ISUR robot holding the needle.

8.1 Planning

A CT scan of the kidney box phantom was done in the East-Tallinn Central Hospital using a multidetector CT scanner (Brilliance 64, Philips Healthcare) as shown in Figure 16. This scan is the preoperative model of the abdomen used during the planning of the surgical procedure. Sub-millimetre layer thickness is used in order to reconstruct the forbidden regions with minimal volume loss in the later phase (the scan layer thickness was 0.9 mm).

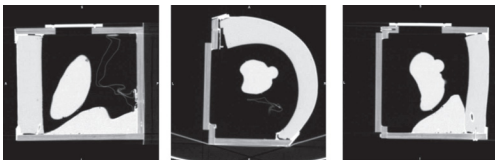


Figure 16. CT scan of the kidney box phantom (kidney in the middle of images, part of the liver seen on the right and left images, colon made out of cloth visible on the left and middle image)

The CT scan of the kidney box phantom has been segmented using 3D Slicer software and 3D STL format models are

created for the detection of forbidden regions later in the preoperative planning and also for US-CT registration. Figure 17 shows the reconstructed kidney box phantom from the CT scan.

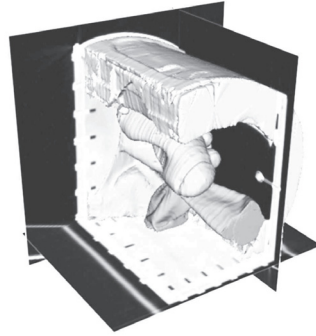


Figure 17. Reconstructed kidney box phantom model from the CT scan

Using this preoperative model the planner provides the minimum number of cryoablation needles to safely cover the tumour and the corresponding poses (target positions of the needle tip and orientations of the needle). Figure 18 shows the 3D rendering of the pose of the cryoablation needles needed to cover the tumour avoiding the anatomical features.

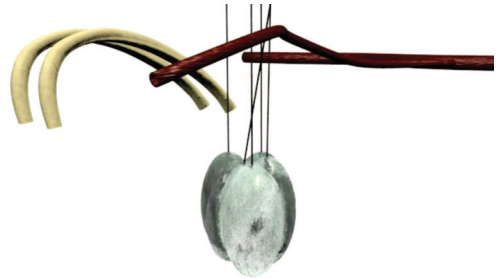


Figure 18. Cryoablation planning. 3D rendering of the pose of the cryoablation needles needed to cover the tumour, avoiding the anatomical features: ribs in white (top-left) and vessels in red (top-right).

Due to the possible deformation of the phantom we implemented a US image segmentation for detecting the registration mismatch between pre- and intra-operative data and to eventually compensate it by modifying the planned needle poses (this procedure is currently performed manually by the surgeon).

8.2 Ultrasound Image Segmentation

Ultrasound image segmentation plays an important role in the intra-operative processing. The ultrasound image segmentation can be used for the detection of the organs' borders, the guideline of surgical tools, the registration of

organ deformation, and the localization of the robot end-effector.

The speckle noise in ultrasound images affects the segmentation result and the segmentation of a heterogeneous object is difficult. Global region descriptors such as mean, variance or texture of an image are usually used in image segmentation. But for an ultrasound image, the global region descriptors do not always produce a satisfactory result. In the literature, there are many approaches using the local region descriptors [75, 76] to solve the segmentation problem of inhomogeneous images.

To improve the segmentation result, we use an active contour algorithm which takes into account both the localized active contour [77] and Bhattacharyya distance [78]. In localized active contour, instead of using global statistical information, the curve evolution is driven by local region statistical information. The curve splits the neighbourhoods of each point along the curve into two parts: interior and exterior region. Bhattacharyya distance is able to measure the discrepancy between two regions and determine in which region the points near the border belong to. The segmentation result of a kidney phantom ultrasound image is shown in Figure 19. Even though the border of the kidney is weak with a discontinued edge, the algorithm is able to extract the edge of the kidney. This result proves the robustness of the algorithm and its capability to deal with inhomogeneous images. The quality of the autonomous segmentation is comparable with the manual segmentation done by expert radiologists.

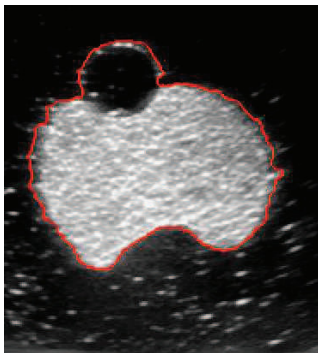


Figure 19. Segmentation Result of a kidney phantom ultrasound image

8.3 Needle tracking in US images

The US image segmentation is useful before starting the insertion of the needle. Once the needle is inserted into the phantom, to monitor the procedure we need to estimate the needle position independently of the robot kinematics. In order to track the needle tip in US images during the execution of the insertion, the method developed in [80] has been applied. The method is divided into three steps:

1. needle detection in the image,
2. estimation of the needle axis (i.e., orientation and entry point on the phantom skin),
3. localization of the needle tip along the axis.

Five features are calculated at run time along the axis and combined into one objective function by using weights. The weights are trained to optimize the tracking. The needle tip is estimated to be where the objective function has its maximum, and since we use multiple features the estimation is reliable and robust against noise and small needle bending [80].

Figure 20 shows the detection of the needle tip during the execution of the surgical task. The knowledge of the pose of the needle is exploited in the situation awareness module to detect when the tip reached the target point or if some potentially dangerous situation may occur (e.g., the needle is too close to a forbidden region).

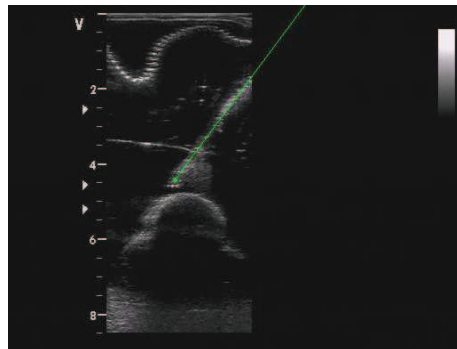


Figure 20. Example of needle tracking during the puncturing

8.4 Situation awareness

Before the ISUR robot starts the needle insertion, the UR5 robot locates the ultrasound probe in a planned pose where the needle should be seen during the puncturing. This nominal pose could be changed at run-time by the surgeon in teleoperated mode if registration errors prevent seeing the needle in the US images. In the present case the rigid registration is quite accurate and so no compensations are needed. However, in the future small translation and rotation of the US probe around the nominal pose will be executed by the robot in an autonomous way to optimize the view of the needle in the US image.

A preliminary step is the offline training of the situation awareness module. US images, together with force sensing and robot kinematic information, were acquired in slightly different needle configurations (i.e., final poses) until the outcome was reliable and robust. A sample of validation is shown in Figure 21. The robot base distance to the target was computed using the ISUR robot kinematics and the

path planning information. The tip distance to the target and the angle to the target were estimated by the needle tracking algorithm from the tip position and the needle orientation. Making use of this information, the Bayesian network computed the probability of the reasoning event 'tumour hit' as shown on the bottom plot.

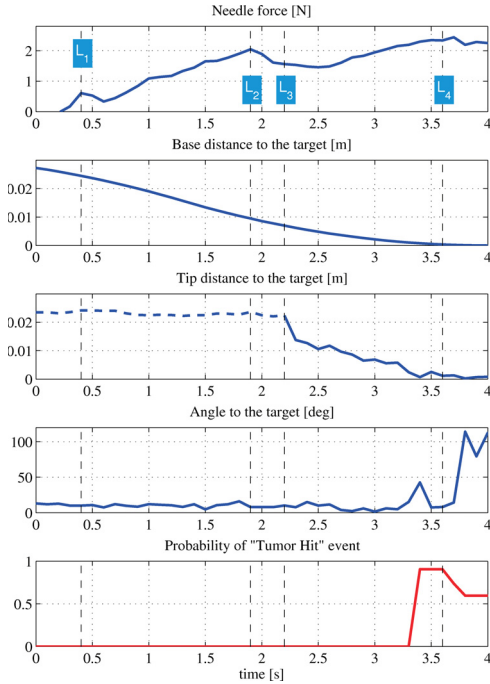


Figure 21. Training of the Bayesian network. L_1 : skin reached, L_2 : abdomen wall penetrated, L_3 : needle tracking started, L_4 : target reached

8.5 Execution

During the puncturing task the ISUR robot must behave in different ways depending on the environment it interacts with. Therefore the robot tool stiffness must change depending on the task phase as described in Section 5. For example, the robot can be compliant in free motion, while it has to be stiff for penetrating the skin and the tumour.

To demonstrate that the system remains stable despite the stiffness changes we also consider different ways of varying the stiffness profile as shown in Figure 22. For example, during the movement of the robot to the position of needle change, the stiffness is augmented gradually (final part of phase A), whereas when the robot is waiting for the needle to be mounted, the stiffness is changed instantly (from phase A to B).

For sake of clarity, the following plots show only the data regarding the translational coordinates x , y and z . Similar results have been obtained for the rotational coordinates.

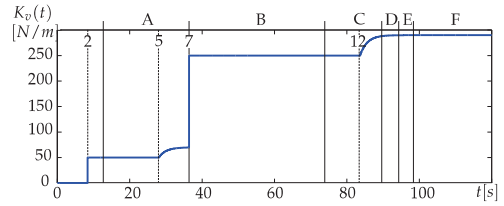


Figure 22. Evolution over time of the values chosen as diagonal elements for the variable part of the stiffness matrix during the autonomous needle insertion. Phases: *A* Move to start position to needle loading position, *B* : Wait until the needle is mounted, *C* : Approach the phantom, *D* : Penetrate the skin, *E* : Move to the target point inside the tumour, *F* Wait until the needle is removed.

The desired Cartesian translational positions computed by the admittance controller are reported in Figure 23. As expected, the commanded motion does not diverge (neither oscillate) over time and the system remains stable despite the many changes of stiffness. Figure 24 shows that the tracking error during the insertion of the needle (phase E) is below the acceptable value of 1mm, thanks to the high values of the stiffness in this phase.

During the insertion of the needle the reasoning module was active to monitor the execution of the task. The Bayesian network was processing actual measurements coming from the sensing system and the needle tracking algorithm, and was sending events to the supervisor component within the high-level control architecture.

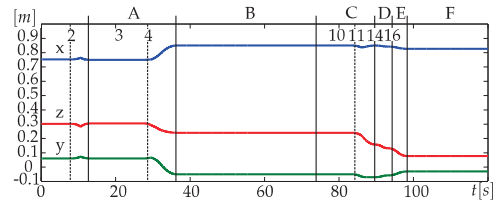


Figure 23. Desired Cartesian positions computed by the admittance controller

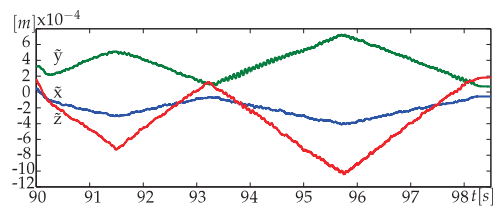


Figure 24. Tracking error (i.e., difference between the position of the robot end-effector and the desired trajectory) during the approach and insertion phases

An initial characterization of the robotic surgical platform revealed that the workspace is sufficient to cover the entire

abdominal area of a human, and that positioning precision is acceptable (<1mm), while accuracy was not (up to 7 mm positioning error, compared to 1.04 mm [81], 2 mm [82] or [83]). The latter is currently being improved through a detailed calibration of the platform. During the needle insertion the interaction forces was smaller than 5N satisfying one of the safety requirement.

9. Legal aspects

In this section we analyse the legal barriers to the introduction of robotic surgery devices in medical facilities. No ad hoc regulation exists in the European jurisdiction that is specifically devoted to the topic of autonomous surgery. Two fundamental aspects have been considered: medical liability (related also to medical malpractice in case of robotic devices) and product liability (where 'product' is, here, a robotic device or machine). Consequently, the research has focused on the legal consequences deriving from activities of designing/testing/updating the robotic machines and their effective implementation.

Referring to the first aspect, we examined complex issues like 'informed consent' and the exception (or exemption) of 'advancement in scientific knowledge'. Physicians owe several different duties to the patient, including (1) the duty to describe the nature of the treatment or of the examination that the patient should undergo (and alternatives in diagnostic and/or therapeutic methods), (2) the duty to describe possible risks, outcomes hoped for and any possibly predictable negative consequences. Therefore, the patient has to receive all useful and relevant information, so that he/she can knowingly decide whether or not to accept the proposed diagnostic method and whether or not to undergo the therapeutic treatment. A core aspect of our analysis has addressed the question whether, and under what conditions, the lack of specific rules on matters like health services performed with surgical robots makes it possible to apply current rules and principles. Moreover, we have also verified which further (or different) information the patient has the right to obtain when surgical intervention is carried out with the use of a robot machine.

From the side of exception (or exemption) of advancement in scientific knowledge, 'we have exemptions from liability possibly available to producers of products which cause damages to consumers if producer proves that the state of scientific and technical knowledge at the time when the product was put into circulation was insufficient to identify the product as defective'. We are trying to verify when this exemption can be invoked and for what kind of damages, in the field of robotic surgical machines.

From the second aspect of liability (i.e., product liability), we have considered the relevance of liability in data processing (collection of data, processing and updating with state-of-the-art knowledge) and the relevance of conformity certifications (e.g., ISO certificates) and their effects on liability standards. Trying to find solutions or

responses to the above-mentioned issues, we have studied USA regulations in automated products, in particular (although it is a quite different field) the ongoing USA legislative process regarding the lawfulness of producing and commercializing automatic vehicles. In this case, automation is limited to steering, accelerating and braking motor vehicles without human intervention. In both experimental fields (motor vehicles and surgical robots) it is possible to find a common core referring to product liability and liability of users of the product who, in a negligent way, acting or omitting to act, cause a dangerous situation for the safety of someone else.

In the absence of general legislation on robot liability and of well established principles, a great role can be played by contractual regulation. Through contractual regulation we can create disclaimers or liability limitations, so that it is possible to shift the risks related to the use of the surgical robots from one to the other of the subjects involved in the surgical operations. It is worth noting that all these provisions are themselves subject to different regulatory limitations, depending on the law applicable to the contract. On the contrary, in all the cases in which the parties did not agree on a contractual regulation of the most important subjects, the lack of common principles and of uniform existing regulations will impose to verify case-by-case which is the applicable law, by means of the single conflict rules provided by the international private law of the applicable country. In most of the cases this will lead to consistently different solutions, generating uncertainty in the application of law.

10. Conclusions

In this paper we described the design and fabrication of a cognitive robotic platform for executing autonomously simple surgical tasks. We integrated new algorithms to control and monitor the procedure, together with new methods for reasoning during the execution to promptly detect errors and possible unsafe situations. A specific user interface has been designed to continuously provide to the operator the status of the procedure and through which eventually s/he can teleoperate the robots if some event occurs that the system cannot handle autonomously.

We demonstrated that the system is able to plan the intervention for the cryoablation of the kidney tumour, to execute the needle insertion, and to monitor the procedure without any intervention by the operator supervising the surgical action. The experimental validation has been performed on an anatomically accurate US/CT compatible phantom of the human abdomen.

From the viewpoint of the ISUR project, future work aims at improving the robustness of the system, at better integrating the different subsystems, and at enlarging the number of tasks that could be executed autonomously (e.g., cutting and suturing).

From the viewpoint of robotic surgery, in this paper we started to address the following issues related to automation and technology integration that will be more and more important in the near future:

- Controlled and increased patient safety. Surgical robots will need automatic control features and monitoring to make further progress in more demanding surgical procedures.
- Increased surgical automation. In spite of the progress in computer and robotic assisted surgery (CAS and RAS), automation in the operating room is still far from being a reality. The introduction of more automation will require new procedures and validation methods to support modularity and testing of the devices.
- Expanding user and intervention bases. Currently, surgical robot users are surgeons with high technology awareness and who can afford the training and risks associated with the new technologies. Since, in the near future, we should expect a significant growth in the number of surgeons involved in RAS, we need to simplify the use of the robot by adding advanced automatic features.
- Safety regulations and standards. Using automation and robotics in the operating room is not just a technological issue but depends on social acceptance, ethical issues and safety regulations and standards. We started an analysis on the 'legal lag' between technology and regulations that, if properly driven, will simplify the introduction of these technologies into the operating room in the near future.

The solution of all these challenges will help to pave the way for autonomous and semi-autonomous robotic systems within the operating room.

11. Acknowledgements

The research leading to these results has been partly funded by the European Union Seventh Framework Programme FP7/2007-2013 under grant agreement n. 270396 (Intelligent Surgical Robotics, I-SUR).

12. References

- [1] J Rosen, B Hannaford, and R M Satava. *Surgical Robotics: Systems Applications and Visions*. Springer, 2011.
- [2] P Gomes. Surgical robotics: Reviewing the past, analysing the present, imagining the future. *Robotics and Computer-Integrated Manufacturing*, 27(2):261–266, 2011.
- [3] W Korb, R Marmulla, J Raczkowsky, J Mühling, and S Hassfeld. Robots in the operating theatre—chances and challenges. *International journal of oral and maxillofacial surgery*, 33(8):721–732, 2004.
- [4] V Vitiello, S-L Lee, T P Cundy, and G-Z Yang. Emerging robotic platforms for minimally invasive surgery. *IEEE Reviews in Biomedical Engineering*, 6:111–126, 2013.
- [5] C Bergeles and G-Z Yang. From passive tool holders to microsurgions: safer, smaller, smarter surgical robots. *IEEE Transactions on Biomedical Engineering*, 61(5):1565–1576, 2014.
- [6] Peter Kazanzides, Gabor Fichtinger, Gregory D Hager, Allison M Okamura, Louis L Whitcomb, and Russell H Taylor. Surgical and interventional robotics-core concepts, technology, and design [tutorial]. *IEEE Robotics & Automation Magazine*, 15(2):122–130, 2008.
- [7] Intuitive Surgical. <http://www.intuitivesurgical.com>, Accessed on 29 Sept 2014.
- [8] A. Tobergte, R. Konietzschke, and G. Hirzinger. Planning and Control of a Teleoperation System for Research in Minimally Invasive Robotic Surgery. In *IEEE International Conference on Robotics and Automation (ICRA)*, pages 4225–4232, Kobe, Japan, May 2009.
- [9] D B Camarillo, T M Krummel, and J K Salisbury Jr. Robotic technology in surgery: past, present, and future. *The American Journal of Surgery*, 188(4):2–15, 2004.
- [10] K C Curley. An overview of the current state and uses of surgical robots. *Operative Techniques in General Surgery*, 7(4):155–164, 2005.
- [11] J Car, A Black, C Anandan, K Cresswell, C Pagliari, B McKinstry, R Procter, A Majeed, and A Sheikh. The impact of eHealth on the quality and safety of healthcare. *A Systemic Overview & Synthesis of the Literature Report for the NHS Connecting for Health Evaluation Programme*, 2008.
- [12] Amy Braverman Puma. Hands-off surgery. *University of Chicago Magazine*, Nov-Dec, 2008.
- [13] U.S. Food and Drug Administration, Computer-Assisted (Robotic) Surgical Systems. <http://www.fda.gov/>, Accessed on 29 Sept 2014.
- [14] O Khatib. Inertial properties in robotic manipulation: An object-level framework. *The International Journal of Robotics Research*, 14(1):19–36, 1995.
- [15] C Adam, A C Mues, and J Landman. Current status of ablative therapies for renal tumors. *Indian J Urol*, 25(4):499–507, 2009.
- [16] D M Clarke, A T Robilotto, E Rhee, R G VanBuskirk, J G Baust, Andrew A Gage, and J M Baust. Cryoablation of renal cancer: variables involved in freezing-induced cell death. *Technology in cancer research & treatment*, 6(2):69–79, 2007.
- [17] G Fichtinger, J P Fiene, C W Kennedy, G Kronreif, I Iordachita, D Y Song, E C Burdette, and P Kazanzides. Robotic assistance for ultrasound-guided

- prostate brachytherapy. *Medical image analysis*, 12(5):535–545, 2008.
- [18] L Maier-Hein, C J Walsh, A Seitel, N C Hanumara, J-A Shepard, A M Franz, F Pianka, S A Müller, B Schmied, A H Slocum, R Gupta, and H-P Meinzer. Human vs. robot operator error in a needle-based navigation system for percutaneous liver interventions. In *SPIE medical imaging*, volume 7261, pages 72610Y–72610Y–12. International Society for Optics and Photonics, 2009.
- [19] L-M Su, D Stoianovici, T W Jarrett, A Patriciu, W W Roberts, J A Cadeddu, S Ramakumar, S B Solomon, and L R Kavoussi. Robotic percutaneous access to the kidney: comparison with standard manual access. *Journal of Endourology*, 16(7):471–475, 2002.
- [20] S Leng, J A Christner, S K Carlson, M Jacobsen, T J Vrieze, T D Atwell, and C H McCollough. Radiation dose levels for interventional ct procedures. *American Journal of Roentgenology*, 197(1):W97–W103, 2011.
- [21] M Torricelli, F Ferraguti, and C Secchi. An Algorithm for Planning the Number and the Pose of the Iceballs in Cryoablation. In *IEEE International Conference of Engineering in Medicine and Biology Society (EMBC)*, pages 4949–4952, Osaka, Japan, July 2013. IEEE.
- [22] A Hunt, A Ristolainen, P Ross, R Öpik, A Krumme, and M Kruusmaa. Low cost anatomically realistic renal biopsy phantoms for interventional radiology trainees. *European journal of radiology*, 82(4):594–600, 2013.
- [23] E Dombre, M De Mathelin, and J Troccaz. *Characteristics and State of the Art*, pages 1–54. John Wiley & Sons, Inc., 2013.
- [24] J Pransky. ROBODOC-surgical robot success story. *Industrial Robot: An International Journal*, 24(3):231–233, 1997.
- [25] S J Harris, F Arambula-Cosio, Q Mei, RD Hibberd, BL Davies, JEA Wickham, MS Nathan, and B Kundu. The probot-an active robot for prostate resection. *Proceedings of the Institution of Mechanical Engineers, Part H: Journal of Engineering in Medicine*, 211(4):317–325, 1997.
- [26] Universal robots, <http://www.universal-robots.com>, Accessed on 29 Sept 2014.
- [27] T K Podder, J Sherman, D P Clark, E M Messing, DJ Rubens, J G Strang, L Liao, R A Brasacchio, Y Zhang, W S Ng, and Y Yu. Evaluation of robotic needle insertion in conjunction with in vivo manual insertion in the operating room. In *IEEE International Workshop on Robot and Human Interactive Communication (ROMAN)*, pages 66–72. IEEE, 2005.
- [28] B Maurin, L Barbe, B Bayle, P Zanne, J Gangloff, M De Mathelin, A Gangi, L Soler, and A Forgiione. In vivo study of forces during needle insertions. In *Proceedings of the Scientific Workshop on Medical Robotics, Navigation, and Visualization (MRNV)*, pages 415–422, 2004.
- [29] M Bouri and R Clavel. The linear delta: Developments and applications. In *41st International Symposium on Robotics (ISR) and 6th German Conference on Robotics (ROBOTIK)*, pages 1198–1205. VDE, 2010.
- [30] R G Franks and C W Worley. Quantitative analysis of cascade control. *Industrial & Engineering Chemistry*, 48(6):1074–1079, 1956.
- [31] International Society for Pharmaceutical Engineering. *GAMP (Good Automated Manufacturing Practice): Supplier Guide for Validation of Automated Systems*. ISPE, 5 edition, 2008.
- [32] M Bonfè, F Boriero, R Dodi, P Fiorini, A Morandi, R Muradore, L Pasquale, A Sanna, and C Secchi. Towards automated surgical robotics: A requirements engineering approach. In *IEEE RAS & EMBS International Conference on Biomedical Robotics and Biomechanics (BioRob)*, pages 56–61, 2012.
- [33] L Baresi, L Pasquale, and P Spoletini. Fuzzy Goals for Requirements-Driven Adaptation. In *Proceedings of the International Requirements Engineering Conference*, pages 125–134, 2010.
- [34] Daniel Jackson. Alloy. <http://alloy.mit.edu/>, Accessed on 29 Sept 2014.
- [35] A Pnueli. The Temporal Logic of Programs. In *Annual Symposium on Foundations of Computer Science*, pages 46–57, 1977.
- [36] Unified Modeling Language. www.uml.org, Accessed on 29 Sept 2014.
- [37] K L McMillan. *Symbolic Model Checking: an Approach to the State Explosion Problem*. Kluwer Academic Publishers, 1993.
- [38] K L McMillan. *The SMV language*. Cadence Berkeley Labs., 2001 Addison St., Berkeley, USA, March 1999.
- [39] Lua. www.lua.org, Accessed on 29 Sept 2014.
- [40] M Klotzbücher, P Soetens, and H Bruyninckx. Orocos rtt-lua: an execution environment for building real-time robotic domain specific languages. In *International Workshop on Dynamic languages for Robotic and Sensors*, pages 284–289, 2010.
- [41] ROS. www.ros.org, Accessed on 29 Sept 2014.
- [42] Orocos. www.orocos.org, Accessed on 29 Sept 2014.
- [43] M Bonfè, N Preda, C Secchi, F Ferraguti, R Muradore, L Repele, G Lorenzi, and P Fiorini. Distributed Control Architecture for Automated Surgical Task Execution with Coordinated Robot Arms. In *Proceedings of the 19th World Congress of the International Federation of Automatic Control, Cape Town, South Africa*, pages 10213–10218, 2014.
- [44] P Soetens. *A Software Framework for Real-Time and Distributed Robot and Machine Control*. PhD thesis, Department of Mechanical Engineering, Katholieke Universiteit Leuven, Belgium, May 2006.

- [45] F Ferraguti, C Secchi, and C Fantuzzi. A tank-based approach to impedance control with variable stiffness. In *IEEE International Conference on Robotics and Automation (ICRA)*, pages 4948–4953, Karlsruhe, Germany, May 2013.
- [46] M Franken, S Stramigioli, S Misra, C Secchi, and A Macchelli. Bilateral telemanipulation with time delays: A two-layer approach combining passivity and transparency. *IEEE Transactions on Robotics*, 27(4):741–756, 2011.
- [47] P F Hokayem and Spong M W. Bilateral teleoperation: An historical survey. *Automatica*, 42(12):2035–2057, 2006.
- [48] M Daniele Comparetti, E Beretta, M Kunze, E De Momi, J Raczkowski, and G Ferrigno. Event-based device-behavior switching in surgical human-robot interaction. In *IEEE International Conference on Robotics and Automation (ICRA)*, pages 1877–1882, 2014.
- [49] L W Clements, W C Chapman, B M Dawant, R L Galloway Jr, and M I Miga. Robust surface registration using salient anatomical features for image-guided liver surgery: algorithm and validation. *Medical physics*, 35(6):2528–2540, 2008.
- [50] D M Cash, M I Miga, T K Sinha, R L Galloway, and W C Chapman. Compensating for intraoperative soft-tissue deformations using incomplete surface data and finite elements. *IEEE Transactions on Medical Imaging*, 24(11):1479–1491, 2005.
- [51] Atracsys, <http://atracsys.com>, Accessed on 29 Sept 2014.
- [52] K Cleary, Cheng P, A Enquobahrie, and Z Yaniv. *IGSTK: The Book - For release 4.2*. Signature Book Printing, Gaithersburg, Maryland, 2009.
- [53] B K P Horn. Closed-form solution of absolute orientation using unit quaternions. *J. Opt. Soc. Am. A*, 4(4):629–642, 1987.
- [54] J H Challis. A procedure for determining rigid body transformation parameters. *Journal of Biomechanics*, 28(6):733–737, 1995.
- [55] L Mercier, T Langø, F Lindseth, and L D Collins. A review of calibration techniques for freehand 3-d ultrasound systems. *Ultrasound in medicine & biology*, 31(2):143–165, 2005.
- [56] K P Murphy. Dynamic bayesian networks. *Probabilistic Graphical Models*, M. Jordan, 2002.
- [57] S Roweis and Z Ghahramani. A unifying review of linear gaussian models. *Neural computation*, 11(2):305–345, 1999.
- [58] L Rabiner. A tutorial on hidden markov models and selected applications in speech recognition. *Proceedings of the IEEE*, 77(2):257–286, 1989.
- [59] Christopher M Bishop. *Pattern recognition and machine learning*. springer New York, 2006.
- [60] M Johannes and N Polson. Particle filtering. In *Handbook of Financial Time Series*, pages 1015–1029. Springer, 2009.
- [61] D Sawyer, K J Aziz, C L Backinger, E T Beers, A Lowery, and S M Sykes. An introduction to human factors in medical devices. *US Department of Health and Human Services, Public Health Service, Food and Drug Administration, Center for Devices and Radiological Health*, 1996.
- [62] A Altaboli and Y Lin. Investigating effects of screen layout elements on interface and screen design aesthetics. *Advances in Human-Computer Interaction*, pages 1–10, 2011.
- [63] C J Vincent, Y Li, and A Blandford. Integration of human factors and ergonomics during medical device design and development: It’s all about communication. *Applied ergonomics*, 45(3):413–419, 2014.
- [64] T Schlatter and D Levinson. *Visual Usability: Principles and Practices for Designing Digital Applications*. Newnes, 2013.
- [65] J L Martin, B J Norris, E Murphy, and J A Crowe. Medical device development: The challenge for ergonomics. *Applied Ergonomics*, 39(3):271–283, 2008.
- [66] A J Chan, M K Islam, T Rosewall, D A Jaffray, A C Easty, and J A Cafazzo. Applying usability heuristics to radiotherapy systems. *Radiotherapy and Oncology*, 102(1):142–147, 2012.
- [67] C Wu, J Jeon, J Cafazzo, and C M Burns. Work domain analysis for designing a radiotherapy system control interface. pages 224–228, 2012.
- [68] M B Privitera, M Design, and D L Murray. Applied ergonomics: Determining user needs in medical device design. In *IEEE International Conference of Engineering in Medicine and Biology Society (EMBC)*, pages 5606–5608, Sept 2009.
- [69] D E Barkana, A Acik, D G Duru, and A Duru. Improvement of design of a surgical interface using an eye tracking device. *Theoretical Biology and Medical Modelling*, 11(48), 2014
- [70] J Nielsen. *Usability engineering*. Elsevier, 1994.
- [71] Visualization toolkit, <http://www.vtk.org>, Accessed on 29 Sept 2014.
- [72] D E Barkana, M Ozkan, F Calisir, D G Duru, and A D Duru. Development of a surgical interface for cryoablation of kidney tumors. *The International Work-Conference on Bioinformatics and Biomedical Engineering (IWBBIO)*, pages 601–611, 2013.
- [73] D E Barkana, M Ozkan, D G Duru, and A D Duru. Applying human factors for design of a kidney tumor cryoablation surgical interface. *27th International Congress and Exhibition on Computer Assisted Radiology and Surgery (CARS)*, 2013.
- [74] D E Barkana and D Erol. Applying a user-centered design approach to develop a surgical interface for

- cryoablation of a kidney tumor. *The International Workshop on Human-Machine Systems, Cyborgs and Enhancing Devices (HUMASCEND 2013)*, 2013.
- [75] C Darolti, A Mertins, C Bodensteiner, and U G Hofmann. Local region descriptors for active contours evolution. *IEEE Transactions on Image Processing*, 17(12):2275–2288, 2008.
- [76] C Li, C-Y Kao, J C Gore, and Z Ding. Minimization of region-scalable fitting energy for image segmentation. *IEEE Transactions on Image Processing*, 17(10):1940–1949, 2008.
- [77] S Lankton and A Tannenbaum. Localizing region-based active contours. *IEEE Transactions on Image Processing*, 17(11):2029–2039, 2008.
- [78] T Kailath. The divergence and bhattacharyya distance measures in signal selection. *IEEE Transactions on Communication Technology*, 15(1):52–60, 1967.
- [79] L Li and M Kruusmaa. Ultrasound image segmentation with localized level set based curve evolution and rayleigh distribution. pages 139–142, 2013.
- [80] K Mathiassen, D Dall’Alba, R Muradore, P Fiorini, and O J Elle. Real-time biopsy needle tip estimation in 2d ultrasound images. In *IEEE International Conference on Robotics and Automation (ICRA)*, pages 4363–4369, May 2013.
- [81] G Fichtinger, J Fiene, C W Kennedy, G Kronreif, I I Iordachita, D Y Song, E C Burdette, and P Kazanzides. Robotic assistance for ultrasound guided prostate brachytherapy. In *Medical Image Computing and Computer-Assisted Intervention (MICCAI)*, pages 119–127. Springer, 2007.
- [82] L MMAier-Hein, A Tekbas, A Seitel, A M Franz, B Radeleff, F Pianka, S A Müller, S Satz, R Tetzlaff, I Wolf, H-U Kauczor, B M Schmied, and H-P Meinzer. Computer-assisted needle insertion for abdominal interventions. In *World Congress on Medical Physics and Biomedical Engineering*, volume 25/6 of *IFMBE Proceedings*, pages 159–162. Springer Berlin Heidelberg, 2009.
- [83] L Maier-Hein, C J Walsh, A Seitel, N C Hanumara, J-A Shepard, A M Franz, F Pianka, S A Müller, B Schmied, A H Slocum, R Gupta, and H-P Meinzer. Human vs. robot operator error in a needle-based navigation system for percutaneous liver interventions. In *SPIE medical imaging*, volume 7261, pages 72610Y–72610Y–12. International Society for Optics and Photonics, 2009.

Appendix B

Lin Li, Peeter Ross, Maarja Kruusmaa, "Ultrasound Image Segmentation by Bhattacharyya Distance with Rayleigh Distribution", in *Proc. IEEE Int. Conf. on Signal Processing: Algorithms, Architectures, Arrangements, and Applications (SPA)*, 2013, pp.149-153.

Ultrasound Image Segmentation by Bhattacharyya Distance with Rayleigh Distribution

Lin Li

Center for Biorobotics
Tallinn University of Technology
Tallinn, Estonia
lin.li@ttu.ee

Peeter Ross

Department of Radiology,
East Tallinn Central Hospital
Institute of Clinical Medicine
Tallinn University of Technology
Tallinn, Estonia
peeter.ross@itk.ee

Maarja Kruusmaa

Center for Biorobotics
Tallinn University of Technology
Tallinn, Estonia
maarja.kruusmaa@ttu.ee

Abstract—In this paper, we study the problem of ultrasound image segmentation of kidney images. We propose a new region based active contour algorithm. The energy function of our algorithm is based on Chan-Vese energy function and the Bhattacharyya distance. In our framework, a curve is evolved to partition the image into two parts. Our algorithm minimizes the differences between each part and maximizes the distance of density function between each part. In the experiments, we use images of kidney phantoms and real ultrasound medical images to validate the performance our method. The results show that by taking into account the similarity of two different regions, the proposed method is able to deal with blurry boundaries in an ultrasound image and provide good results on both phantom and patient US images.

Keywords—ultrasound image, Bhattacharyya distance, Rayleigh distribution, segmentation

I. INTRODUCTION

Ultrasound image (US) analysis has played an important part in many clinical applications. The ultrasound image has the advantage of short acquisition times, relatively low cost and use of non-ionizing radiation. The result of the ultrasound image segmentation is an organ of interest, for example heart [1], kidney or liver [3] or more importantly, a pathology of those organs which can be used for clinical diagnosis. However, due to speckle in US images [10], US image is usually of low contrast, with shadows and blurry boundaries. Therefore precise segmentation is challenging.

Active contour (AC) method is commonly used in ultrasound image segmentation [4]. In the active contour method, the segmentation problem can be treated as optimization problem. By calculating the minimum or maximum of the energy function, the active contour reaches the optimization of the energy function which is also the result of the segmentation. Active contour can be mainly divided into edge based active contour and region based region contour. Edge based active contour use image gradient for curve evolution. Region based active contour on the other hand utilize region information instead of image gradient.

In region based active contours, the region descriptors are used to represent the region information. Intensity and texture are usually meant for region descriptors. The region active contours are more robust for noisy and weak boundaries images than the edge based active contours.

Chan and Vese (CV) proposed the known region based active contour in [5]. Their method partitioned the image into interior region and exterior region. By maximizing the intensity difference between the interior region and exterior region, CV model is able to deal with noisy image. Since the medical image is usually with noise and low contrast, CV model is suitable for medical images.

However, the problem with CV method is that the approach is a global method. The energy function of the CV method does not guarantee the desired results because it only considers the global intensity information. If the image has large inhomogeneous areas, the CV method cannot provide satisfying results.

A Bhattacharyya distance based active contour method is introduced in [6]. The energy function is driven by the gradient flow of Bhattacharyya distance in [6]. In their method, the objects are identified as image regions. Their algorithm attempts to maximize the distance between the distribution of the objects' interior and the distribution of the background exterior.

In this paper, we propose a new region-based active contour algorithm for US image segmentation. The energy function of our algorithm is based on the Chan-Vese energy and the Bhattacharyya distance in a level set formulation with Rayleigh distribution. We test our algorithm on phantom and real patient US images. The results show that our algorithm can accurately segment both images.

The organization of this paper is as follows: in Section 2, we will introduce the mathematical derivation of our algorithm; in Section 3, we will describe the experimental setup; in Section 4, we will discuss the results; and Section 5 finishes with conclusions.

II. PROPOSED METHOD

A. Overview of the proposed method

In this section, we will present and discuss the details of the proposed method and its numerical implementation. Unlike some traditional level set methods using the image gradient or global information to drive the curve evolving towards the object boundaries, our method combines the advantages of the CV model and Bhattacharyya distance. The local intensity information is considered in our method. By taking into account the similarity of two different regions, our method is able to overcome blurry boundaries and noise in an US image.

The energy function of our method consists of three parts: the region term $F(C)$, the Bhattacharyya distance term $B(C)$, and the regularization component $\text{Length}(C)$. Thus, the overall energy function is:

$$E(C) = \alpha F(C) + (1 - \alpha)B(C) + \beta \text{Length}(C) \quad (1)$$

where α and β are the weighting parameters and $\alpha \in [0, 1]$.

In our model, we would like to seek a curve that partitions the image into two regions. The outcome of our algorithm is the minimization of the different between two regions and the maximization of the distance between two regions' density function.

B. Mathematical derivation

In CV active contour method, image features are assumed to be similar within a segment. In this case, the image I is assumed to be consisting of two segments with approximately piecewise-constant intensities. Suppose a curve C divides the image domain Ω into two parts, Ω_{in} and Ω_{out} , the energy functional of CV model is:

$$F(C) = \int_{\Omega_{in}} (I - u)^2 dx + \int_{\Omega_{out}} (I - v)^2 dx \quad (2)$$

where u is the mean of the intensity inside the curve C and v is the mean intensity of the region outside C .

The CV model assumes that foreground and background regions can be separated by maximizing the mean intensities between them. The energy optimization will move the curve toward the largest difference between interior and exterior means.

The global minimization of the CV energy functional does not always guarantee the desired results. When the image is noisy and the segment is highly inhomogeneous, the CV algorithm fails to produce correct result. The reason for CV model failure is that in CV model, only the mean value is used in the segmentation process. When the image contains large inhomogeneous regions, the CV method has trouble correctly segmenting the objects.

Therefore, in our approach, we incorporate the Bhattacharyya distance with the CV model. Bhattacharyya distance has a simple analytical form and it can work with arbitrary distributions [9]. By incorporating the Bhattacharyya distance, the density functions of different objects are considered in the energy function.

The Bhattacharyya distance is able to measure the similarity between two probability density functions $P_i(z)$ and $P_o(z)$ with $z \in R^N$. The Bhattacharyya distance is defined as $D = -\log B$ where B is the Bhattacharyya coefficient:

$$B = \int_{R^N} \sqrt{P_i(z)P_o(z)} dz \quad (3)$$

the range of Bhattacharyya coefficient is between $[0, 1]$. The maximization of (3) is equivalent to the minimization of D .

We assume the distribution of ultrasound image is Rayleigh distribution. The Rayleigh probability function is defined by:

$$p(I(x)) = \frac{I(x)}{\sigma^2} \exp\left(-\frac{I(x)^2}{2\sigma^2}\right) \quad (4)$$

where σ is the parameter of the Rayleigh distribution.

We use the level set framework in our algorithm. For the level-set formulation, let us define $H(\phi)$ as the Heaviside function and $\delta(\phi)$ as Dirac functions:

$$H(\phi) = \begin{cases} 1, & \text{if } \phi \geq 0 \\ 0, & \text{if } \phi < 0 \end{cases} \quad (5)$$

$$\delta(\phi) = \frac{d}{d\phi} H(\phi)$$

We calculate the inside curve σ_i and the outside curve σ_o by Maximum-Likelihood (ML). The value of σ_i and σ_o can be calculated by using the following two expressions:

$$\sigma_i = \frac{\int_{\Omega} I^2 H(\phi(x)) dx}{2 \int_{\Omega} H(\phi(x)) dx}$$

$$\sigma_o = \frac{\int_{\Omega} I^2 H(1 - \phi(x)) dx}{2 \int_{\Omega} H(1 - \phi(x)) dx} \quad (6)$$

Using the level set framework, the energy function of (1) can then be rewritten as:

$$E(\phi) = \alpha F(\phi) + (1 - \alpha)B(\phi) + \beta \text{Length}(\phi)$$

$$= \left\{ \alpha \int_{\Omega} (I - u)^2 H(\phi(x)) dx + (I - v)^2 \left(1 - \int_{\Omega} H(\phi(x)) dx \right) \right\}$$

$$+ (1 - \alpha) \int_{R^N} \sqrt{P_i(z)P_o(z)} dz + \beta \int_{\Omega} |\nabla H(\phi(x))| dx \quad (7)$$

The first deviation of (7) with respect to ϕ can be calculated as:

$$\frac{\partial E}{\partial \phi} = \alpha \frac{\partial F(\phi(x))}{\partial \phi(x)} + (1 - \alpha) \frac{\partial B(\phi(x))}{\partial \phi(x)}$$

$$+ \beta \delta(\phi(x)) \text{div} \left(\frac{\nabla \phi(x)}{|\nabla \phi(x)|} \right) \quad (8)$$

Using Euler-Lagrange equation with respect to ϕ , the first term of (8) can be calculated by:

$$\frac{\partial F(\phi(x))}{\partial \phi(x)} = -\delta(\phi(x)) [(I - u)^2 - (I - v)^2] \quad (9)$$

The second term of (8) is the Bhattacharyya distance. We calculate the Bhattacharyya coefficient with Rayleigh distribution according to the following form [11]:

$$B(\phi(x)) = 2 \cdot \frac{\sigma_i(\phi(x)) \cdot \sigma_o(\phi(x))}{\sigma_i^2(\phi(x)) + \sigma_o^2(\phi(x))} \quad (10)$$

The first deviation of $B(\phi(x))$ with respect to $\phi(x)$ can be derived as:

$$\frac{\partial B(\phi(x))}{\partial \phi(x)} = \frac{(\sigma_i \cdot \sigma_o) \cdot (\sigma_i^2 - \sigma_o^2)}{(\sigma_i^2 + \sigma_o^2)^2} \cdot \left\{ \frac{1}{A_i} \left[\frac{I^2(x)}{2\sigma_i^2} - 1 \right] + \frac{1}{A_o} \left[\frac{I^2(x)}{2\sigma_o^2} - 1 \right] \right\} \delta(\phi(x)) \quad (11)$$

where A_i is the interior region and A_o is the exterior region:

$$A_i = \int_{\Omega} H(\phi(x)) dx \quad A_o = \int_{\Omega} (1 - H(\phi(x))) dx \quad (12)$$

Hence, the evolution flow associated with minimizing the energy functional of (7) is derived as:

$$\begin{aligned} \frac{\partial \phi}{\partial t} = & - \frac{\partial E(\phi(x))}{\partial \phi(x)} \\ = & \alpha \delta(\phi) [(I - u)^2 - (I - v)^2] - (1 - \alpha) \frac{(\sigma_i \sigma_o) \cdot (\sigma_i^2 - \sigma_o^2)}{(\sigma_i^2 + \sigma_o^2)^2} \cdot \\ & \left\{ \frac{1}{A_i} \left[\frac{I^2(x)}{2\sigma_i^2} - 1 \right] + \frac{1}{A_o} \left[\frac{I^2(x)}{2\sigma_o^2} - 1 \right] \right\} \delta(\phi(x)) \\ & + \beta \delta(\phi(x)) \operatorname{div} \left(\frac{\nabla \phi(x)}{|\nabla \phi(x)|} \right) \end{aligned} \quad (13)$$

The pseudo-code of our algorithm is outlined in TABLE I:

TABLE I. Pseudo-code of proposed algorithm

-
- $k=0$, initialize ϕ^k by ϕ_0 .
 - Compute the mean value u and v inside and outside the level set ϕ^k .
 - Compute the σ_i and σ_o according to (6).
 - Calculate A_i and A_o according to (12).
 - Evolve the curve by (13) to obtain ϕ^{k+1}
 - Check if ϕ is convergent. If not, $k=k+1$ and go back to step 2.
-

III. EXPERIMENTAL SETUP

In this section we will describe our experimental setup and the evaluation method. The quantitative performance of our algorithm is evaluated by DICE coefficient [7]. The DICE coefficient is defined as:

$$\text{DICE} = \frac{2(A \cap B)}{A \cup B} \quad (14)$$

Where A is the reference region and B is the segmentation result of an algorithm. The DICE measurement is often used to

measure the accuracy of an automatic segmentation algorithm. The DICE coefficient ranges is $[0, 1]$. If there is no overlap between two regions, the DICE value is 0; if two regions are completely overlap, the DICE value is 1.

To evaluate the performance of our algorithm, we test it on 3 data sets. The first one is a small kidney tumor US image data set. This image is obtained from a radiology training phantom described in [8].

The second data set is a phantom kidney cyst US image data set consisting of two parts: noise free kidney cyst image and Salt-pepper image data sets. We first obtained kidney cyst US images. Those US images were then used to generate the Salt-Pepper data set. Two different Salt and Pepper noise density values $d = \{0.1, 0.3\}$ are added to the original kidney cyst images. The parameter d controls the total amount of noise added into the image. The larger d value, the more noise is added into the image. A density of $d = 0.3$ would be the worst case in our experiment. The third dataset contains two real patient medical images: one patient kidney cyst ultrasound image and one patient kidney ultrasound image. The reference images are obtained manually by an expert radiologist for quantitatively evaluating the segmentation results.

IV. RESULT AND DISCUSSION

In this section, we will show the results of the proposed algorithm on various phantom and real medical images. We implemented our algorithm in Matlab. All experiments are done on a PC workstation (Intel Quad Q8300, 8 GB RAM, Windows 7 Professional).

A. Phantom image segmentation results

The first data set is obtained from a kidney radiology phantom with a tumor. The border of a tumor is blurry and therefore difficult to segment. Fig.1 shows the result of the proposed algorithm on the kidney tumor image. The resolution of the first data set is 360×290 . The DICE value is $\text{DICE} = 0.9198$.

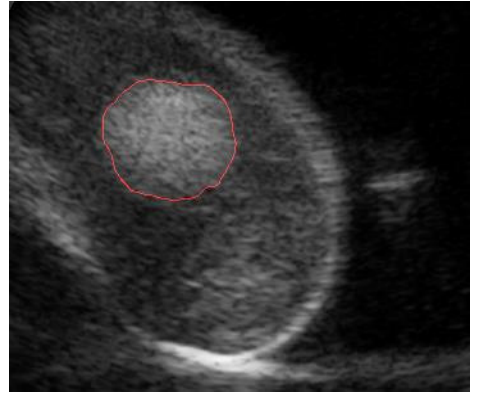
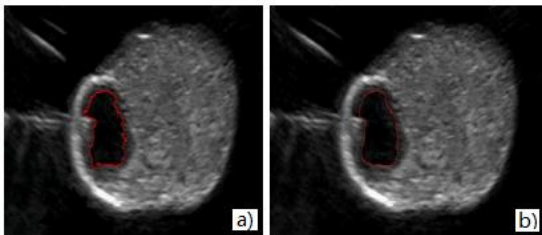


Fig.1. Kidney tumor phantom US image segment result

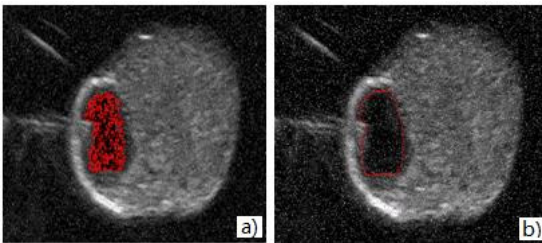
B. Sensitivity to noise

To evaluate the noise sensitivity of the proposed algorithm, we add additional noise to the US image data set. The resolution of the second data set is 520*230. Fig. 2 a) shows the result of the CV algorithm on a Salt-Pepper image. The result shows that the CV AC works well with the noise-free image, but its performance decreases when more noise is introduced to the image.

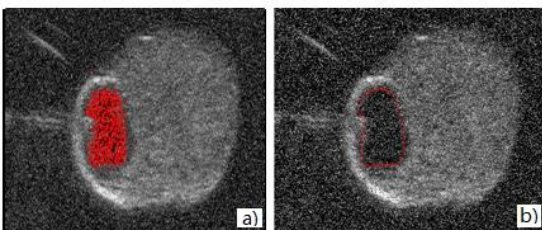
Fig.2 b) is the result of our proposed algorithm on a Salt-Pepper image data set. Our algorithm converges to the desired features on the noisy image. As we can see from Fig.2 b), when the image contains high density of noise ($d=0.3$), our algorithm can still produce accurate result.



Noise free



Salt-Pepper noise, $d=0.1$



Salt-Pepper noise, $d=0.3$

Fig. 2. Segmentation results for (a) CV algorithm and (b) proposed algorithm.

The proposed method greatly improves the segmentation accuracy for the following reasons: in our algorithm, not only local means are considered, but also local variances are considered. If only the local means are considered, the model cannot provide enough intensity change information. Therefore, some images with intensity inhomogeneity can give inaccurate segmentation results.

C. Performance on real medical images

Our algorithm was also tested on patient images. We tested our algorithm on a kidney cyst and image of a patient's kidney ultrasound image. The resolution the kidney image is 310*210. Fig. 3 is the segmentation result of the kidney cyst. The DICE value for the kidney cyst is $DICE=0.9029$.

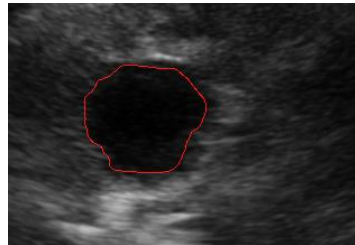
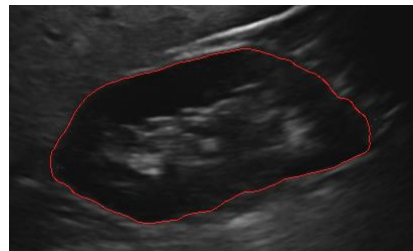


Fig.3.Kidney cyst image segmentation result

Fig.4a) shows the result of our algorithm on a patient kidney image. The resolution the kidney image is 400*240. Fig.4b) is the manual segmentation drawn by an expert. A value of $DICE = 0.9263$ is found using our approach. We can see that our algorithm can provide good segmentation result on both kidney cyst ultrasound image and the patient kidney image.



a) Segmentation result of the proposed algorithm



b) Ground truth

Fig. 4. Kidney image segmentation result

V. CONCLUSION

In this paper, a novel AC method is proposed. The proposed algorithm is based on CV model with a combination of Bhattacharyya distance. Under the assumption that the

ultrasound image can be modeled by Rayleigh distribution, and by adding an additional Bhattacharyya coefficient term into the energy function, our algorithm can drive the curve moving toward the desired edge of the object. In our algorithm, the segmentation is obtained by minimizing the difference within one segment and maximizing the distances between different regions' density function. By using the level-set framework, the proposed algorithm is able to adapt to the changing topology. Our proposed algorithm was demonstrated to accurately segment real medical images, an image of a kidney cyst and a patient's kidney. We compared the results of proposed algorithm with the CV algorithm on a noisy image data with Salt and Pepper noise. The results show that our algorithm is more robust than the CV algorithm and able to segment blurry boundaries in an ultrasound image. Currently, we only test our algorithm on static US image. Further work will test more complex or moving images.

ACKNOWLEDGMENT

This work is supported by European Union 7th Framework Programme SAFROS and ISUR projects.

REFERENCES

- [1] A. F. Frangi, W. J. Niessen, and M. A. Viergever, Three-dimensional modeling for functional analysis of cardiac images: A review, *IEEE Transaction on Medical Imaging*, pp 2–5, 2001.
- [2] Xie, Jun, Jiang, Yifeng Tsui, Hung-tat, Segmentation of kidney from ultrasound images based on texture and shape priors, *IEEE Transaction on Medical Imaging*, pp 45-57, 2005.
- [3] Hua, K. A. Segmentation of ultrasound liver images: an automatic approach, *IEEE Transaction on Multimedia and Expo*, pp 573–576, 2003.
- [4] M. Kass, A. Witkin and D. Terzopoulos, Snakes: active contour models, *International Journal of Computer Vision*, pp 321-31, 1988.
- [5] T. Chan, L. Vese, Active contour without edges, *IEEE Transaction on Image Processing*, pp266–277, 2001.
- [6] O. Michailovich, Y. Rathi, and A. Tannenbaum, Image segmentation using active contours driven by the bhattacharyya gradient flow, *IEEE Transaction on Image Process*, pp 2787–2801, 2007.
- [7] J.K. Udupa, V.R. LeBlanc. Methodology for evaluating image-segmentation algorithms, *SPIE Medical Imaging*, 2002.
- [8] A. Hunt, A. Ristolainen, P. Ross, R. Öpik, A. Krumme, M. Kruusmaa, Low cost anatomically realistic renal biopsy phantoms for interventional radiology trainees, *European Journal of Radiology*, 2013.
- [9] A. Bhattacharyya, On a measure of divergence between two statistical populations defined by their probability distributions, *Bulletin of the Calcutta Mathematical Society*, pp. 99–109, 1943.
- [10] R. Wagner, S. Smith, J. Sandrick, and H. Lopez, Statistics of speckle in ultrasound b-scans, *IEEE Transaction on Sonics Ultrason*, pp 156–163, 1983.
- [11] M. Alessandrini, D. Friboulet, O. Basset, J. D'hooge and O. Bernard, Level-set segmentation of myocardium and epicardium in ultrasound images using localized bhattacharyya distance, *Ultrasonics Symposium (IUS)*, pp 2468 - 2471, 2009.
- [12] Kass, M., Witkin, A., Terzopoulos, D.: Snakes: active contour models, *Comput. Vision*, pp 321–331, 1987.
- [13] Li, C., Kao, C., Gore, J.C., Ding, Z, Minimization of region-scalable fitting energy for image segmentation, *IEEE Transaction on Image Process*, pp1940–1949, 2008.

Appendix C

Lin Li, Maarja Kruusmaa, "Ultrasound Image Segmentation with Localized Level Set Based Curve Evolution and Rayleigh Distribution", in *Proc. IEEE Int. Conf. on Systems, Signals and Image Processing (IWSSIP)*, 2013, pp. 139-142.

Ultrasound Image Segmentation with Localized Level Set Based Curve Evolution and Rayleigh Distribution

Lin Li

Center for Biorobotics,
Tallinn University of Technology
Tallinn, Estonia
Lin.Li@ttu.ee

Maarja Kruusmaa

Center for Biorobotics,
Tallinn University of Technology
Tallinn, Estonia
Maarja.Kruusmaa@ttu.ee

Abstract— In this paper, we present a new region based active contour algorithm for ultrasound image segmentation. An energy function based on a localized region-based active contour and shifted Rayleigh distribution is formulated. In our active contour framework, the target and background are represented as small local regions and the energy optimization is calculated at each point separately. The proposed algorithm drives the evolving curve according to the shifted Rayleigh distribution in a small local area. Using this framework, our algorithm is able to handle noisy and blurry boundaries object in ultrasound image. We test our algorithm on several ultrasound images and the results show the efficiency of our algorithm.

Keywords— *ultrasound image, rayleigh distribution, level set, segmentation*

I. INTRODUCTION

Ultrasound (US) image segmentation nowadays plays an important role in computer aided diagnosis system. Compared to CT and MRI, ultrasound has an advantage of shorter acquisitions time and smaller doses of radiation. But ultrasound images contain strong speckle noises and artifacts. Therefore the quality of an US image usually is low. An US image usually contains shadows and weak borders, which makes it difficult to properly segment the correct positions and shapes of interesting objects.

In the literature, several approaches have been reported to automatically or semi-automatically detect the borders of objects from ultrasound images. Methods like region growing [4], statistical methods [5], and active contour [7] are among the most frequently used.

Active contour methods have been used in US image segmentation in recent years. Region-based active contour method [11] is one of the main categories of the active contour methods. Intensity, texture usually are used as region descriptors in region based active contour. Compared to other active contour methods, region based models generally are more robust to noise and weak image.

An US image usually contains speckle and noise which significantly affect the segmentation result. Therefore, it is important and critical to reduce the speckle and noise in an US image. Many region-based active contour algorithms are based on the assumption that an image can be approximated by global intensity [6]. However for heterogeneous objects, global

statistical region modeling techniques are usually not ideal for segmenting. In such an image, usually the objects and the background cannot easily distinguish by global methods. Because in heterogeneous images such as US images, the objects and the background usually don't have clear border, the global methods have difficulty to correctly separate the objects from background.

Chan and Vese in [2] introduced the known region based active contour algorithm. In [1] proposed an algorithm based on Chan and Vese's algorithm. The algorithm in [1] used Rayleigh distribution as a *prior* knowledge of ultrasound image and maximum likelihood (ML) was used in their algorithm. Because the algorithm proposed in [2] was a global method, when the image contained heterogeneous object or incomplete edges, this algorithm could not produce correct result.

Instead of using global methods, many groups study local intensity active contour. The segmentation results can be improved by using local intensity. For example, a local binary fitting energy region based model was proposed in [10], which is capable to deal with intensity inhomogeneity. The results in [10] showed that using local intensity information, active contour is possible to segment weak border object.

In [3] introduces a localized active contour framework. The object and background are represented by local region in the localized active contour framework. Energy optimization is calculated at each point along the curve separately. The results in [3] show that using the localized framework, active contour is able to segment objects with inhomogeneity intensity which is difficult to segment by global method.

In this paper, we propose an algorithm which is based on localized active contour framework. Since ultrasound images usually contain speckle and noise, using local region has the advantage to capture the inhomogeneous object boundary. In our method, shifted Rayleigh distribution is used as a *prior* knowledge of the ultrasound image gray scale intensity. Under this assumption, the proposed algorithm drives the active contour evolved according to the shift Rayleigh distribution of the ultrasound image in the local region at each point along the curve. We test our algorithm on different ultrasound images: phantom US images and real patient US image. From the results we can see that, our algorithm works efficiently in noisy and inhomogeneous ultrasound images.

The organization of this paper is as follows: in Section 2, we will show the Rayleigh distribution estimator; in Section 3, we will derive the localized shifted Rayleigh active contour algorithm; in Section 4, we will discuss the experimental set up and results; Section 5 is the conclusions.

II. MAXIMUM LIKELIHOOD ESTIMATOR

We will show how to derive a maximum likelihood estimator for segmentation using region-based active contours. We derive the variational flow from Rayleigh distributions of the ultrasound image.

For image I , we suppose the image intensities are independently distributed. Thus we can use the probability density function $p(I)$ to represent the image.

For a closed curve Γ which partitions the image domain into two parts: Ω_i and Ω_o . Ω_i represents the region inside the curve Γ and Ω_o represents the region outside the curve Γ . We define $p_i = \prod_{\Omega_i} p(I)$ as the probability of that pixel being inside of the curve and $p_o = \prod_{\Omega_o} p(I)$ as the probability that the pixel is outside of the curve.

A. Rayleigh distribution estimator

We assume that an ultrasound image can be represented by a *prior* distribution. In this paper we use Rayleigh distribution. The Rayleigh probability function is defined as:

$$p(I(x, y), \sigma) = \frac{I(x, y)}{\sigma^2} \exp\left(-\frac{I(x, y)^2}{2\sigma^2}\right) \quad (1)$$

where σ is a parameter of Rayleigh distribution. Let σ_i be the parametric values for the pixels inside the curve and σ_o for the pixels outside of the curve.

For the level-set formulation, let us define $H(\phi)$ as the Heaviside function and $\delta(\phi)$ as the Dirac function. The energy function $E(\phi)$ of Rayleigh distribution is obtained by:

$$\begin{aligned} E(\phi) = & \mu \int_{\Omega} \delta(\phi(x, y)) |\nabla \phi(x, y)| dx dy + \\ & \int_{\Omega} \left(\log \frac{\sigma_i}{\sigma_o} + \frac{I^2}{\sigma_i^2} \right) H(\phi(x, y)) dx dy + \\ & \int_{\Omega} \frac{I^2}{\sigma_o^2} H(1 - \phi(x, y)) dx dy \end{aligned} \quad (2)$$

The first term $\mu \int_{\Omega} \delta(\phi(x, y)) |\nabla \phi(x, y)| dx dy$ is the regularization term. The parameter μ is a scalar. The σ_i and σ_o can be calculated as:

$$\begin{aligned} \sigma_i^2 &= \frac{\int_{\Omega} I^2 H(\phi(x, y)) dx dy}{2 \int_{\Omega} H(\phi(x, y)) dx dy} \\ \sigma_o^2 &= \frac{\int_{\Omega} I^2 H(1 - \phi(x, y)) dx dy}{2 \int_{\Omega} H(1 - \phi(x, y)) dx dy} \end{aligned} \quad (3)$$

Using Euler-Lagrange equation with respect to ϕ , the evolution equation minimizing (2) can be computed by:

$$\frac{\partial \phi}{\partial t} = \delta(\phi) \left(\mu \operatorname{div} \left(\frac{\nabla \phi}{|\nabla \phi|} \right) + \log \frac{\sigma_i}{\sigma_o} + \frac{I^2}{\sigma_i^2} - \frac{I^2}{\sigma_o^2} \right) \quad (4)$$

B. Shifted Rayleigh distribution estimator

We consider the shifted Rayleigh distribution as the intensity function of the ultrasound image. The shifted Rayleigh distribution is defined by:

$$p(I(x, y), u, \sigma) = \frac{(I(x, y) - u)}{\sigma^2} \exp\left(-\frac{(I(x, y) - u)^2}{2\sigma^2}\right) \quad (5)$$

Using Euler-Lagrange equation, the evolution equation of the shifted Rayleigh distribution can be calculated as:

$$\frac{\partial \phi}{\partial t} = \delta(\phi) \left(\mu \operatorname{div} \left(\frac{\nabla \phi}{|\nabla \phi|} \right) + \log \frac{\sigma_i}{\sigma_o} + \frac{(I - u_i)^2}{\sigma_i^2} - \frac{(I - u_o)^2}{\sigma_o^2} \right) \quad (6)$$

where u_i is the mean intensity inside of the curve ϕ and u_o is the mean intensity outside of the curve ϕ . The parameter u_i and u_o can be calculated by:

$$\begin{aligned} u_i &= \frac{\int_{\Omega} I H(\phi(x, y)) dx dy}{\int_{\Omega} H(\phi(x, y)) dx dy} \\ u_o &= \frac{\int_{\Omega} I H(1 - \phi(x, y)) dx dy}{\int_{\Omega} H(1 - \phi(x, y)) dx dy} \end{aligned} \quad (7)$$

III. LOCALIZED LEVEL-SET-BASED CURVE EVOLUTION

In [3] proposed a framework which utilized the information of local region in active contour evolution. The results in [3] show that using local intensity information can increase the accuracy of segmentation. In localized active contour framework, the foreground and background region are not represented by global statistical information. The localized active contour used the small region in the curve evolution. Each point along the curve, its neighborhoods are split into two parts: interior and exterior region. The energy optimization is calculated at each single point. We use this localized active contour framework in our approach. Our method incorporates the shifted Rayleigh distribution with the localized active contour.

In the localized active contour, the localized factor is calculated by:

$$W(x, y) = \begin{cases} 1, & |x - y| < r \\ 0, & \text{otherwise} \end{cases} \quad (8)$$

where x, y represents a point in Ω and r represents a radius parameter. In the local region representation, the intensity distribution inside the curve is represented by $W(x, y) \cdot H(\phi(x, y))$, whereas outside the curve is represented by $W(x, y) \cdot (1 - H(\phi(x, y)))$.

Using this framework, we derived our evolution equation for the localized shifted Rayleigh active contour (LSRAC) algorithm as:

$$\frac{\partial \phi}{\partial t}(x) = \delta(\phi(x)) \int W(x, y) \delta(\phi(y)) \cdot$$

$$\left(\log \frac{\sigma_i}{\sigma_o} + \frac{(I(y) - u_i)^2}{\sigma_i^2} - \frac{(I(y) - u_o)^2}{\sigma_o^2} \right) dy + \mu \delta(\phi(x)) \operatorname{div} \left(\frac{\nabla \phi(x)}{|\nabla \phi(x)|} \right) \quad (9)$$

The parameter u_i and u_o in the localized framework is obtained by:

$$\begin{aligned} u_i &= \frac{\int_{\Omega} W(x, y) I H(\phi(x, y)) dx dy}{\int_{\Omega} W(x, y) H(\phi(x, y)) dx dy} \\ u_o &= \frac{\int_{\Omega} W(x, y) I H(1 - \phi(x, y)) dx dy}{\int_{\Omega} W(x, y) H(1 - \phi(x, y)) dx dy} \end{aligned} \quad (10)$$

The parameter σ_i and σ_o in the localized framework is calculated by:

$$\begin{aligned} \sigma_i^2 &= \frac{\int_{\Omega} W(x, y) (I - u_i)^2 H(\phi(x, y)) dx dy}{2 \int_{\Omega} W(x, y) H(\phi(x, y)) dx dy} \\ \sigma_o^2 &= \frac{\int_{\Omega} W(x, y) (I - u_o)^2 H(1 - \phi(x, y)) dx dy}{2 \int_{\Omega} W(x, y) H(1 - \phi(x, y)) dx dy} \end{aligned} \quad (11)$$

We compared the proposed algorithm with localized Rayleigh active contour (LRAC) algorithm. The curve evolution for the LRAC algorithm is calculated as:

$$\begin{aligned} \frac{\partial \phi}{\partial t}(x) &= \delta(\phi(x)) \int W(x, y) \delta(\phi(y)) \left(\log \frac{\sigma_i}{\sigma_o} + \frac{I(y)^2}{\sigma_i^2} \right. \\ &\quad \left. - \frac{I(y)^2}{\sigma_o^2} \right) dy + \mu \delta(\phi(x)) \operatorname{div} \left(\frac{\nabla \phi(x)}{|\nabla \phi(x)|} \right) \end{aligned} \quad (12)$$

IV. RESULT AND DISCUSSION

In this section, we will describe the experimental setup and discuss the results. All our algorithms were implemented with Matlab on a PC workstation (Intel Quad Q8300, 8 GB RAM, Windows 7 Professional).

To validate the result, Dice coefficient is used here. The Dice coefficient is defined as:

$$\text{Dice} = \frac{2(A \cap B)}{A + B} \quad (13)$$

where A and B are the reference region and the segmentation result of an algorithm. The Dice Similarity coefficient is often used to measure the accuracy of an automatic segmentation algorithm [8]. Dice similarity coefficient expresses the overlap of two regions relative to the sum of the two areas. The ranges of Dice value is [0 1]. If two regions have no overlap, the Dice value is 0; if two regions are completely match, the Dice value is 1. Segmentation results are compared with manual segmentation by a radiology expert.

We validate our algorithm on 4 different US image data sets. The first one is a kidney cyst phantom US image data set, consisting of 10 gray scale images. The images are obtained from a radiology training phantom described in [9]. We didn't

apply any filter on the original images. The segmentation result is shown in Fig.1. Table I is the Dice value of LSRAC algorithm.

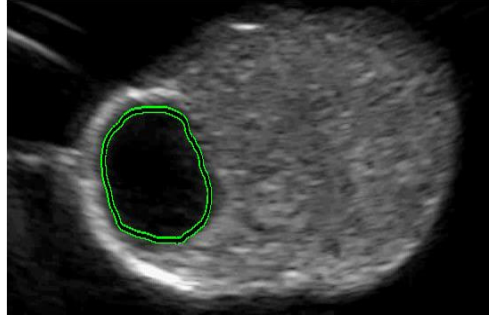


Fig.1. Segmentation result of LSRAC algorithm on US image without noise

In order to evaluate the capability of LSRAC algorithm to cope with noisy images, we created the second data set by adding salt-pepper noise to the first data set. The density value for salt-pepper noise is $d = 0.1$. The result is show in Fig. 2. The Dice value of LSRAC algorithm is in Table I. From Table I, we can see that, the LSRAC algorithm works efficiently on both on the US image without noise and in the present of noise.

TABLE I. LSRAC results on US images without noise and with noise

Dice	
US image without noise	0.9319 ± 0.0124
US image with noise	0.8993 ± 0.0132

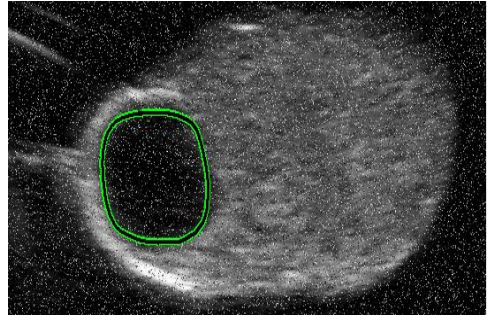
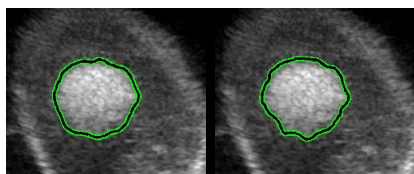
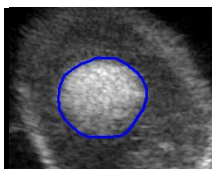


Fig.2. Segmentation result of LSRAC algorithm on US image with noise.

The third data set is obtained from a kidney radiology phantom with a tumor. The third data set also contains 10 gray scale images. Compared to a kidney cyst US image, the border of a tumor is more blurry and therefore more difficult to segment. Fig.3 (a) shows the final result of LSRAC algorithm. In Fig. 3 (b), the result of LRAC algorithm is shown. Fig. 3 (c) is the ground truth, which is segmented manually. Table II is the Dice value for LSRAC and LRAC algorithm. From Table II, we can see that, the LSRAC algorithm produces a better result than LRAC algorithm.



a) LSRAC algorithm b) LRAC algorithm



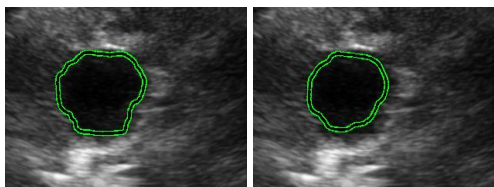
c) Ground truth

Fig.3. Kidney tumor phantom US image segmentation result.

TABLE II. LSRAC and LRAC segmentation results

Algorithm	Dice
LSRAC	0.9452 ± 0.0222
LRAC	0.9093 ± 0.0229

Furthermore, we tested our algorithm on a patient's US image of a kidney cyst. The kidney cyst can be divided into two groups: simple cyst and complex cyst. The simple kidney cyst is harmless. The complex cyst is susceptible to kidney cancer. Fig. 4 is the results of a simple cyst, in Fig. 4 (a), the segment result of the LSRAC algorithm. The Dice value for the LSRAC algorithm is Dice=0.9152. Fig. 4 (b) is the result of the LRAC algorithm and for the LRAC algorithm; Dice value is Dice=0.8386. Fig. 4 (c) is the ground truth, which is also obtained manually.



(a) LSRAC algorithm (b) LRAC algorithm



(c)Ground truth

Fig.4. Kidney cyst US image segmentation result.

We can see from the segmentation results, the LSRAC algorithm has higher Dice values than LRAC algorithm. Because the LSRAC uses both the mean μ and the variance σ of an image in the segment process while the LRAC only considers the variance σ of an image, the LSRAC produces better results.

V. CONCLUSION

In this paper, we proposed an algorithm based on localized region based active contour for ultrasound images. In this algorithm, an energy function is formulated based on the localized active contour model and the shifted Rayleigh distribution. We presented the segmentation results on ultrasound images of radiology phantoms: on a kidney cyst and a kidney tumour. The experimental results show that the proposed method can accurately segment the boundaries of a cyst and a tumor. We also applied the proposed method on a real ultrasound medical image of a kidney cyst. The segmentation results of the proposed method were compared to the segmentation result obtained with the localized Rayleigh active contour algorithm. The Dice values show that the proposed method produces better results. In our future work, we will apply the proposed algorithm on more complicated ultrasound images such as for example kidney tumor ultrasound images.

ACKNOWLEDGMENT

This work is supported by European Union 7th Framework Programme projects SAFROS and ISUR.

REFERENCE

- [1] A. Sarti, C. Corsi, E. Mazzini, and C. Lamberti, "Maximum likelihood segmentation of ultrasound images with rayleigh distribution," *IEEE Trans. Ultrason., Ferroelectr., Freq. control*, pp. 947–960, 2005
- [2] T. Chan, L. Vese, Active contour without edges, *IEEE Transaction on Image Processing*, pp.266–277, 2001
- [3] S. Lankton and A. Tannenbaum, "Localizing region-based active contours," *IEEE Trans. Image Process.*, vol. 17, no. 11, pp. 2029–2039, 2008.
- [4] X. H. X. Hao, C. Bruce, C. Pislaru, and J. F. Greenleaf, "A novel region growing method for segmenting ultrasound images," in *Proc. IEEE Ultrasonics Symposium*, vol. 2, pp. 1717–1720, 2000
- [5] Greg Slabaugh, Gozde Unal, Micheal Wels, Tong Fang, Bimba Rao, "Statistical Region-Based Segmentation of Ultrasound Images," *Ultrasound in Medicine & Biology*, vol. 35, no. 5, pp. 781–795, 2009.
- [6] J. A. Yezzi, A. Tsai, and A. Willsky, "A fully global approach to image segmentation via coupled curve evolution equations," *J. Vis. Comm. Image Rep.*, vol. 13, no. 1, pp. 195–216, Mar. 2002..
- [7] Kass, M., Witkin, A., Terzopoulos, D.: 'Snakes: active contour models', *Int. J. Comput. Vision*, pp. 321–331, 1987..
- [8] J.K. Udupa, V.R. LeBlanc. 2002. Methodology for evaluating image-segmentation algorithms. In *SPIE Medical Imaging*, 2002.
- [9] A. Hunt, A. Ristolainen, P. Ross, R. Öpik, A. Krumme, M. Kruusmaa, Low cost anatomically realistic renal biopsy phantoms for interventional radiology trainees, *European Journal of Radiology*, 2013.
- [10] C. Li, C. Kao, J. Gore, Z. Ding, Implicit active contours driven by local binary fitting energy, in: *Proceedings of IEEE Conference on Computer Vision and Pattern Recognition (CVPR)*, pp. 1–7, 2007.
- [11] Li, C., Kao, C., Gore, J.C., Ding, Z.: 'Minimization of region-scalable fitting energy for image segmentation', *IEEE Trans. Image Process.*, pp. 1940–1949, 2008

Appendix D

Lin Li, Peeter Ross, Maarja Kruusmaa, Xiaosong Zheng, "A Comparative Study of Ultrasound Image Segmentation Algorithms for Segmenting Kidney Tumors", *In Proceedings of the 4th International Symposium on Applied Sciences in Biomedical and Communication Technologies*, ACM, 2011.

A Comparative Study of Ultrasound Image Segmentation Algorithms for Segmenting Kidney Tumors

Lin Li

Center for Biorobotics,
Tallinn University of
Technology
Akadeemia tee 15A-111,
12618 Tallinn, Estonia
+372 53511055
lin@biorobotics.ttu.ee

Peeter Ross

Department of Radiology,
East Tallinn Central Hospital
Ravi tn 18, 10138 Tallinn,
Estonia
+372 6227070
peeter.ross@itk.ee

Maarja Kruusmaa

Center for Biorobotics, Tallinn
University of Technology
Akadeemia tee 15A-111,
12618 Tallinn, Estonia
+372 5183074
maarja@biorobotics.ttu.ee

Xiaosong Zheng

Center for Biorobotics,
Tallinn University of
Technology
Akadeemia tee 15A-111,
12618 Tallinn, Estonia;
Department of IT, SILC,
Shanghai University
+372 58137288

xiaosong@biorobotics.
ttu.ee

ABSTRACT

In this paper we introduce an ultrasound image segmentation evaluation framework for kidney tumor. Ultrasound image segmentation algorithms can be divided into edge based, region based, texture based, active contour and model base technique. We tested the performance of algorithms in each category using a kidney phantom and kidney cyst ultrasound image. We found that the algorithms we implemented are more suitable for relatively homogeneous kidney tumors. For more heterogeneous tumors we should use more complicated segmentation techniques and some of these advanced techniques are discussed in this paper.

Keywords

Kidney tumor, ultrasound image, segmentation, algorithm

1. INTRODUCTION

In Europe, kidney cancer accounts for nearly 3% of all cancer cases [1]. Laparoscopic partial nephrectomy or minimally invasive surgery is the standard treatment for kidney surgeon for small tumors (4cm or less). A successful partial nephrectomy means the tumor is completely remove, but some amount of healthy tissue is left in the organ. In order to do this, identification of the location and shape of the tumor inside the kidney is important. Ultrasound(US), computed tomography (CT) and magnetic resonance imaging (MRI) are currently utilized by doctor to predetermine the location, size and shape of the tumor before surgeon. Compare to CT and MRI, ultrasound has the advantage of short acquisition time, less radiation. But ultrasound images usually contain strong speckle noises and artifacts, which make it difficult to properly segment the interested objects with correct position and shape. Segmentation remains as a challenge task in pre-operative surgical planning.

Several approaches have been proposed to segment ultrasound tumor images for diagnosis of tumors, such for the breast tumor [8]. However, very little has been done in kidney tumor segmentation. In [3] the authors proposed using Ultrasound (US) to acquire images of the tumor and the surrounding tissues, then segmenting these US images to present the tumor as a three dimensional (3D) surface. In [3], it also introduced that their kidney phantom was made by poly(vinyl alcohol) cryogel material.

In this paper we will introduce our kidney phantom made from gelatin material. And we will also discuss and compare several algorithms that can be used for tumor segmentation and we will present the evaluation metrics and the evaluation results.

The organization of this paper as follows: in section 2, we will introduce a kidney phantom made from gelatin gel; In section 3, five categories of ultrasound image segmentation algorithms that used for kidney tumor segmentation are discussed; in section 4, we will present evaluation criteria; section 5, discuss the experiment set up and results; in section 6 conclusion will be presented with an outline of future research direction.

2. PHYSICAL PHANTOM

Ultrasound imaging phantoms are tissue-mimicking objects designed to match the tissue properties. Phantoms designed should possess the same acoustic properties as for the conventional ultrasound. Kidney phantoms is an useful tool for performance testing and also can be used as a training tool for medical school student to practice ultrasound guided interventional procedures like biopsy, fine needle aspirations.

The kidney phantoms that we used are based on gelatin gels which have numerously been reported in the literature as a suitable material to mimic the ultrasound properties of living tissues [4-7]. Both the ultrasound attenuation and wave propagation speed are tuned by adjusting the precise gel composition. The kidney mould is based on an actual human kidney that is segmented from a CT scan, processed to create a negative, and finally printed with a rapid prototyper. Tumors or cysts of different sizes are premanufactured using various materials and fixed in a proper location inside the mold prior to casting. By using this procedure an organ phantom with realistic

shape, ultrasound parameters and pathology is created. In this work we use a kidney phantom with ultrasound propagation speed 1450 m/s, broadband ultrasound attenuation $-0.45 \text{ dB}/(\text{cm} \cdot \text{MHz})$, and with tumors of 20 mm and 40 mm in diameter and 30-50 % lower stiffness/attenuation. Figure 1, a) is the picture of the kidney mould model; Figure 1, b) is the picture of the kidney phantom mould; Figure 1, c) is the kidney phantom with tumor inside.

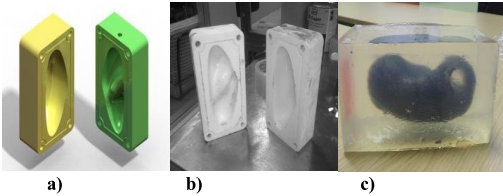


Figure 1. Kidney phantom.

3. IMAGE SEGMENTATION METHODS

The algorithms that we used for ultrasound lesions image segmentation can be divided into the following 5 categories:

- Edge or boundary based methods
- Region based methods
- Texture based methods
- Active contour methods
- Model base methods

3.1 Edge or boundary based methods

Edge or boundary based methods attempt to solve the image segmentation by detecting the edge between different regions. The edge method has the advantage that it analysis the images by drastically reducing the amount of data to be processed, while at the same time preserving useful structural information about object boundaries [9].

For ultrasound images which have inherent speckle noise and texture characteristics, edge detector only algorithms cannot achieve high quality result. Therefore, traditional edge detection method rarely used alone [13]. In [14], it introduced a combination of canny edge detector with gradient vector flow algorithm. By coupling the smoothness of the edge map to the initial size of the snake, enhancing the tumor boundaries, better tumor boundary have obtained. Different from [14], we use canny edge operator with levelset function.

3.2 Region based methods

Region based techniques is frequently used in ultrasound image segmentation. Region based method use a set criteria, like image intensity, texture, histograms, and gradient to distinguish and connect neighborhood pixels, then assign pixels to object [17-21].

Region growing as one of the most common region based algorithm, starts from seed and seed area, continues merge the neighbour pixels until the completion of all pixels of the connection. We combine region growing and other algorithms for kidney tumor segmentation. Firstly, Otu method [11] is used to assign image pixels into different class. Morphology operation, such as erosion and dilation[10] is applied later to smooth the sharp edge. After that region growing is used to obtain the interesting tumor area.

3.3 Texture based methods

Each texture can be thought as containing a narrow range of frequency and orientation components. Thus textures can be used to perform tasks such as the segment the ultrasound image into distinct objects and then analysis surface geometries. By using texture filter like multiple band-pass filters filter, the image tuned to the frequency dominant and orientation component, it is possible to localize similarities in texture image. The output of the filters can be used to determine the regions occupied by the textures.

Gabor filters is used here as our test algorithm. The Gabor filters[16], are band-pass filters with tunable center frequency, orientation and bandwidth. The filter outputs reflect the spatial and orientation composition of a texture.

3.4 Active contour methods

The active contour model, more widely known as snake, has been extensively used for US images. In active contour model, the contour deforms to minimize the contour energy that includes the internal energy from the contour and the external energy from the image. Active contour model can be divided into based on the boundary, based on region and based on hybrid active contour model and so on. We use an algorithm ACWE which was introduced in[15] for our evaluation test.

3.5 Model based methods

Markov random field (MRF) model has been used for US image segmentation[22][25]. The algorithm alternatively approximates the maximization of the posterior estimation of the class labels, and estimates the class parameters. Image segmentation using MRF model include: definition of neighborhood system; the choice of energy function and parameter estimation; minimization of energy function in order to obtain maximum a posteriori probability of the strategy.

Here, we use k-means algorithm to get initial label image estimation for MRF. K-means algorithm is a clustering algorithm. It iteratively assigns pixels to the closest cluster using a distance function, such as the Euclidean distance measure. After obtain label image, MRF is applied to segment the tumor from image.

4. EXPERIMENT SETUP

The objective of the experiments is to provide insights about both the strength and weakness of the various algorithms described in section 2 when they used for ultrasound image segmentation for kidney tumors. Section 4.1 presents the image test set. Section 4.2 presents the evaluation scheme that we used in this research.

4.1 Test Image set

A small set of 2D ultrasound images is selected to serve as the representative test set. The first image set is 40 ultrasound images taken from the Gelatin Kidney phantom. We also apply the segmentation algorithms on a patient kidney cyst image. All our experiments were done on a PC workstation (Intel Quad Q8300, 8 GB RAM, Windows 7 Professional).

4.2 Evaluation metrics

In this section, we will introduce our comparison criteria. We would like to qualitatively and quantitatively measure the performance of each algorithm. We validate our segmentation methods using a variety of evaluation methods [12]. Particularly, our segmentation is compared with the manual results that done by radiologist. The following three criteria are used to compute different between segmentation result and the reference images:

- Dice criterion: $Dice = \frac{2(A \cap B)}{A + B}$, where A and B are the reference region and the segmentation result of an algorithm;
- Peak signal-to-noise ratio: $PSNR = 10 \log_{10} \left(\frac{d}{MSE(A, B)} \right)$, where d is the maximum possible value of the image;
- Hausdorff distance:

Hausdorff = $\max(D1(A, B), D1(B, A))$, where A and B are the reference contour and the result contour of an algorithm and $D_1(A, B) = \max_{x \in A} (\min_{y \in B} (\|x - y\|))$.

The Dice Similarity Coefficient is often used to measure the accuracy of an automatic segmentation algorithm. The coefficient ranges from 0 (no overlap), to 1 (a complete overlap). Dice similarity coefficient expresses the overlap of two regions relative to the sum of the two areas.

PSNR often uses as a quality measurement between the original and a compressed image. The higher the PSNR, the better the quality of the compressed, or reconstructed image.

The Hausdorff identifies the point of A that is farthest from any point of B, and measures the distance from A to its nearest neighbor in B. Thus the Hausdorff distance, H(A,B), measures the degree of mismatch between two sets, as it reflects the distance of the point of A that is farthest from any point of B and vice versa. The small number of Hausdorff distance means the two data sets are closer to each other.

5. RESULTS AND DISCUSSION

In section 2, we introduced 5 ultrasound image segmentation algorithm categories. We test 40 kidney tumor ultrasound images from gelatin kidney phantom. Figure 2 is one example of the segmentation result from gelatin kidney phantom. In Figure 2, the blue contour is groundtruth and the white contour is the segmentation results.

5.1 Accuracy

The accuracy is one of the significant features of every algorithm. We use Dice Similarity Coefficient as evaluation of accuracy in our experiments. As we can see from table 1, the Dice Coefficient for 5 algorithms, texture segmentation, ACWE and Model base have the similar value.

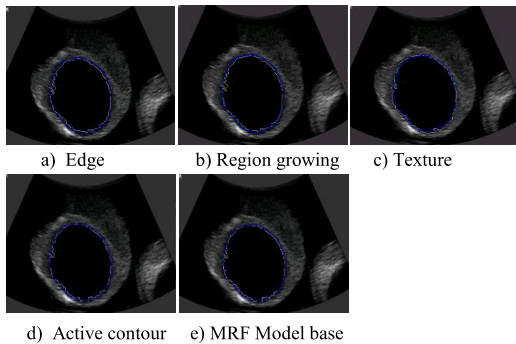


Figure 2. Segmentation results for kidney phantom.

Analysing the contours shown in Figure 2, we observed that all lesions could be detected by the segmentation methods proposed in section 2 and Dice values in table 1 for all algorithms are very similar. This is, basically, due to the fact that the gray levels of the kidney tissue are different from the lesions.

We can also observe that the shape of lesions in the images is very close to the real objects for practical purposes. Comparing the parameters in Table 1, we can notice that the Dice value of the phantom are close to 1, respectively, which indicates that segmentation contour are very close to groundtruth contour.

Table 1. Evaluation results for gelatin kidney phantom

Algorithms	Dice	PSNR	Hausdorff
Edge	0.9469	14.9842	8.7934
Region growing	0.9488	15.1398	9.2195
Texture segment	0.9694	17.0774	7.2655
Active contour	0.9669	16.7072	8.2804
MRF Model base	0.9653	16.7768	10.6862

We also tested the algorithm on a kidney cyst ultrasound image. There are two significant categories of kidney cysts: simple cyst and complex cyst. The simple kidney cyst is very common and has no risk of becoming a kidney cancer. The complex cyst refers to a spectrum of cysts that have different characteristics which may make them suspicious for kidney cancer[23]. In Figure3, a) is groundtruth defined by radiologist; b) to f) are the segmentation results from 5 algorithms.

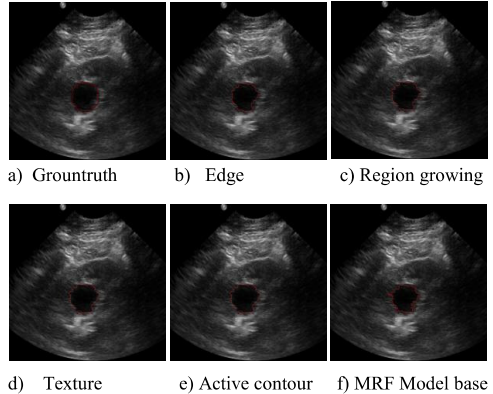


Figure 3. Kidney cyst segmentation results.

Table 2 is the comparable result of kidney cyst. From table 2 we can see that, canny edge, region growing and gabor texture algorithm have similar Dice value. Due to the speckle and noisy of ultrasound image nature, the boundary of tumor is blur. Since Hausdorff distance measures the maximum distance between two contour, Hausdorff distance is larger than table 1.

Comparing Table 1 and Table 2, we observed that the results for kidney phantom are better than patient cyst. For example, for edge algorithm, the Dice value is 0.9469 for phantom image and 0.8942

for kidney cyst. The Dice value expresses the similarity between segmentation and the groundtruth. The high value means the segment results are more overlap to groundtruth. Higher PSNR value, the better the quality or reconstructed image. The PSNR for phantom is 14.9842 and 12.4931 for kidney cyst, which also mean the phantom images has better result. The Hausdorff distance evaluates the maximum contours distance between the segmentation image and the groundtruth. The low Hausdorff distance means the segment contour closer to groundtruth contour. The Hausdorff distance is 8.7934 for phantom image and 23.0217 for kidney cyst image. Therefore, the canny edge algorithm produces better result on phantom image than kidney cyst image. The other four algorithms also have the same situation.

Table 2. Evaluation results for kidney cyst

Algorithms	Dice	PSNR	Hausdorff
Edge	0.8942	12.4931	23.0217
Region growing	0.8915	12.5479	22.6716
Texture segment	0.9072	12.8794	19.4165
Active contour	0.8330	10.9452	26.9258
MRF Model base	0.8699	11.8220	26.4008

When implementing segmentation algorithm, the parameter initialization or definition is important. For region growing, one of the problems of region growing is seed point selection. The seed point usually need user predefined. Adaptive region growing, such as in [2], give a solution for automotive region growing segmentation which can select a seed point without user participation.

Canny edge has several parameters. The crucial parameter is δ , which is the standard deviation of the low pass smoothing filter parameter. According to [14], if the tumor was large, a larger sigma ($\delta=3$ or 4) was applied on the US image and for small tumors smaller sigma ($\delta=1.5$) is chosen.

The gabor filter parameter estimation can be divide in to two group: the filter-bank approaches and the filter-design approaches. In filter-bank approaches, the filter parameters are present ad hoc and are not necessarily optimal for a particular processing task. In filter-design approaches only one or a few filters for a particular application are designed in an effort to reduce the difficulties of filter-bank approaches [26].

For ACWE, this algorithm has one specific parameter that can be modified, the curvature term. It weights the influence of the regularization term of equation. For our experience, we choose 0.2. More detail can be found in [12].

5.2 Computational Time

We compared the computational time demands of the tested methods for the Gelatin Kidney phantom. The image data sets for Gelatin Kidney phantom were used for this purpose. Moreover, we resized these images to the different sizes in order to highlight the dependence of the methods computational time demands on the image size. The image size are 50×50 pixels, and image data set were resized to the sizes 100×100 , 200×200 , 400×400 , 500×500 and 600×600 pixels.

Figure 4 is the calculation time for five algorithms. As we can see from Figure 4, the calculation time increase as the pixels in image increase. MRF Model base and gabor texture have higher calculation time when dimension of image increase, while active contour ACWE, canny and region growing the increase rate is small, especially for region growing. For gabor texture filter, because it contains a bank of filter, the speed is usually slow. Because the model base method we use MRF and k-mean algorithm, and calculation time for k-mean is account for half the total time. Therefore, the whole running time for MRF model base algorithm is large.

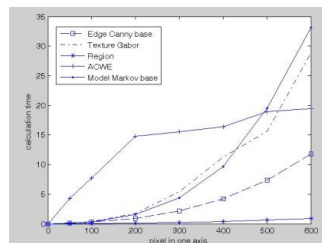


Figure 4. Calculation time of five algorithms.

6. CONCLUSION

In this paper, a phantom adequate to mimic the appearance of kidney lesions with regular contour in ultrasound images, was developed. Based on the evaluation of parameters, the contour of the simulated lesions was found to be regular and consistent with the real physical phantom.

We also evaluated different kinds of techniques for medical image segmentation on the kidney phantom. The tested algorithms could be divided into five categories: edge based, texture, region growing, active contour, and MRF Model based algorithm. We focused on the method accuracy, computational time and implemented the 5 algorithms in experimental tests. The evaluation metrics we use here are Dice, PSNR, and Hausdorff distance.

It is noted that the algorithms we implemented are more suitable for relatively homogeneous kidney tumors, and would not be that effective in heterogeneous lesions. For heterogeneous lesions, which contain inhomogeneous area, a more sophisticated segmentation technique that relies on local image intensity discontinuities is needed to get precise result. More powerful techniques, such as level sets with texture, and shape prior statistics information, may be used to adapt to segmenting structures with more geometric complexity and reducing underestimations of the tumor's boundary.

Considering calculation time, in [24], the authors presented a modification model for ACWE. They use a global minimization method with a dual formulation of the total variation norm perform the contour evolution. From their result, the calculation time reduces significantly and it is possible to realize real time calculation, which makes it a possible solution to real time tumor ultrasound image segmentation.

7. ACKNOWLEDGMENTS

This work is supported by European Union 7th Framework Programme SAFROS and ISUR projects.

8. REFERENCES

- [1] Ferlay, J., et al. 2007. Estimates of the cancer incidence and mortality in Europe in 2006. *Ann Oncol.* DOI= 10.1093/annonc/mdl498.
- [2] S. Poonguzhali, G.Ravindran, A Complete Automatic Region Growing Method for Segmentation of Masses on Ultrasound Images. DOI=10.2991/jcis.2008.57.
- [3] Anis Ahmad, Derek Cool, Ben H. Chew, Stephen E. Pautler, Terry M. Petersa. 2006. 3D Segmentation of Kidney Tumors from Freehand 2D Ultrasound. *Proceedings of the SPIE*, 6141, 227-237. DOI=10.1117/12.653848.
- [4] R. O. Bude and R. S. Adler.1995. An easily made, low-cost, tissue-like ultrasound phantom material. *Journal of clinical ultrasound* ,23, 4, 271-3, May. DOI= 10.1002/jcu.1870230413.
- [5] E. L. Madsen. 1978. Tissue mimicking materials for ultrasound phantoms. *Medical Physics*. 5,5,391. DOI= 10.1118/1.59448.
- [6] T. J. Hall, M. Bilgen, M. F. Insana, T. a Krouskop. 1997. Phantom materials for elastography. *IEEE Transactions on Ultrasonics, Ferroelectrics and Frequency Control*. 44, 6, 1355-1365. DOI= 10.1109/58.656639.
- [7] K. Zell, J. I. Sperl, M. W. Vogel, R. Niessner, C. Haisch. 2007. Acoustical properties of selected tissue phantom materials for ultrasound imaging. *Physics in medicine and biology*. 52, 20, 475-84. DOI = 10.1088/0031-9155/52/20/N02.
- [8] Cheng HD, Shan J, Ju W, Guo Y, Zhang L. 2010. Automated breast cancer detection and classification using ultrasound images: A survey. *Pattern Recognition*. 43,1,299-317. DOI=10.1016/j.patcog.2009.05.012.
- [9] Shrimali V, Anand R, Kumar V. 2009. Current Trends in Segmentation of Medical Ultrasound B-mode Images: A Review. *IETE Technical Review*. 26,1,8. DOI= 10.4103/0256-4602.48464.
- [10] Abdelrahman A, Hamid O. 2011. Lesion boundary detection in ultrasound breast images. *Engineering and Technology*. 320-323. DOI=10.1117/12.708625.
- [11] Nobuyuki Otsu. 1979. A threshold selection method from gray-level histograms. *IEEE Trans. Sys., Man., Cyber.* 9,1, 62-66. DOI =10.1109/TSMC.1979.4310076.
- [12] J.K. Udupa, V.R. LeBlanc. 2002. Methodology for evaluating image-segmentation algorithms. *In SPIE Medical Imaging, San Diego*. ,4684, 266. DOI=10.1117/12. 467166.
- [13] Xujia Qin, Jionghui Jiang , Weihong Wang. 2007. Canny Operator based Level Set Segmentation Algorithm for Medical Images. *The 1st International Conference on Bioinformatics and Biomedical Engineering*,892-895. DOI=10.1109/ICBBE.2007.232.
- [14] M. Cvancarova, F. Albreghsen, K. Brabrand. 2005. Segmentation of ultrasound images of liver tumors applying snake algorithms and GVF. *International Congress Series*. 1281, 218-223. DOI=10.1016/j.ics.2005.03.190.
- [15] T. Chan and L. Vese. 2001.Active contours without edges. *IEEE Trans. Image Process*. DOI =10.1.1.2.1828.
- [16] Chung-Ming Chen, Henry Horng-Shing Lu,and Ko-Chung Han. 2001. A textural approach based on Gabor functions for texture edge detection in ultrasound images. *Ultrasound in Medicine & Biology*. 27,4,515-34.DOI= 10.1016/S0301-5629(00)00323-9.
- [17] X.Hao, C.Bruce,C.Pislaru, J.F.Greenleaf. 2000. A novel region growing method for segmenting ultrasound images. *IEEE Ultrasonics Symposium*. 2,2,717-1720. DOI= 10.1109/ULTSYM. 2000.921653.
- [18] C.M.Chen, L.H.Horng-shing, Y.L.Chen. 2003. A discrete region competition approach incorporating weak edge enhancement for ultrasound image segmentation. *Pattern Recognition Letters*. 24, 4-5. DOI= 10.1016/S0167-655(02)00175-7.
- [19] A. Madabhushi, D.N.Metaxas. 2003. Combining low,high-level and empirical domain knowledge for automated segmentation of ultrasonic breast lesions. *Medical Imaging*, IEEE Transactions on. 22,2,155-169. DOI= 10.1109/TMI. 2002. 808364.
- [20] Slabaugh G, Unal G, Wels M, Fang T, Rao B. 2009. Statistical region-based segmentation of ultrasound images. *Ultrasound in medicine & biology*.,35,5,781-95. DOI=10.1016/j. ultramedbio. 2008.10.014
- [21] Slabaugh G, Unal G, Fang T, Wels M. 2006. Ultrasound-specific segmentation via decorrelation and statistical region-based active contours. *Proc. IEEE Conference on Computer Vision and Pattern Recognition*.45-53. DOI= 10.1109/CVPR. 2006.318.
- [22] LA Christopher, EJ Delp, CR Meyer, PL Carson. 2002. 3-D Bayesian ultrasound breast image segmentation using the EM/MPM algorithm. *IEEE International Symposium on Proceedings of Biomedical Imaging*. DOI= 10.1109/ISBI. 2002.1029199.
- [23] Abouzar Eslami, Shohreh Kasaei, Mehran Jahed. 2004. Radial Multiscale Cyst Segmentation in Ultrasound Images of Kidney. *Signal Processing and Information Technology*. 42 - 45. DOI = 10.1109/ISSPIT.2004.1433684.
- [24] X. Bresson, S. Esedoglu, P. Vandergheynst, J. Thiran , S. Osher. 2007. Fast Global Minimization of the Active Contour/Snake Model. *Journal of Mathematical Imaging and Vision*. 28,2. DOI=10.1007/s10851-007-0002-0.
- [25] Marcos Martin-Fernandez, Carlos Alberola-Lopez. 2004. An approach for contour detection of human kidneys from ultrasound images using Markov random fields and active contours. *Medical Image Analysis*. 91,1-23. DOI= 10.1016/j.media.2004.05.001.
- [26] Ma Li, R.C. Staunton. 2007. Optimum Gabor filter design and local binary patterns for texture. *Pattern Recognition Letters*. 29,5. DOI=10.1016/j.patrec.2007.12.001.

CURRICULUM VITAE

Personal data

Name: Lin Li
Date of birth: 19.08.1980
Place of birth: China
Citizenship: Chinese

Contact data

Address: Akadeemia tee 5A, Tallinn, Estonia
Phone: +37253511055
E-mail: Lin.li@ttu.ee

Education

2011 – 2015	Tallinn University of Technology	PhD
2003 – 2006	Tianjin University of Technology	MSC
1999 – 2003	Tianjin University of Technology	BSc
1996 – 1999	Baise Highschool	Highschool

Language competence

Chinese	Native
English	Fluent

Professional employment

2007 – 2010	ZhengHai RenLi company, engineer
-------------	----------------------------------

ELULOOKIRJELDUS

Isikuandmed

Nimi: Lin Li
Sünniaeg: 19.08.1980
Sünnikoht: Hiina
Kodakondsus: Hiina

Kontaktandmed

Aadress: Akadeemia tee 5A, Tallinn, Estonia
Telefon: +37253511055
E-mail: lin.li@ttu.ee

Hariduskäik

2011 – 2015	Tallinna Tehnikaülikool	PhD
2003 – 2006	Tianjin'i Tehnikaülikool	MSC
1999 – 2003	Tianjin'i Tehnikaülikool	BSc
1996 – 1999	Baise Keskkool	Keskharidus

Keelteoskus

Hiina keel – emakeel
Inglise keel – väga hea kõnes ja kirjas

Teenistuskäik

2007 – 2010 ZhengHai RenLi OÜ, insener

**DISSERTATIONS DEFENDED AT
TALLINN UNIVERSITY OF TECHNOLOGY ON
INFORMATICS AND SYSTEM ENGINEERING**

1. **Lea Elmik**. Informational Modelling of a Communication Office. 1992.
2. **Kalle Tammemäe**. Control Intensive Digital System Synthesis. 1997.
3. **Eerik Lossmann**. Complex Signal Classification Algorithms, Based on the Third-Order Statistical Models. 1999.
4. **Kaido Kikkas**. Using the Internet in Rehabilitation of People with Mobility Impairments – Case Studies and Views from Estonia. 1999.
5. **Nazmun Nahar**. Global Electronic Commerce Process: Business-to-Business. 1999.
6. **Jevgeni Riipulk**. Microwave Radiometry for Medical Applications. 2000.
7. **Alar Kuusik**. Compact Smart Home Systems: Design and Verification of Cost Effective Hardware Solutions. 2001.
8. **Jaan Raik**. Hierarchical Test Generation for Digital Circuits Represented by Decision Diagrams. 2001.
9. **Andri Riid**. Transparent Fuzzy Systems: Model and Control. 2002.
10. **Marina Brik**. Investigation and Development of Test Generation Methods for Control Part of Digital Systems. 2002.
11. **Raul Land**. Synchronous Approximation and Processing of Sampled Data Signals. 2002.
12. **Ants Ronk**. An Extended Block-Adaptive Fourier Analyser for Analysis and Reproduction of Periodic Components of Band-Limited Discrete-Time Signals. 2002.
13. **Toivo Paavle**. System Level Modeling of the Phase Locked Loops: Behavioral Analysis and Parameterization. 2003.
14. **Irina Astrova**. On Integration of Object-Oriented Applications with Relational Databases. 2003.
15. **Kuldar Taveter**. A Multi-Perspective Methodology for Agent-Oriented Business Modelling and Simulation. 2004.
16. **Taivo Kangilaski**. Eesti Energia käiduhaldussüsteem. 2004.
17. **Artur Jutman**. Selected Issues of Modeling, Verification and Testing of Digital Systems. 2004.
18. **Ander Tenno**. Simulation and Estimation of Electro-Chemical Processes in Maintenance-Free Batteries with Fixed Electrolyte. 2004.

19. **Oleg Korolkov.** Formation of Diffusion Welded Al Contacts to Semiconductor Silicon. 2004.
20. **Risto Vaarandi.** Tools and Techniques for Event Log Analysis. 2005.
21. **Marko Koort.** Transmitter Power Control in Wireless Communication Systems. 2005.
22. **Raul Savimaa.** Modelling Emergent Behaviour of Organizations. Time-Aware, UML and Agent Based Approach. 2005.
23. **Raido Kurel.** Investigation of Electrical Characteristics of SiC Based Complementary JBS Structures. 2005.
24. **Rainer Taniloo.** Ökonoomsete negatiivse diferentsiaaltakistusega astmete ja elementide disainimine ja optimeerimine. 2005.
25. **Pauli Lallo.** Adaptive Secure Data Transmission Method for OSI Level I. 2005.
26. **Deniss Kumlander.** Some Practical Algorithms to Solve the Maximum Clique Problem. 2005.
27. **Tarmo Veskioja.** Stable Marriage Problem and College Admission. 2005.
28. **Elena Fomina.** Low Power Finite State Machine Synthesis. 2005.
29. **Eero Ivask.** Digital Test in WEB-Based Environment 2006.
30. **Виктор Войтович.** Разработка технологий выращивания из жидкой фазы эпитаксиальных структур арсенида галлия с высоковольтным р-п переходом и изготовления диодов на их основе. 2006.
31. **Tanel Alumäe.** Methods for Estonian Large Vocabulary Speech Recognition. 2006.
32. **Erki Eessaar.** Relational and Object-Relational Database Management Systems as Platforms for Managing Softwareengineering Artefacts. 2006.
33. **Rauno Gordon.** Modelling of Cardiac Dynamics and Intracardiac Bio-impedance. 2007.
34. **Madis Listak.** A Task-Oriented Design of a Biologically Inspired Underwater Robot. 2007.
35. **Elmet Orasson.** Hybrid Built-in Self-Test. Methods and Tools for Analysis and Optimization of BIST. 2007.
36. **Eduard Petlenkov.** Neural Networks Based Identification and Control of Nonlinear Systems: ANARX Model Based Approach. 2007.
37. **Toomas Kirt.** Concept Formation in Exploratory Data Analysis: Case Studies of Linguistic and Banking Data. 2007.

38. **Juhan-Peep Ernits**. Two State Space Reduction Techniques for Explicit State Model Checking. 2007.
39. **Innar Liiv**. Pattern Discovery Using Seriation and Matrix Reordering: A Unified View, Extensions and an Application to Inventory Management. 2008.
40. **Andrei Pokatilov**. Development of National Standard for Voltage Unit Based on Solid-State References. 2008.
41. **Karin Lindroos**. Mapping Social Structures by Formal Non-Linear Information Processing Methods: Case Studies of Estonian Islands Environments. 2008.
42. **Maksim Jenihhin**. Simulation-Based Hardware Verification with High-Level Decision Diagrams. 2008.
43. **Ando Saabas**. Logics for Low-Level Code and Proof-Preserving Program Transformations. 2008.
44. **Ilja Tšahhirov**. Security Protocols Analysis in the Computational Model – Dependency Flow Graphs-Based Approach. 2008.
45. **Toomas Ruuben**. Wideband Digital Beamforming in Sonar Systems. 2009.
46. **Sergei Devadze**. Fault Simulation of Digital Systems. 2009.
47. **Andrei Krivošei**. Model Based Method for Adaptive Decomposition of the Thoracic Bio-Impedance Variations into Cardiac and Respiratory Components. 2009.
48. **Vineeth Govind**. DfT-Based External Test and Diagnosis of Mesh-like Networks on Chips. 2009.
49. **Andres Kull**. Model-Based Testing of Reactive Systems. 2009.
50. **Ants Torim**. Formal Concepts in the Theory of Monotone Systems. 2009.
51. **Erika Matsak**. Discovering Logical Constructs from Estonian Children Language. 2009.
52. **Paul Annus**. Multichannel Bioimpedance Spectroscopy: Instrumentation Methods and Design Principles. 2009.
53. **Maris Tõnso**. Computer Algebra Tools for Modelling, Analysis and Synthesis for Nonlinear Control Systems. 2010.
54. **Aivo Jürgenson**. Efficient Semantics of Parallel and Serial Models of Attack Trees. 2010.
55. **Erkki Joason**. The Tactile Feedback Device for Multi-Touch User Interfaces. 2010.

56. **Jürgo-Sören Preden**. Enhancing Situation – Awareness Cognition and Reasoning of Ad-Hoc Network Agents. 2010.
57. **Pavel Grigorenko**. Higher-Order Attribute Semantics of Flat Languages. 2010.
58. **Anna Rannaste**. Hierarcical Test Pattern Generation and Untestability Identification Techniques for Synchronous Sequential Circuits. 2010.
59. **Sergei Strik**. Battery Charging and Full-Featured Battery Charger Integrated Circuit for Portable Applications. 2011.
60. **Rain Ottis**. A Systematic Approach to Offensive Volunteer Cyber Militia. 2011.
61. **Natalja Sleptšuk**. Investigation of the Intermediate Layer in the Metal-Silicon Carbide Contact Obtained by Diffusion Welding. 2011.
62. **Martin Jaanus**. The Interactive Learning Environment for Mobile Laboratories. 2011.
63. **Argo Kasemaa**. Analog Front End Components for Bio-Impedance Measurement: Current Source Design and Implementation. 2011.
64. **Kenneth Geers**. Strategic Cyber Security: Evaluating Nation-State Cyber Attack Mitigation Strategies. 2011.
65. **Riina Maigre**. Composition of Web Services on Large Service Models. 2011.
66. **Helena Kruus**. Optimization of Built-in Self-Test in Digital Systems. 2011.
67. **Gunnar Pih**. Archetypes Based Techniques for Development of Domains, Requirements and Software. 2011.
68. **Juri Gavšin**. Intrinsic Robot Safety Through Reversibility of Actions. 2011.
69. **Dmitri Mihhailov**. Hardware Implementation of Recursive Sorting Algorithms Using Tree-like Structures and HFSM Models. 2012.
70. **Anton Tšertov**. System Modeling for Processor-Centric Test Automation. 2012.
71. **Sergei Kostin**. Self-Diagnosis in Digital Systems. 2012.
72. **Mihkel Tagel**. System-Level Design of Timing-Sensitive Network-on-Chip Based Dependable Systems. 2012.
73. **Juri Belikov**. Polynomial Methods for Nonlinear Control Systems. 2012.
74. **Kristina Vassiljeva**. Restricted Connectivity Neural Networks based Identification for Control. 2012.
75. **Tarmo Robal**. Towards Adaptive Web – Analysing and Recommending Web Users` Behaviour. 2012.

76. **Anton Karputkin.** Formal Verification and Error Correction on High-Level Decision Diagrams. 2012.
77. **Vadim Kimlaychuk.** Simulations in Multi-Agent Communication System. 2012.
78. **Taavi Viilukas.** Constraints Solving Based Hierarchical Test Generation for Synchronous Sequential Circuits. 2012.
79. **Marko Kääramees.** A Symbolic Approach to Model-based Online Testing. 2012.
80. **Enar Reilent.** Whiteboard Architecture for the Multi-agent Sensor Systems. 2012.
81. **Jaan Ojarand.** Wideband Excitation Signals for Fast Impedance Spectroscopy of Biological Objects. 2012.
82. **Igor Aleksejev.** FPGA-based Embedded Virtual Instrumentation. 2013.
83. **Juri Mihhailov.** Accurate Flexible Current Measurement Method and its Realization in Power and Battery Management Integrated Circuits for Portable Applications. 2013.
84. **Tõnis Saar.** The Piezo-Electric Impedance Spectroscopy: Solutions and Applications. 2013.
85. **Ermo Täks.** An Automated Legal Content Capture and Visualisation Method. 2013.
86. **Uljana Reinsalu.** Fault Simulation and Code Coverage Analysis of RTL Designs Using High-Level Decision Diagrams. 2013.
87. **Anton Tšepurov.** Hardware Modeling for Design Verification and Debug. 2013.
88. **Ivo Mürsepp.** Robust Detectors for Cognitive Radio. 2013.
89. **Jaas Ježov.** Pressure sensitive lateral line for underwater robot. 2013.
90. **Vadim Kaparin.** Transformation of Nonlinear State Equations into Observer Form. 2013.
92. **Reeno Reeder.** Development and Optimisation of Modelling Methods and Algorithms for Terahertz Range Radiation Sources Based on Quantum Well Heterostructures. 2014.
93. **Ants Koel.** GaAs and SiC Semiconductor Materials Based Power Structures: Static and Dynamic Behavior Analysis. 2014.
94. **Jaan Übi.** Methods for Coopetition and Retention Analysis: An Application to University Management. 2014.
95. **Innokenti Sobolev.** Hyperspectral Data Processing and Interpretation in Remote Sensing Based on Laser-Induced Fluorescence Method. 2014.
96. **Jana Toompuu.** Investigation of the Specific Deep Levels in p^- , i^- and n^- Regions of GaAs p^+pin-n^+ Structures. 2014.

97. **Taavi Salumäe.** Flow-Sensitive Robotic Fish: From Concept to Experiments. 2015.
98. **Yar Muhammad.** A Parametric Framework for Modelling of Bioelectrical Signals. 2015.
99. **Ago Mölder.** Image Processing Solutions for Precise Road Profile Measurement Systems. 2015.
100. **Kairit Sirts.** Non-Parametric Bayesian Models for Computational Morphology. 2015.
101. **Alina Gavrijaševa.** Coin Validation by Electromagnetic, Acoustic and Visual Features. 2015.
102. **Emiliano Pastorelli.** Analysis and 3D Visualisation of Microstructured Materials on Custom-Built Virtual Reality Environment. 2015.
103. **Asko Ristolainen.** Phantom Organs and their Applications in Robotic Surgery and Radiology Training. 2015.
104. **Aleksei Tepljakov.** Fractional-order Modeling and Control of Dynamic Systems. 2015.
105. **Ahti Lohk.** A System of Test Patterns to Check and Validate the Semantic Hierarchies of Wordnet-type Dictionaries. 2015.
106. **Hanno Hantson.** Mutation-Based Verification and Error Correction in High-Level Designs. 2015.